HAL
open science

Bi-temperature Euler Equations Modeling for Fusion Plasma

Élise Estibals, Hervé Guillard, Afeintou Sangam

To cite this version:

Élise Estibals, Hervé Guillard, Afeintou Sangam. Bi-temperature Euler Equations Modeling for Fusion Plasma. [Research Report] RR-9026, INRIA Sophia-Antipolis, France. 2017, pp.74. hal-01461679

HAL Id: hal-01461679

https://inria.hal.science/hal-01461679

Submitted on 8 Feb 2017

HAL is a multi-disciplinary open access archive for the deposit and dissemination of scientific research documents, whether they are published or not. The documents may come from teaching and research institutions in France or abroad, or from public or private research centers.

L'archive ouverte pluridisciplinaire **HAL**, est destinée au dépôt et à la diffusion de documents scientifiques de niveau recherche, publiés ou non, émanant des établissements d'enseignement et de recherche français ou étrangers, des laboratoires publics ou privés.

Bi-temperature Euler Equations Modeling for Fusion Plasma

Élise Estibals, Hervé Guillard, Afeintou Sangam

RESEARCH REPORT
N° 9026
February 2017
Project-Teams CASTOR

ISSN 0249-6399 ISRN INRIA/RR--9026--FR+ENG

Bi-temperature Euler Equations Modeling for Fusion Plasma

Élise Estibals, Hervé Guillard, Afeintou Sangam

Project-Teams CASTOR

Research Report n° 9026 — February 2017 — 74 pages

Abstract: This work deals with the modeling of fusion plasma by bi-temperature fluid models. First, using non-dimensional scaling of the governing equations, we give the assumptions leading to a bi-temperature model. Then we describe a finite volume method on non-structured meshes to approximate the solutions of this model. The method relies on a relaxation scheme to solve the Riemann problem at the interfaces.
The description of the finite volume method that uses the strong conservative form of the equations is given both in Cartesian as well as in cylindrical coordinate systems useful to compute flows inside a torus. Several numerical tests in Cartesian and cylindrical coordinate systems and in different geometries are presented in order to validate the numerical method.

Key-words: Kinetic model, fluid model, bi-temperature Euler equations, relaxation scheme, finite volume method, toroidal geometry, fusion plasma.

RESEARCH CENTRE
SOPHIA ANTIPOLIS – MÉDITERRANÉE

2004 route des Lucioles - BP 93
06902 Sophia Antipolis Cedex

Modélisation des équations d'Euler bi-températures pour les plasmas de fusion

Résumé : Ce travail traite de la modélisation des plasmas de fusion par des modèles à deux températures. Tout d'abord, en adimensionnant les équations, on donne les hypothèses permettant d'obtenir le modèle bi-température. On décrit ensuite une méthode aux volumes finis pour des maillages non-structurés afin d'approcher les solutions du modèle. Cette méthode se sert des schémas de relaxation pour résoudre les problèmes de Riemann aux interfaces.
Cette méthode, qui utilise la formulation forte des équations conservatives, est donnée à la fois pour les coordonnées cartésiennes et cylindriques ces dernières étant utiles pour la modélisation des écoulements dans un tore. Des tests numériques sont présentés pour les coordonnées cartésiennes et cylindriques afin de valider la méthode numérique.

Mots-clés : Modèle cinétique, Modèle fluide, équations d'Euler bi-températures, schéma de relaxation, méthode volumes finis, géométrie toroïdale, plasma de fusion.

1 Introduction

Fusion energy as a sustainable power source with favourable economic, environmental and safety attributes, is a subject of active experimental, theoretical and numerical researches. Fusion is the process which powers the sun and the stars. In future fusion reactors, energy will be released by merging together hydrogen isotopes, namely Deuterium and Tritium, producing α particles and fast neutrons carrying a lot of energy. Fusion occurs naturally at the extremely high pressures and temperatures which exist at the center of the sun, 15 millions of degrees Celsius. At the high temperatures experienced in the sun, any gas becomes a plasma, a mixture of negatively charged electrons and either positively charged atomic nuclei or ions. In order to reproduce fusion on earth, gases need to be heated to extremely high temperatures whereby atoms become completely ionized yielding a hot plasma. Currently, two ways are studied to attain the high temperatures and densities needed to initiate a fusion reaction.

One is called Magnetic Confinement Fusion shortly named MCF, a method in which a plasma is confined thanks to an extremely large (several Tesla) magnetic field. Although different alternatives exist (Stellarator as Wendelstein 7-X [43], Z-Pinch) the main concept currently studied is the tokamak where an axisymmetric plasma is confined in a toroidal chamber. The tokamak *Iter*, [3] and [42] p711 currently being in Cadarache, France, is the largest of these devices. The beginning of its operational phase is scheduled for 2025-2030 and the construction of the demonstration fusion reactor *Demo* [44] will follow if ITER is successful. However, the stability of fusion scenario in these machines is an open question and the plasma behaviour in tokamaks is not totally understood, justifying an intense numerical and theoretical effort to help in the development of these machines.

The other main method to produce fusion energy is called Inertial Confinement Fusion abbreviated ICF [2]. The method uses laser devices such as the *MégaJoule* laser [10] in Bordeaux, France or the *NIF* [27] in the USA. For ICF, the fusion is initiated by a sudden heating and compression of a target composed of Deuterium, and Tritium surrounded by an outer layer made of gold. This process leads to the implosion of the layer and to shock waves propagating inside the target. If those shock waves are sufficiently powerful the fusion reaction can be initiated at the target center. However, as in tokamaks, some instabilities appear. Those instabilities are due to the interaction of laser beam and the plasma leading to the diffusion of laser energy and a turbulent mixing between the outer material and the target preventing fusion reaction to occur. There is therefore a crucial need to a deeper understanding of plasma dynamics and of reliable numerical and theoretical models able to study it.

The dynamics of the charged particles of a plasma can be described by several models, amongst other kinetic models, fluid models, transition regime models [36, 24]. In kinetic models, the charged particles of the plasma are described by distribution functions in time, physical and velocities space, that encode their interaction with electromagnetic fields and the collisions they undergo. Kinetic theories can accurately model such a system owning large number of particles. However, numerical computations of kinetic theories are, in general, resource consuming both in time and storage space, and are limited in a small computational domain of physical/velocities space. Large information yielded by kinetic models are not often accessible by experiment. Conversely fluid models constructed on velocity moments provide pertinent plasma parameters on a large time and a large domain [32, 33], which fit with experimental data.
Fluid models can be of different degrees of complexity. A two-fluid model considers a plasma as mixture of ions fluid and electrons fluid that are coupled by exchanged terms such as momentum

transfer terms, ion and electron heating terms due to collisions. This system is quite intricate (see for instance [24] pages 108 to 118 where a description of the wave system of this model is given) and seldom used for numerical purposes (see [37] for the description of an approximate Riemann solver for this system). Therefore, it is usually reduced to a one-fluid model whose characteristic quantities are weighted averages of the ones of the electrons and ions: only one density ρ, one velocity $\mathbf{u}$, one temperature T are then considered [4, 20, 24] to describe the plasma. Physical phenomena that are specific to either electrons or ions are then missed in this model.
Between these two models, an elaborated one-fluid model can be investigated instead, in which electrons and ions possess two different temperatures, namely T_i for ions and T_e for electrons. This model is known as either the two-temperature Euler model [16, 36, 1] or the T_i–T_e model. It is also called the bi-temperature Euler model.

The present report is concerned with a numerical approximation of the T_i–T_e model. The considered model is constituted by Euler equations where two equations describing the evolution of the ions temperature T_i and the electrons temperature T_e are taken into account. This model is given in [16, 20, 24, 30] and recently re-derived in [1]. This model assumes that ions and electrons have the same velocity, undergo an electric field but neglect the magnetic field. Numerical approximation of the proposed model by finite volume schemes is difficult since the T_i–T_e system is non-conservative. A significant work towards the numerical computation of solutions of the T_i–T_e model was suggested by Coquel and Marmignon in [16] for multi-species plasma: they transformed the non-conservative form into conservative one under the assumption of null electronic entropy jump across shocks, and then solved the obtained system by a Roe-type scheme. In the present work, we present a derivation of this model, more general than the ones given in [16, 20, 24, 30, 1] and building upon these works, a relaxation scheme is proposed to solve the T_i–T_e model both in Cartesian and cylindrical coordinates. With in mind future applications to MCF, we study the modification of finite volume type method to approximate the solutions of the T_i–T_e model in a toroidal geometry. Such a geometry is relevant in tokamaks [5, 20, 26, 29, 42], and in astrophysical systems as stars and galaxies [24].
The difficulty when dealing with models in a toroidal geometry is to appropriately take into account curvilinear coordinates systems within equations are formulated. Put simply in other words, the strong conservative form of equations of the model can be destroyed, introducing artificial source terms if cautions are not considered when manipulating vectorial equations in curvilinear coordinates. The scheme we proposed is based on recent works reported in [13, 12] where it is shown that the strong conservative form of the model can be kept whatever the system of curvilinear coordinates used. More precisely, the proposed finite volume scheme designed in this report is an application of the method described in [13, 12] to the T_i–T_e model in cylindrical coordinates for toroidal problems. However, such as application is not straightforward due to both the complexity of the T_i–T_e model and the unstructured tessellation used to adequately mesh the toroidal geometry of the tokamak.

This work is organised as follows. In Section 2 a review of the models used in plasma physics is given: a hierarchy of models from kinetic view to fluid frame is presented and the T_i–T_e model considered in this paper is introduced in Section 3 as a limit for large plasma β parameter of the two-fluid model. Section 3 presents also a study of the mathematical properties of this model. Afterwards general principles of finite volume method are recalled and its version used for the numerical simulation of the model is developed in Section 4. This numerical strategy is based on a finite volume method in a toroidal geometry addressed in [13, 12] coupled to a relaxation scheme derived in [1], which constitutes the matter of Section 5. Numerical tests are performed in Section 6. A conclusion is finally given in Section 7.

2 Plasma modeling

In this Section, we present the kinetic model leading to the bi-fluid MHD equations. First, we present the kinetic model for two species: the electrons denoted e, and the ions denoted i. Then, we give the definitions of some macroscopic quantities. Those definitions are then used to derive the kinetic equations leading to the bi-fluid macroscopic equations. Finally, the Maxwell equations are added to the bi-fluid ones in order to obtain the bi-fluid MHD equations.

2.1 Kinetic model

The plasma is composed of electrons and ions submitted to an electric field $\mathbf{E} \in \mathbb{R}^3$ and to a magnetic field $\mathbf{B} \in \mathbb{R}^3$. The kinetic model describes at the microscopic scale the behaviour of the particles in the plasma [15]. To each species $\alpha = e, i$, is associated a distribution function f_α. This function depends on the time $t \in \mathbb{R}_+$, on the position $\mathbf{x} \in \mathbb{R}^3$, and on the velocity $\mathbf{v} \in \mathbb{R}^3$. The distribution function is solution of the Boltzmann equation

$$\partial_t f_\alpha + \mathbf{v} \cdot \nabla f_\alpha + \frac{q_\alpha}{m_\alpha}(\mathbf{E} + \mathbf{v} \times \mathbf{B}) \cdot \nabla_{\mathbf{v}} f_\alpha = C_{\alpha,\alpha} + C_{\alpha,\beta}, \ (\alpha, \beta) = (e, i), (i, e), \tag{1}$$

where $C_{\alpha,\alpha}$ represents the collisions between α particles, and $C_{\alpha,\beta}$ represents the collisions between α particles and β particles. The operator $\nabla_{\mathbf{v}}$ is the gradient operator in the velocity space. The Lorentz force applied to the plasma is defined by

$$\mathbf{a}_\alpha = \frac{q_\alpha}{m_\alpha} \left(\mathbf{E} + \mathbf{v} \times \mathbf{B}\right),$$

where q_α is the charge associated to the species α, and m_α is its mass.

The minimal required properties that collision operators must fulfills are to conserve the mass per species, the total momentum, and the total energy. Hence, we have

$$\int_{\mathbb{R}^3} m_\alpha C_{\alpha,\beta} d\mathbf{v} = 0, \ \alpha = e, i, \ \beta = e, i, \tag{2}$$

$$\int_{\mathbb{R}^3} m_\alpha \mathbf{v} C_{\alpha,\beta} d\mathbf{v} + \int_{\mathbb{R}^3} m_\beta \mathbf{v} C_{\beta,\alpha} d\mathbf{v} = 0, \ \alpha = e, i, \ \beta = e, i, \tag{3}$$

$$\int_{\mathbb{R}^3} \frac{1}{2} m_\alpha \mathbf{v}^2 C_{\alpha,\beta} d\mathbf{v} + \int_{\mathbb{R}^3} \frac{1}{2} m_\beta \mathbf{v}^2 C_{\beta,\alpha} d\mathbf{v} = 0, \ \alpha = e, i, \ \beta = e, i. \tag{4}$$

The relations (3) and (4) show that the collision operator $C_{\alpha,\alpha}$ also conserves the momentum and the energy of each species

$$\int_{\mathbb{R}^3} m_\alpha \mathbf{v} C_{\alpha,\alpha} d\mathbf{v} = 0, \ \alpha = e, i,$$

$$\int_{\mathbb{R}^3} \frac{1}{2} m_\alpha \mathbf{v}^2 C_{\alpha,\alpha} d\mathbf{v} = 0, \ \alpha = e, i.$$

2.2 Macroscopic quantities

The macroscopic quantities are obtained with the extraction of the different moments of the distribution function. For example, the density n_α, the velocity $\mathbf{u}_\alpha$, and the total energy $\mathcal{E}_\alpha$ of

the species $\alpha = e, i$ are respectively given by the zeroth, the first, and the second moments of f_α:

$$n_\alpha = \int_{\mathbb{R}^3} f_\alpha d\mathbf{v}, \tag{5}$$

$$\mathbf{u}_\alpha = \frac{1}{n_\alpha} \int_{\mathbb{R}^3} \mathbf{v} f_\alpha d\mathbf{v}, \tag{6}$$

$$\mathcal{E}_\alpha = \int_{\mathbb{R}^3} \frac{1}{2} m_\alpha \mathbf{v}^2 f_\alpha d\mathbf{v} = \frac{3}{2} n_\alpha k_B T_\alpha + \frac{1}{2} \rho_\alpha \mathbf{u}_\alpha^2, \tag{7}$$

where $\rho_\alpha = n_\alpha m_\alpha$, T_α is defined as the temperature of the species, and $k_B = 1.3806 \times 10^{-23} J.K^{-1}$ is the Boltzmann constant.

We also introduce the velocity of the mixture and the temperature of the mixture with

$$\mathbf{u} = \frac{\rho_e \mathbf{u}_e + \rho_i \mathbf{u}_i}{\rho}, \tag{8}$$

$$\frac{3}{2} n k_B T = \sum_{\alpha = e,i} \left[\frac{1}{2} \rho_\alpha (\mathbf{u}_\alpha^2 - \mathbf{u}^2) + \frac{3}{2} n_\alpha k_B T_\alpha \right],$$

where $n = n_e + n_i$ and $\rho = \rho_e + \rho_i$.

The total charge and the current are defined by

$$\overline{\rho} = \int_{\mathbb{R}^3} q_e f_e d\mathbf{v} + \int_{\mathbb{R}^3} q_i f_i d\mathbf{v} = n_e q_e + n_i q_i,$$

$$\mathbf{J} = \int_{\mathbb{R}^3} q_e \mathbf{v} f_e d\mathbf{v} + \int_{\mathbb{R}^3} q_i \mathbf{v} f_i d\mathbf{v} = q_e n_e \mathbf{u}_e + q_i n_i \mathbf{u}_i. \tag{9}$$

2.3 Collision operators

There are a great number of collision operators. In this model, we limit ourselves to BGK type operators [11]. Then, the two collision operators are written in the form

$$\begin{cases} C_{\alpha,\alpha} &= \dfrac{1}{\tau_\alpha} \left(\mathcal{M}_\alpha - f_\alpha \right), \\ C_{\alpha,\beta} &= \dfrac{1}{\tau_{\alpha\beta}} \left(\overline{\mathcal{M}_\alpha} - f_\alpha \right), \end{cases}$$

where $\dfrac{1}{\tau_\alpha}$ is the frequency of collision between particles of the same species α. The frequency of electron/ion collisions $\dfrac{1}{\tau_{ei}}$, the frequency of ion/electron collisions is $\dfrac{1}{\tau_{ie}}$. The functions $\mathcal{M}_\alpha$ and $\overline{\mathcal{M}_\alpha}$ are two Maxwellian distributions defined in [1] by

$$\mathcal{M}_\alpha(f_\alpha) = \frac{n_\alpha}{(2\pi k_B T_\alpha / m_\alpha)^{3/2}} \exp\left(-\frac{(\mathbf{v} - \mathbf{u}_\alpha)^2}{2 k_B T_\alpha / m_\alpha} \right),$$

$$\overline{\mathcal{M}_\alpha}(f_e, f_i) = \frac{n_\alpha}{(2\pi k_B \overline{T} / m_\alpha)^{3/2}} \exp\left(-\frac{(\mathbf{v} - \overline{\mathbf{u}})^2}{2 k_B \overline{T} / m_\alpha} \right),$$

where

$$\overline{\mathbf{u}} = \frac{\tau_{ie}\rho_e\mathbf{u}_e + \tau_{ei}\rho_i\mathbf{u}_i}{\tau_{ie}\rho_e + \tau_{ei}\rho_i}, \tag{10}$$

$$\overline{T} = \frac{\frac{3}{2}k_B(\tau_{ie}n_eT_e + \tau_{ei}n_iT_i) + \frac{1}{2}\tau_{ie}\rho_e(\mathbf{u_e}^2 - \overline{\mathbf{u}}^2) + \frac{1}{2}\tau_{ei}\rho_i(\mathbf{u_i}^2 - \overline{\mathbf{u}}^2)}{\frac{3}{2}k_B(\tau_{ie}n_e + \tau_{ei}n_i)}. \tag{11}$$

The variables $\overline{\mathbf{u}}$ and $\overline{T}$ are chosen such as the three following moments are

$$\int_{\mathbb{R}^3} m_\alpha \mathcal{M}_\alpha d\mathbf{v} = \int_{\mathbb{R}^3} m_\alpha \overline{\mathcal{M}}_\alpha d\mathbf{v} = \rho_\alpha, \tag{12}$$

$$\int_{\mathbb{R}^3} m_\alpha \mathbf{v}\mathcal{M}_\alpha d\mathbf{v} = \rho_\alpha \mathbf{u}_\alpha, \ \int_{\mathbb{R}^3} m_\alpha \mathbf{v}\overline{\mathcal{M}}_\alpha d\mathbf{v} = \rho_\alpha \overline{\mathbf{u}}, \tag{13}$$

$$\int_{\mathbb{R}^3} \frac{1}{2}m_\alpha \mathbf{v}^2\mathcal{M}_\alpha d\mathbf{v} = \frac{3}{2}n_\alpha k_B T_\alpha + \frac{1}{2}\rho_\alpha \mathbf{u}_\alpha^2, \ \int_{\mathbb{R}^3} \frac{1}{2}m_\alpha \mathbf{v}^2\overline{\mathcal{M}}_\alpha d\mathbf{v} = \frac{3}{2}n_\alpha k_B \overline{T} + \frac{1}{2}\rho_\alpha \overline{\mathbf{u}}^2. \tag{14}$$

We define $\mathbf{F}_{\alpha,\beta}$ and $\mathcal{W}_{\alpha,\beta}$ the first and the second moments of the collision operator $C_{\alpha,\beta}$ with

$$\mathbf{F}_{\alpha,\beta} = \int_{\mathbb{R}^3} m_\alpha \mathbf{v} C_{\alpha,\beta} d\mathbf{v}, \tag{15}$$

$$\mathcal{W}_{\alpha,\beta} = \int_{\mathbb{R}^3} \frac{1}{2}m_\alpha \mathbf{v}^2 C_{\alpha,\beta} d\mathbf{v}. \tag{16}$$

According to the properties (3) and (4) we have

$$\mathbf{F}_{ie} = -\mathbf{F}_{ei}, \ \mathcal{W}_{ie} = -\mathcal{W}_{ei}.$$

Using the results (10)-(13) we have

$$\mathbf{F}_{ei} = \frac{1}{\tau_{ei}}(\overline{\mathbf{u}} - \mathbf{u}_e) = \frac{\rho_e\rho_i}{\tau_{ie}\rho_e + \tau_{ei}\rho_i}(\mathbf{u}_i - \mathbf{u}_e), \tag{17}$$

$$\begin{aligned} \mathcal{W}_{ei} &= \frac{1}{\tau_{ei}}\left[\frac{3}{2}n_ek_B(\overline{T} - T_e) + \frac{1}{2}\rho(\overline{\mathbf{u}}^2 - \mathbf{u}_e^2)\right]^2, \\ &= \nu_{ei}^{\mathcal{E}}(T_i - T_e) + \mathbf{F}_{ei}\cdot\left[\frac{1}{2}\left(\overline{\mathbf{u}} + \frac{\tau_{ie}n_e\mathbf{u}_i + \tau_{ei}n_i\mathbf{u}_e}{\tau_{ie}n_e + \tau_{ei}n_i}\right)\right], \end{aligned} \tag{18}$$

where

$$\nu_{ei}^{\mathcal{E}} = \frac{3}{2}k_B\frac{n_en_i}{\tau_{ie}n_e + \tau_{ei}n_i}. \tag{19}$$

In order to simplify the expression (18), we define

$$\widetilde{\mathcal{W}}_{\alpha,\beta} = \int_{\mathbb{R}^3} \frac{1}{2}m_\alpha(\mathbf{v} - \mathbf{u}_\alpha)^2 C_{\alpha,\beta} d\mathbf{v},$$

Then, we have

$$\mathcal{W}_{\alpha,\beta} = \widetilde{\mathcal{W}}_{\alpha,\beta} + \mathbf{F}_{\alpha,\beta}\cdot\mathbf{u}_\alpha, \tag{20}$$

where

$$\left\{\begin{array}{rcl}\widetilde{\mathcal{W}}_{ei} & = & \nu_{ei}^{\mathcal{E}}(T_i - T_e) + \dfrac{1}{2}\left[\dfrac{\tau_{ei}\rho_i}{\tau_{ie}\rho_e + \tau_{ei}\rho_i} + \dfrac{\tau_{ie}n_e}{\tau_{ie}n_e + \tau_{ei}n_i}\right]\mathbf{F}_{ei}\cdot(\mathbf{u}_i - \mathbf{u}_e), \\ \widetilde{\mathcal{W}}_{ie} & = & -\nu_{ei}^{\mathcal{E}}(T_i - T_e) + \dfrac{1}{2}\left[\dfrac{\tau_{ie}\rho_e}{\tau_{ie}\rho_e + \tau_{ei}\rho_i} + \dfrac{\tau_{ei}n_i}{\tau_{ie}n_e + \tau_{ei}n_i}\right]\mathbf{F}_{ei}\cdot(\mathbf{u}_i - \mathbf{u}_e).\end{array}\right. \tag{21}$$

2.4 Moment equations

In this subsection, we extract the zeroth, first, and the second moments of (1) to obtain the macroscopic equations. Since we have

$$\frac{q_\alpha}{m_\alpha}(\mathbf{E} + \mathbf{v}\times\mathbf{B})\cdot\nabla_{\mathbf{v}} f_\alpha = \nabla_{\mathbf{v}}\cdot\left[\frac{q_\alpha}{m_\alpha}(\mathbf{E} + \mathbf{v}\times\mathbf{B}) f_\alpha\right],$$

then the equation (1) can be rewritten as

$$\partial_t f_\alpha + \nabla\cdot(\mathbf{v} f_\alpha) + \nabla_{\mathbf{v}}\cdot\left[\frac{q_\alpha}{m_\alpha}(\mathbf{E} + \mathbf{v}\times\mathbf{B}) f_\alpha\right] = C_{\alpha,\alpha} + C_{\alpha,\beta}. \tag{22}$$

2.4.1 Mass conservation equation

The mass equation per species $\alpha = e, i$ is obtained by taking the zeroth moment of (22) meaning that we multiply it by the mass m_α, and integrate the results over the velocity space

$$\int_{\mathbb{R}^3} m_\alpha\Big[\partial_t f_\alpha + \nabla\cdot(\mathbf{v} f_\alpha) + \nabla_{\mathbf{v}}\cdot(\mathbf{a}_\alpha f_\alpha)\Big]d\mathbf{v} = \int_{\mathbb{R}^3} m_\alpha\Big(C_{\alpha,\alpha} + C_{\alpha,\beta}\Big)d\mathbf{v}. \tag{23}$$

According to (2), the two collision operators conserve the mass per species. Hence, the right side of (23) is zero. For the left side, as the distribution function is supposed to be zero at the infinity, the integral of the velocity divergence is also zero. For the two last terms, we use the definitions (5) and (6). Hence, the mass conservation equation per species is

$$\partial_t \rho_\alpha + \nabla\cdot(\rho_\alpha \mathbf{u}_\alpha) = 0,\ \alpha = e, i.$$

2.4.2 Momentum equation

To obtain the momentum equation for each species $\alpha = e, i$, the equation (22) is multiplied by $m_\alpha \mathbf{v}$ and integrated over the velocity space

$$\int_{\mathbb{R}^3} m_\alpha\mathbf{v}\Big[\partial_t f_\alpha + \nabla\cdot(\mathbf{v} f_\alpha) + \nabla_{\mathbf{v}}\cdot(\mathbf{a}_\alpha f_\alpha)\Big]d\mathbf{v} = \int_{\mathbb{R}^3} m_\alpha\mathbf{v}\Big(C_{\alpha,\alpha} + C_{\alpha,\beta}\Big)d\mathbf{v}.$$

According to the relation (3) and (15), we have

$$\int_{\mathbb{R}^3} m_\alpha\mathbf{v}\Big(C_{\alpha,\alpha} + C_{\alpha,\beta}\Big)d\mathbf{v} = \mathbf{F}_{\alpha,\beta}. \tag{24}$$

Writing that

$$m_\alpha\mathbf{v}\nabla_{\mathbf{v}}\cdot(\mathbf{a}_\alpha f_\alpha) = \nabla_{\mathbf{v}}\cdot(m_\alpha\mathbf{v}\otimes\mathbf{a}_\alpha f_\alpha) - m_\alpha\mathbf{a}_\alpha f_\alpha,$$

we deduce that the integral with the velocity divergence is

$$\int_{\mathbb{R}^3} m_\alpha\mathbf{v}\nabla_{\mathbf{v}}\cdot(\mathbf{a}_\alpha f_\alpha)\,d\mathbf{v} = -q_\alpha n_\alpha(\mathbf{E} + \mathbf{u}_\alpha\times\mathbf{B}). \tag{25}$$

Concerning the spatial divergence term, we remark that

$$\mathbf{v} \otimes \mathbf{v} = (\mathbf{v} - \mathbf{u}_\alpha) \otimes (\mathbf{v} - \mathbf{u}_\alpha) + \mathbf{v} \otimes \mathbf{u}_\alpha + \mathbf{u}_\alpha \otimes \mathbf{v} - \mathbf{u}_\alpha \otimes \mathbf{u}_\alpha.$$

Then, we obtain

$$\int_{\mathbb{R}^3} m_\alpha \mathbf{v} \otimes \mathbf{v} f_\alpha d\mathbf{v} = \rho_\alpha \mathbf{u}_\alpha \otimes \mathbf{u}_\alpha + \overline{\overline{P_\alpha}}, \tag{26}$$

where $\overline{\overline{P_\alpha}}$ is the pressure tensor defined by

$$\overline{\overline{P_\alpha}} = \int_{\mathbb{R}^3} m_\alpha (\mathbf{v} - \mathbf{u}_\alpha) \otimes (\mathbf{v} - \mathbf{u}_\alpha) f_\alpha d\mathbf{v}.$$

The scalar pressure is then defined by

$$p_\alpha = \frac{1}{3} trace \left(\overline{\overline{P_\alpha}} \right).$$

Therefore, the total energy of the species α (7) writes

$$\mathcal{E}_\alpha = \frac{3}{2} p_\alpha + \frac{1}{2} \rho_\alpha \mathbf{u}_\alpha^2,$$

and the ideal gas law that links the temperature and the pressure of the species α is

$$n_\alpha k_B T_\alpha = p_\alpha. \tag{27}$$

Finally, the pressure tensor rewrites

$$\overline{\overline{P_\alpha}} = p_\alpha \overline{\overline{I}} + \overline{\overline{\Pi_\alpha}},$$

where $\overline{\overline{I}}$ is the identity tensor and $\overline{\overline{\Pi_\alpha}}$ is known as the stress tensor. Hence the relation (26) becomes

$$\int_{\mathbb{R}^3} m_\alpha \mathbf{v} \otimes \mathbf{v} f_\alpha d\mathbf{v} = \rho_\alpha \mathbf{u}_\alpha \otimes \mathbf{u}_\alpha + p_\alpha \overline{\overline{I}} + \overline{\overline{\Pi_\alpha}}. \tag{28}$$

Using the results (6), (24), (25), and (28), we get the momentum equation of the species $\alpha = e, i$

$$\partial_t (\rho_\alpha \mathbf{u}_\alpha) + \nabla \cdot (\rho_\alpha \mathbf{u}_\alpha \otimes \mathbf{u}_\alpha) + \nabla p_\alpha = q_\alpha n_\alpha (\mathbf{E} + \mathbf{u}_\alpha \times \mathbf{B}) - \nabla \cdot \overline{\overline{\Pi_\alpha}} + \mathbf{F}_{\alpha,\beta}.$$

2.4.3 Energy equation

In this part, we extract the second moment of (22) in order to obtain the equation on the total energy per species $\alpha = e, i$. Hence, we multiply by $\frac{1}{2} m_\alpha \mathbf{v}^2$ the kinetic equation and integrate it on the velocity space

$$\int_{\mathbb{R}^3} \frac{1}{2} m_\alpha \mathbf{v}^2 \Big[\partial_t f_\alpha + \nabla \cdot (\mathbf{v} f_\alpha) + \nabla_{\mathbf{v}} \cdot (\mathbf{a}_\alpha f_\alpha) \Big] d\mathbf{v} = \int_{\mathbb{R}^3} \frac{1}{2} m_\alpha \mathbf{v}^2 \Big(C_{\alpha,\alpha} + C_{\alpha,\beta} \Big) d\mathbf{v}. \tag{29}$$

Let us first concentrate on the right side of (29). According to (20), we have

$$\int_{\mathbb{R}^3} \frac{1}{2} m_\alpha \mathbf{v}^2 \Big(C_{\alpha,\alpha} + C_{\alpha,\beta} \Big) d\mathbf{v} = \widetilde{\mathcal{W}}_{\alpha,\beta} + \mathbf{F}_{\alpha,\beta} \cdot \mathbf{u}_\alpha. \tag{30}$$

Concerning the last left term of (29) we remark that

$$\frac{1}{2}m_\alpha \mathbf{v}^2 \nabla_{\mathbf{v}} \cdot [\mathbf{a}_\alpha f_\alpha] = \nabla_{\mathbf{v}} \cdot \left[\frac{1}{2}m_\alpha \mathbf{v}^2 \mathbf{a}_\alpha f_\alpha\right] - m_\alpha \mathbf{v} \cdot \mathbf{a}_\alpha f_\alpha,$$

hence we have

$$\int_{\mathbb{R}^3} \frac{1}{2}m_\alpha \mathbf{v}^2 \nabla_{\mathbf{v}} \cdot [\mathbf{a}_\alpha f_\alpha]\, d\mathbf{v} = -q_\alpha n_\alpha \mathbf{E} \cdot \mathbf{u}_\alpha. \tag{31}$$

Indeed, as the force $\frac{q_\alpha}{m_\alpha}\mathbf{v} \times \mathbf{B}$ and to the velocity $\mathbf{v}$ are perpendicular, this force does not produce work. Using the same method as the one for the momentum equation, the spatial divergence term is

$$\nabla \cdot \left(\int_{\mathbb{R}^3} \frac{1}{2}m_\alpha \mathbf{v}^2 \mathbf{v} f_\alpha d\mathbf{v}\right) = \nabla \cdot [(\mathcal{E}_\alpha + p_\alpha)\, \mathbf{u}_\alpha] + \nabla \cdot \mathbf{Q}_\alpha + \nabla \cdot \left(\overline{\overline{\Pi_\alpha}}\mathbf{u}_\alpha\right), \tag{32}$$

where $\mathbf{Q}_\alpha$ is the heat flux of the species α given by

$$\mathbf{Q}_\alpha = \int_{\mathbb{R}^3} \frac{1}{2}m_\alpha (\mathbf{v} - \mathbf{u}_\alpha)^2 (\mathbf{v} - \mathbf{u}_\alpha) f_\alpha d\mathbf{v}.$$

Finally, with the definition (7) and the results (30)-(32), the total energy equation of the species $\alpha = e, i$ is

$$\partial_t \mathcal{E}_\alpha + \nabla \cdot [(\mathcal{E}_\alpha + p_\alpha)\, \mathbf{u}_\alpha] + \nabla \cdot \mathbf{Q}_\alpha = q_\alpha n_\alpha \mathbf{E} \cdot \mathbf{u}_\alpha - \nabla \cdot \left(\overline{\overline{\Pi_\alpha}}\mathbf{u}_\alpha\right) + \widetilde{\mathcal{W}}_{\alpha,\beta} + \mathbf{F}_{\alpha,\beta} \cdot \mathbf{u}_\alpha.$$

2.5 Maxwell equations

To complete the kinetic model, we add the four Maxwell equations to (1)

$$\begin{cases} \partial_t \mathbf{B} & = & -\nabla \times \mathbf{E}, & (33.a) \\ \frac{1}{c^2}\partial_t \mathbf{E} + \mu_0 \mathbf{J} & = & \nabla \times \mathbf{B}, & (33.b) \\ \varepsilon_0 \nabla \cdot \mathbf{E} & = & \overline{\rho}, & (33.c) \\ \nabla \cdot \mathbf{B} & = & 0, & (33.d) \end{cases}$$

where ε_0 is the permittivity of free space, μ_0 is the permeability of free space, and $c = \frac{1}{\sqrt{\varepsilon_0 \mu_0}}$ is the speed of the light in the vacuum. To the Maxwell system is associated an electromagnetic energy conservation equation: Take the scalar product of (33.a) with $\frac{\mathbf{B}}{\mu_0}$, take the scalar product of (33.b) with $\frac{\mathbf{E}}{\mu_0}$, add the resulting equations to obtain

$$\partial_t \mathcal{E}_{EM} + \nabla \cdot \mathbf{E} \times \frac{\mathbf{B}}{\mu_0} = -\mathbf{E} \cdot \mathbf{J}, \tag{34}$$

where the electromagnetic energy is defined by:

$$\mathcal{E}_{EM} = \frac{1}{2}\varepsilon_0 \mathbf{E}^2 + \frac{1}{2\mu_0}\mathbf{B}^2.$$

Since plasma particles move with velocities much smaller than the light celerity $c = 3\times 10^8 m.s^{-1}$, it is usual to neglect in (33.b) the displacement current $\frac{1}{c^2}\partial_t \mathbf{E}$. Hence, the Maxwell equations become

$$\left\{\begin{array}{lcl} \partial_t \mathbf{B} & = & -\nabla\times\mathbf{E}, \\ \mu_0 \mathbf{J} & = & \nabla\times\mathbf{B}, \\ \varepsilon_0 \nabla\cdot\mathbf{E} & = & \overline{\rho}, \\ \nabla\cdot\mathbf{B} & = & 0. \end{array}\right. \tag{35}$$

One can check that (34) remains valid except that the electromagnetic energy is now defined by

$$\mathcal{E}_{EM} = \frac{1}{2\mu_0}\mathbf{B}^2,$$

that is the electric energy is considered negligible in front of the magnetic one.

2.6 Bi-fluid MHD equations

The bi-fluid MHD equations are composed of the hydrodynamic equations and the low frequency Maxwell equations (35). Then, the bi-fluid MHD equations are given by the following system

$$\left\{\begin{array}{lcll} \partial_t \rho_e + \nabla\cdot(\rho_e \mathbf{u}_e) & = & 0, & (36.a) \\ \partial_t \rho_i + \nabla\cdot(\rho_i \mathbf{u}_i) & = & 0, & (36.b) \\ \partial_t(\rho_e \mathbf{u}_e) + \nabla\cdot(\rho_e \mathbf{u}_e\otimes\mathbf{u}_e) + \nabla p_e + \nabla\cdot\overline{\overline{\Pi}}_e & = & q_e n_e(\mathbf{E}+\mathbf{u}_e\times\mathbf{B}) + \mathbf{F}_{ei}, & (36.c) \\ \partial_t(\rho_i \mathbf{u}_i) + \nabla\cdot(\rho_i \mathbf{u}_i\otimes\mathbf{u}_i) + \nabla p_i + \nabla\cdot\overline{\overline{\Pi}}_i & = & q_i n_i(\mathbf{E}+\mathbf{u}_i\times\mathbf{B}) - \mathbf{F}_{ei}, & (36.d) \\ \partial_t \mathcal{E}_e + \nabla\cdot[(\mathcal{E}_e+p_e)\mathbf{u}_e] + \nabla\cdot\left(\overline{\overline{\Pi}}_e\mathbf{u}_e\right) + \nabla\cdot\mathbf{Q}_e & = & q_e n_e \mathbf{E}\cdot\mathbf{u}_e + \widetilde{\mathcal{W}}_{ei} + \mathbf{F}_{ei}\cdot\mathbf{u}_e, & (36.e) \\ \partial_t \mathcal{E}_i + \nabla\cdot[(\mathcal{E}_i+p_i)\mathbf{u}_i] + \nabla\cdot\left(\overline{\overline{\Pi}}_i\mathbf{u}_i\right) + \nabla\cdot\mathbf{Q}_i & = & q_i n_i \mathbf{E}\cdot\mathbf{u}_i + \widetilde{\mathcal{W}}_{ie} - \mathbf{F}_{ei}\cdot\mathbf{u}_i, & (36.f) \\ \partial_t \mathbf{B} & = & -\nabla\times\mathbf{E}, & (36.g) \\ \mu_0 \mathbf{J} & = & \nabla\times\mathbf{B}, & (36.h) \\ \varepsilon_0 \nabla\cdot\mathbf{E} & = & \overline{\rho}, & (36.i) \\ \nabla\cdot\mathbf{B} & = & 0, & (36.j) \end{array}\right.$$

Using the definition of the velocity of the mixture $\mathbf{u}$ in (8) and the one of the current $\mathbf{J}$ in (9), the two momentum equations can be replaced by one equation for the total momentum one and one equation for the current $\mathbf{J}$. First, we write the electronic and ionic velocities as a function of $\mathbf{u}$ and $\mathbf{J}$

$$\left\{\begin{array}{lcl} \mathbf{u}_e & = & \dfrac{1}{n_e(m_e q_i - m_i q_e)}\,(\rho q_i \mathbf{u} - m_i \mathbf{J}), \\ \\ \mathbf{u}_i & = & \dfrac{1}{n_i(m_i q_e - m_e q_i)}\,(\rho q_e \mathbf{u} - m_e \mathbf{J}). \end{array}\right. \tag{37}$$

Then, the total momentum equation writes

$$\partial_t(\rho\mathbf{u}) + \nabla\cdot(\rho\mathbf{u}\otimes\mathbf{u}) + \nabla\cdot[\rho_i\mathbf{u}_e\otimes(\mathbf{u}-\mathbf{u}_i) + \rho_e\mathbf{u}_i\otimes(\mathbf{u}-\mathbf{u}_e)] + \nabla p + \nabla\cdot\overline{\overline{\Pi}} = \overline{\rho}\,\mathbf{E} + \mathbf{J}\times\mathbf{B}, \tag{38}$$

where $p = p_e + p_i$ is the total pressure and $\overline{\overline{\Pi}} = \overline{\overline{\Pi}}_e + \overline{\overline{\Pi}}_i$ is the total stress tensor.

For the current equation, the momentum equations per species are rewritten in the following form

$$\partial_t(n_e\mathbf{u}_e) + \nabla\cdot(n_e\mathbf{u}_e\otimes\mathbf{u}_e) + \frac{1}{m_e}\left(\nabla p_e + \nabla\cdot\overline{\overline{\Pi}}_e\right) = \frac{q_e n_e}{m_e}\Big(\mathbf{E}+\mathbf{u}_e\times\mathbf{B}\Big) + \frac{1}{m_e}\mathbf{F}_{ei}, \tag{39}$$

$$\partial_t(n_i\mathbf{u}_i) + \nabla\cdot(n_i\mathbf{u}_i\otimes\mathbf{u}_i) + \frac{1}{m_i}\left(\nabla p_i + \nabla\cdot\overline{\overline{\Pi}}_i\right) = \frac{q_i n_i}{m_i}\Big(\mathbf{E}+\mathbf{u}_i\times\mathbf{B}\Big) - \frac{1}{m_i}\mathbf{F}_{ei}, \tag{40}$$

By multiplying the equation (39) by q_e and the equation (40) by q_i and finally summing the results leads to the generalized Ohm's law

$$\begin{aligned}&\partial_t\mathbf{J} + \nabla\cdot[n_e q_e\mathbf{u}_e\otimes\mathbf{u}_e + n_i q_i\mathbf{u}_i\otimes\mathbf{u}_i] + \frac{n_e q_e}{\rho_e}\left(\nabla p_e + \nabla\cdot\overline{\overline{\Pi}}_e\right) + \frac{n_i q_i}{\rho_i}\left(\nabla p_i + \nabla\cdot\overline{\overline{\Pi}}_i\right)\\ &= \left(\frac{(n_e q_e)^2}{\rho_e} + \frac{(n_i q_i)^2}{\rho_i}\right)\mathbf{E} + \left(\frac{(n_e q_e)^2}{\rho_e}\mathbf{u}_e + \frac{(n_i q_i)^2}{\rho_i}\mathbf{u}_i\right)\times\mathbf{B} + \left(\frac{n_e q_e}{\rho_e} - \frac{n_i q_i}{\rho_i}\right)\mathbf{F}_{ei},\end{aligned} \tag{41}$$

The total energy of each species $\alpha = e, i$ are defined by $\mathcal{E}_\alpha$

$$\mathcal{E}_\alpha = \frac{p_\alpha}{\gamma_\alpha - 1} + \frac{1}{2}\rho_\alpha\mathbf{u}_\alpha^2, \tag{42}$$

where γ_α is the adiabatic index of the species α. This definition is consistent with the one of the kinetic definition (7) if these indexes correspond to the mono-atomic case

$$\gamma_e = \gamma_i = \frac{5}{3} = \gamma. \tag{43}$$

The total energy is defined as the sum of the total energy of the species:

$$\mathcal{E} = \mathcal{E}_i + \mathcal{E}_e = \frac{p_i + p_e}{\gamma - 1} + \frac{1}{2}\rho_i\mathbf{u}_i^2 + \frac{1}{2}\rho_e\mathbf{u}_e^2, \tag{44}$$

and the total mechanical energy is obtained by summing the energy equation of the ions and electrons:

$$\partial_t\mathcal{E} + \nabla\cdot[(\mathcal{E}_e + p_e)\mathbf{u}_e + (\mathcal{E}_i + p_i)\mathbf{u}_i] + \nabla\cdot\left(\overline{\overline{\Pi}}_e\mathbf{u}_e + \overline{\overline{\Pi}}_i\mathbf{u}_i\right) + \nabla\cdot(\mathbf{Q}_e + \mathbf{Q}_i) \quad = \quad \mathbf{E}\cdot\mathbf{J}. \tag{45}$$

Comparing this equation with (34), we see that the source term $\mathbf{E}\cdot\mathbf{J}$ represents a transfer of energy between mechanical energy and electromagnetic one. An equivalent relation to (45) in term of total energy, mechanical + electromagnetic, can therefore be

$$\partial_t\mathcal{E}_T + \nabla\cdot\left[(\mathcal{E}_e + p_e)\mathbf{u}_e + (\mathcal{E}_i + p_i)\mathbf{u}_i + \mathbf{E}\times\frac{\mathbf{B}}{\mu_0}\right] + \nabla\cdot\left(\overline{\overline{\Pi}}_e\mathbf{u}_e + \overline{\overline{\Pi}}_i\mathbf{u}_i\right) + \nabla\cdot(\mathbf{Q}_e + \mathbf{Q}_i) = 0, \tag{46}$$

where the total energy is now defined as the sum of the mechanical and electromagnetic energies

$$\mathcal{E}_T = \mathcal{E}_i + \mathcal{E}_e + \frac{1}{2\mu_0}\mathbf{B}^2 = \frac{p_i + p_e}{\gamma - 1} + \frac{1}{2}\rho_i\mathbf{u}_i^2 + \frac{1}{2}\rho_e\mathbf{u}_e^2 + \frac{1}{2\mu_0}\mathbf{B}^2. \tag{47}$$

Observe that this equation is under conservative form as it should be: the total energy is a conserved quantity that can only change due to fluxes through the boundary of the domain.

Instead of the equations (36.e)-(36.f) we can also use the definition (42) to get an equation for each pressure

$$\partial_t p_\alpha + \mathbf{u}_\alpha\cdot\nabla p_\alpha + \gamma p_\alpha\nabla\cdot\mathbf{u}_\alpha + (\gamma - 1)\left[\overline{\overline{\Pi}}_\alpha : \nabla\mathbf{u}_\alpha + \nabla\cdot\mathbf{Q}_\alpha\right] = (\gamma - 1)\widetilde{\mathcal{W}}_{\alpha,\beta}. \tag{48}$$

In the same way, by summing the equation of the electronic pressure and the ionic pressure and the relation (21), an equation for the total pressure can be obtained:

$$\partial_t(p_e+p_i)+\mathbf{u}\cdot\nabla(p_e+p_i)+\gamma(p_e+p_i)\nabla\cdot\mathbf{u}+(\gamma-1)\left[\overline{\overline{\Pi}}:\nabla\mathbf{u}+\nabla\cdot\mathbf{Q}\right]$$

$$\frac{\rho_i}{\rho_e}(\mathbf{u}-\mathbf{u}_i)\nabla p_e+\frac{\rho_e}{\rho_i}(\mathbf{u}-\mathbf{u}_e)\nabla p_i+\gamma\left[p_e\nabla\cdot\left(\frac{\rho_i}{\rho_e}(\mathbf{u}-\mathbf{u}_i)\right)+p_i\nabla\cdot\left(\frac{\rho_e}{\rho_i}(\mathbf{u}-\mathbf{u}_e)\right)\right]$$

$$+(\gamma-1)\left[\overline{\overline{\Pi}}_e:\nabla\left(\frac{\rho_i}{\rho_e}(\mathbf{u}-\mathbf{u}_i)\right)+\overline{\overline{\Pi}}_i:\nabla\left(\frac{\rho_e}{\rho_i}(\mathbf{u}-\mathbf{u}_e)\right)\right]=(\gamma-1)\mathbf{F}_{ei}\cdot(\mathbf{u}_i-\mathbf{u}_e).$$

For smooth ($\mathcal{C}^2$) solutions, it is mathematically equivalent to use in (36) instead of the two equations for the mechanical energies of the species, the two pressure equations (48) or the total energy equation and one pressure equation or any two independent equations derived from any combination of these equations. However, for discontinuous solutions, these combinations are not equivalent. In the sequel, we will choose for one of these two equations, the total energy equation (46) since this one has a clear physical meaning. We must then supplement it by another equation. A rigorous procedure [7] would be to choose this equation based on the analysis of travelling wave solutions of the system (36). However, this analysis presents formidable mathematical difficulties that are far beyond the scope of this work. Instead we will complement equation (46) by an equation for the electronic entropy. For discontinuous solutions, this implies (see the next section) that we assume that the electronic entropy remains constant through a shock. Although this assumption has no physical justification, it is reasonable since the mass of the electrons is considerably smaller than the one of the ions. Thus one can expect that the changes in the electronic entropy will have a minimal impact on the behaviour of the other macroscopic quantities. This assumption has also been used in different context than plasma physics for instance in the modelling of multiphase flows where the hypothesis that the entropy of the lighter species is constant has shown to give results in reasonable agreement with the experiments [21]. Thus, we define the electronic entropy by

$$S_e=p_e\rho_e^{-\gamma}. \tag{49}$$

By using the equation of the electronic pressure (48), we get

$$\partial_t(\rho_eS_e)+\nabla\cdot(\rho_eS_e\mathbf{u}_e)+\rho_e^{1-\gamma}(\gamma-1)\left[\overline{\overline{\Pi}}_e:\nabla\mathbf{u}_e+\nabla\cdot\mathbf{Q}_e\right]=\rho_e^{1-\gamma}(\gamma-1)\widetilde{\mathcal{W}}_{ei}. \tag{50}$$

With the results (38), (41), (46), and (50), an equivalent system for smooth solution to the

bi-fluid MHD equations (36) can therefore be

$$\left\{\begin{array}{lcl}
\partial_t \rho_e & + & \nabla\cdot(\rho_e \mathbf{u}_e) = 0,\\
\partial_t \rho_i & + & \nabla\cdot(\rho_i \mathbf{u}_i) = 0,\\
\partial_t(\rho\mathbf{u}) & + & \nabla\cdot(\rho\mathbf{u}\otimes\mathbf{u}) + \nabla\cdot[\rho_i\mathbf{u}_e\otimes(\mathbf{u}-\mathbf{u}_i) + \rho_e\mathbf{u}_i\otimes(\mathbf{u}-\mathbf{u}_e)]\\
 & = & \overline{\rho}\,\mathbf{E} + \mathbf{J}\times\mathbf{B} - \nabla p - \nabla\cdot\overline{\overline{\Pi}},\\
\\
\partial_t \mathbf{J} & + & \nabla\cdot[n_e q_e \mathbf{u}_e\otimes\mathbf{u}_e + n_i q_i \mathbf{u}_i\otimes\mathbf{u}_i] + \dfrac{n_e q_e}{\rho_e}\left(\nabla p_e + \nabla\cdot\overline{\overline{\Pi}}_e\right) + \dfrac{n_i q_i}{\rho_i}\left(\nabla p_i + \nabla\cdot\overline{\overline{\Pi}}_i\right)\\
 & = & \left(\dfrac{(n_e q_e)^2}{\rho_e} + \dfrac{(n_i q_i)^2}{\rho_i}\right)\mathbf{E} + \left(\dfrac{(n_e q_e)^2}{\rho_e}\mathbf{u}_e + \dfrac{(n_i q_i)^2}{\rho_i}\mathbf{u}_i\right)\times\mathbf{B} + \left(\dfrac{n_e q_e}{\rho_e} - \dfrac{n_i q_i}{\rho_i}\right)\mathbf{F}_{ei},\\
\\
\partial_t \mathcal{E}_T & + & \nabla\cdot\left[(\mathcal{E}_e + p_e)\mathbf{u}_e + (\mathcal{E}_i + p_i)\mathbf{u}_i + \mathbf{E}\times\dfrac{\mathbf{B}}{\mu_0}\right] + \nabla\cdot\left(\overline{\overline{\Pi}}_e\mathbf{u}_e + \overline{\overline{\Pi}}_i\mathbf{u}_i\right)\\
 & + & \nabla\cdot(\mathbf{Q}_e + \mathbf{Q}_i) = 0,\\
\\
\partial_t(\rho_e S_e) & + & \nabla\cdot(\rho_e S_e \mathbf{u}_e) + \rho_e^{1-\gamma}(\gamma-1)\left[\overline{\overline{\Pi}}_e : \nabla\mathbf{u}_e + \nabla\cdot\mathbf{Q}_e\right] = \rho_e^{1-\gamma}(\gamma-1)\widetilde{\mathcal{W}}_{ei},\\
\\
\partial_t \mathbf{B} & = & -\nabla\times\mathbf{E},\\
\mu_0\mathbf{J} & = & \nabla\times\mathbf{B},\\
\varepsilon_0\nabla\cdot\mathbf{E} & = & \overline{\rho},\\
\nabla\cdot\mathbf{B} & = & 0.
\end{array}\right. \tag{51}$$

3 Bi-temperature Euler model

In this Section, we present the derivation of bi-temperature Euler equations from the bi-fluid MHD equations. In this model, only one density and one velocity are used but the two species can have different temperatures. In addition to the quasi-neutrality assumption, the fundamental hypothesis leading from the bi-fluid MHD system to the two temperature Euler model is that the dynamical pressure largely dominates the electromagnetic effects (large β). Hence, all the terms involving the current can be neglected. We conclude this Section by a mathematical study of the resulting equations.

3.1 Quasi-neutral regime

Considering that the constant ε_0 is very small, we assume that the net charge is near zero

$$\varepsilon_0\nabla\cdot\mathbf{E} \approx 0,$$

hence we have

$$\overline{\rho} = n_e q_e + n_i q_i = 0. \tag{52}$$

This hypothesis corresponds to quasi-neutral plasma. Then, we only need one equation on density. The charges q_e and q_i are given by

$$q_e = -e,\ \ q_i = Ze,$$

where $e = 1.6022\times 10^{-19}C$ is the elementary charge, and Z is the ion charge state. Here, we consider the case $Z = 1$ corresponding to hydrogen isotopes as Deuterium and Tritium. Then,

we deduce from (52)

$$\begin{cases} n_e &= n_i = n, \\ \mathbf{u} &= \dfrac{m_e}{m_e+m_i}\mathbf{u}_e + \dfrac{m_i}{m_e+m_i}\mathbf{u}_i, \\ \mathbf{J} &= ne(\mathbf{u}_i - \mathbf{u}_e). \end{cases}$$

Then, the system (37) becomes

$$\begin{cases} \mathbf{u}_e &= \mathbf{u} - \dfrac{c_i}{ne}\mathbf{J}, \\ \mathbf{u}_i &= \mathbf{u} + \dfrac{c_e}{ne}\mathbf{J}, \end{cases} \tag{53}$$

where c_α is the mass fraction of the species $\alpha = e, i$ given by,

$$c_\alpha = \frac{\rho_\alpha}{\rho} = \frac{m_\alpha}{m_e + m_i}.$$

With these results, the momentum equation of system (51) becomes

$$\partial_t(\rho\mathbf{u}) + \nabla\cdot(\rho\mathbf{u}\otimes\mathbf{u}) + \frac{m_e m_i}{m_e+m_i}\nabla\cdot\left(\frac{1}{ne^2}\mathbf{J}\otimes\mathbf{J}\right) + \nabla p + \nabla\cdot\overline{\overline{\Pi}} = \mathbf{J}\times\mathbf{B}. \tag{54}$$

The vector $\mathbf{F}_{ei}$ given in (17) is rewritten in function of the current $\mathbf{J}$

$$\mathbf{F}_{ei} = \frac{m_e m_i}{(\tau_{ie}m_e + \tau_{ei}m_i)e}\mathbf{J}, \tag{55}$$

therefore the Ohm's law becomes with quasi-neutrality simplications

$$\begin{aligned} &\frac{m_i m_e}{m_e+m_i}\left[\frac{1}{e}\Big(\partial_t\mathbf{J} + \nabla\cdot(\mathbf{u}\otimes\mathbf{J} + \mathbf{J}\otimes\mathbf{u})\Big)\right] - \frac{m_e m_i(m_i-m_e)}{(m_e+m_i)^2}\nabla\cdot\left(\frac{1}{ne^2}\mathbf{J}\otimes\mathbf{J}\right) \\ &+c_e\left[\nabla p_i + \nabla\cdot\overline{\overline{\Pi}}_i\right] - c_i\left[\nabla p_e + \nabla\cdot\overline{\overline{\Pi}}_e\right] = ne\Big[\mathbf{E} + \mathbf{u}\times\mathbf{B} - \eta\mathbf{J}\Big] - \frac{m_i-m_e}{m_i+m_e}\mathbf{J}\times\mathbf{B}, \end{aligned} \tag{56}$$

where η is the isotropic resistivity of the plasma and is defined by

$$\eta = \frac{m_i m_e}{ne^2(\tau_{ie}m_e + \tau_{ei}m_i)}. \tag{57}$$

Concerning the total energy, by using the system (53), the definition of the resistivity (57), and the result (55), we get

$$\begin{aligned} \partial_t\mathcal{E}_T \quad &+\nabla\cdot\left[(\mathcal{E}+p_e+p_i)\mathbf{u} + \mathbf{E}\times\frac{\mathbf{B}}{\mu_0}\right] + \nabla\cdot\left[\Big(c_e(\mathcal{E}_i+p_i) - c_i(\mathcal{E}_e+p_e)\Big)\frac{1}{ne}\mathbf{J}\right] \\ &+\nabla\cdot\Big(\overline{\overline{\Pi}}_e\mathbf{u}_e + \overline{\overline{\Pi}}_i\mathbf{u}_i\Big) + \nabla\cdot(\mathbf{Q}_e + \mathbf{Q}_i) = 0. \end{aligned}$$

For the electronic entropy, we simplify the results (21) with the quasi-neutrality hypothesis

$$\widetilde{\mathcal{W}}_{ei} = \nu_{ei}^{\mathcal{E}} + \zeta_{ei}\eta\mathbf{J}^2,$$

where

$$\zeta_{ei} = \frac{1}{2}\left[\frac{\tau_{ei} m_i}{\tau_{ie} m_e + \tau_{ei} m_i} + \frac{\tau_{ie}}{\tau_{ie} + \tau_{ei}}\right], \tag{58}$$

and finally, the electronic entropy equation of system (51) becomes

$$\begin{aligned}
&\partial_t(\rho_e S_e) + \nabla\cdot(\rho_e S_e \mathbf{u}) - c_i \nabla\cdot\left(\frac{1}{ne}\rho_e S_e \mathbf{J}\right) + \rho_e^{1-\gamma}(\gamma-1)\left[\overline{\overline{\Pi}}_e : \nabla\mathbf{u} + \nabla\cdot\mathbf{Q}_e\right] \\
&-c_i \rho_e^{1-\gamma}(\gamma-1)\overline{\overline{\Pi}}_e : \nabla\left(\frac{1}{ne}\mathbf{J}\right) = \rho_e^{1-\gamma}(\gamma-1)\left[\nu_{ei}^{\mathcal{E}}(T_i - T_e) + \zeta_{ei}\eta\mathbf{J}^2\right].
\end{aligned}$$

Then, the bi-fluid MHD system (51) writes with the quasi-neutrality assumption

$$\begin{cases}
\partial_t\rho + \nabla\cdot(\rho\mathbf{u}) = 0, \\
\partial_t(\rho\mathbf{u}) + \nabla\cdot(\rho\mathbf{u}\otimes\mathbf{u}) + \dfrac{m_e m_i}{m_e+m_i}\nabla\cdot\left(\dfrac{1}{ne^2}\mathbf{J}\otimes\mathbf{J}\right) + \nabla p + \nabla\cdot\overline{\overline{\Pi}} = \mathbf{J}\times\mathbf{B}, \\
\dfrac{m_i m_e}{m_e+m_i}\left[\dfrac{1}{e}\Big(\partial_t\mathbf{J} + \nabla\cdot(\mathbf{u}\otimes\mathbf{J} + \mathbf{J}\otimes\mathbf{u})\Big)\right] - \dfrac{m_e m_i(m_i-m_e)}{(m_e+m_i)^2}\nabla\cdot\left(\dfrac{1}{ne^2}\mathbf{J}\otimes\mathbf{J}\right) \\
+c_e\left[\nabla p_i + \nabla\cdot\overline{\overline{\Pi}}_i\right] - c_i\left[\nabla p_e + \nabla\cdot\overline{\overline{\Pi}}_e\right] = ne\Big[\mathbf{E} + \mathbf{u}\times\mathbf{B} - \eta\mathbf{J}\Big] - \dfrac{m_i-m_e}{m_i+m_e}\mathbf{J}\times\mathbf{B}, \\
\partial_t\mathcal{E}_T + \nabla\cdot\left[(\mathcal{E}+p_e+p_i)\mathbf{u} + \mathbf{E}\times\dfrac{\mathbf{B}}{\mu_0}\right] + \nabla\cdot\left[\Big(c_e(\mathcal{E}_i+p_i) - c_i(\mathcal{E}_e+p_e)\Big)\dfrac{1}{ne}\mathbf{J}\right] \\
+\nabla\cdot\Big(\overline{\overline{\Pi}}_e\mathbf{u}_e + \overline{\overline{\Pi}}_i\mathbf{u}_i\Big) + \nabla\cdot(\mathbf{Q}_e + \mathbf{Q}_i) = 0, \\
\partial_t(\rho_e S_e) + \nabla\cdot(\rho_e S_e\mathbf{u}) - c_i\nabla\cdot\left(\dfrac{1}{ne}\rho_e S_e\mathbf{J}\right) + \rho_e^{1-\gamma}(\gamma-1)\left[\overline{\overline{\Pi}}_e : \nabla\mathbf{u} + \nabla\cdot\mathbf{Q}_e\right] \\
-c_i\rho_e^{1-\gamma}(\gamma-1)\overline{\overline{\Pi}}_e : \nabla\left(\dfrac{1}{ne}\mathbf{J}\right) = \rho_e^{1-\gamma}(\gamma-1)\left[\nu_{ei}^{\mathcal{E}}(T_i-T_e) + \zeta_{ei}\eta\mathbf{J}^2\right], \\
\partial_t\mathbf{B} = -\nabla\times\mathbf{E}, \\
\mu_0\mathbf{J} = \nabla\times\mathbf{B}, \\
\nabla\cdot\mathbf{B} = 0.
\end{cases}$$

In the sequel, we will neglect the dissipative effects in the previous system in order to concentrate on the first-order part of the system. Neglecting dissipative terms usually means that we are mainly interested in the short term behaviour of the system since dissipative phenomena are generally associated to large time scales. Therefore, the system that we will consider from

now on is

$$\begin{cases} \partial_t \rho + \nabla \cdot (\rho \mathbf{u}) = 0, \\ \partial_t (\rho \mathbf{u}) + \nabla \cdot (\rho \mathbf{u} \otimes \mathbf{u}) + \dfrac{m_e m_i}{m_e + m_i} \nabla \cdot \left(\dfrac{1}{ne^2} \mathbf{J} \otimes \mathbf{J} \right) + \nabla (p_e + p_i) = \mathbf{J} \times \mathbf{B}, \\ \dfrac{m_i m_e}{m_e + m_i} \left[\dfrac{1}{e} \Big(\partial_t \mathbf{J} + \nabla \cdot (\mathbf{u} \otimes \mathbf{J} + \mathbf{J} \otimes \mathbf{u}) \Big) \right] - \dfrac{m_e m_i (m_i - m_e)}{(m_e + m_i)^2} \nabla \cdot \left(\dfrac{1}{ne^2} \mathbf{J} \otimes \mathbf{J} \right) \\ + c_e \nabla p_i - c_i \nabla p_e = ne \Big[\mathbf{E} + \mathbf{u} \times \mathbf{B} - \eta \mathbf{J} \Big] - \dfrac{m_i - m_e}{m_i + m_e} \mathbf{J} \times \mathbf{B}, \\ \partial_t \mathcal{E}_T + \nabla \cdot \left[(\mathcal{E} + p_e + p_i) \mathbf{u} + \mathbf{E} \times \dfrac{\mathbf{B}}{\mu_0} \right] + \nabla \cdot \left[\Big(c_e (\mathcal{E}_i + p_i) - c_i (\mathcal{E}_e + p_e) \Big) \dfrac{1}{ne} \mathbf{J} \right] = 0, \\ \partial_t (\rho_e S_e) + \nabla \cdot (\rho_e S_e \mathbf{u}) - c_i \nabla \cdot \left(\dfrac{1}{ne} \rho_e S_e \mathbf{J} \right) = \rho_e^{1-\gamma} (\gamma - 1) \left[\nu_{ei}^{\mathcal{E}} (T_i - T_e) + \zeta_{ei} \eta \mathbf{J}^2 \right], \\ \partial_t \mathbf{B} = -\nabla \times \mathbf{E}, \\ \mu_0 \mathbf{J} = \nabla \times \mathbf{B}, \\ \nabla \cdot \mathbf{B} = 0. \end{cases} \tag{59}$$

3.2 Derivation of the bi-temperature model

The system (59) contains two momentum equations: one for the total momentum (ions + electrons) and one for the current density $\mathbf{J}$. Our goal now is to eliminate the fast part of the dynamics related to the movement of the electrons while keeping the possibility for the ions and electrons to have different temperatures. To establish the range of validity of this simplification, we introduce non-dimensional parameters and to this end, we first begin to introduce reference quantities in order to express (59) in non-dimensional form. First, we denote respectively, L_0, n_0, $T_{e,0}$, $T_{i,0}$, and B_0 the reference length, density, electronic temperature, ionic temperature, and magnetic field. Then, since we are interested in phenomena where the velocities can be large, we introduce a reference velocity u_0 defined as:

$$u_0 = \sqrt{\frac{k_B (T_{e,0} + T_{i,0})}{m_e + m_i}}. \tag{60}$$

Later on, we will see that this velocity corresponds to the speed of sound of the ion-electron mixture. Thus, this choice of velocity scale means that we are interested in phenomena where the material velocity is comparable to the speed of sound. The time scale is chosen such that

$$t_0 = \frac{L_0}{u_0},$$

and this implies as usual that this choice of scales leaves unchanged the continuity equation and the material derivatives. Then from the state laws (27), the pressure scales are defined by

$$p_{\alpha,0} = n_0 k_B T_{\alpha,0}.$$

From the Maxwell-Ampère equation, we will also use the following scaling to define the reference current:

$$J_0 = \frac{B_0}{L_0 \mu_0}.$$

Then each variable is re-defined in term of reference quantities and non-dimensional variables as:

$$\widetilde{t} = \frac{t}{t_0},\ \widetilde{\mathbf{x}} = \frac{1}{L_0}\mathbf{x},\ \widetilde{\mathbf{u}} = \frac{1}{u_0}\mathbf{u},\ \widetilde{\rho} = \frac{\rho}{(m_e+m_i)n_0},\ \widetilde{T}_\alpha = \frac{T_\alpha}{T_{\alpha,0}},\ \alpha = e,i,\ \widetilde{\mathbf{B}} = \frac{1}{B_0}\mathbf{B},$$

where a super tilde $\widetilde{\cdot}$ denotes a non-dimensional variable.

The momentum equation can be re-written in the following form

$$\begin{aligned}\widetilde{\partial}_t(\widetilde{\rho}\widetilde{\mathbf{u}}) + \widetilde{\nabla}\cdot(\widetilde{\rho}\widetilde{\mathbf{u}}\otimes\widetilde{\mathbf{u}}) + \frac{m_e m_i}{(m_e+m_i)^2}\frac{B_0^2}{n_0^2 e^2\mu_0^2 L_0^2 u_0^2}\widetilde{\nabla}\cdot\left[\frac{1}{\widetilde{n}}\widetilde{\mathbf{J}}\otimes\widetilde{\mathbf{J}}\right]\\ +\frac{k_B T_{e,0}}{(m_e+m_i)u_0^2}\widetilde{\nabla}\widetilde{p}_e + \frac{k_B T_{i,0}}{(m_e+m_i)u_0^2}\widetilde{\nabla}\widetilde{p}_i = \frac{B_0^2}{\mu_0 n_0(m_e+m_i)u_0^2}\widetilde{\mathbf{J}}\times\widetilde{\mathbf{B}}.\end{aligned} \tag{61}$$

Let us define the (total) plasma β parameter by:

$$\beta = \frac{(m_e+m_i)n_0u_0^2}{B_0^2/\mu_0} = \frac{n_0k_B(T_{e,0}+T_{i,0})}{B_0^2/\mu_0} \tag{62}$$

The plasma β is a well known non-dimensional parameter used in plasma physics, it measures the ratio between the dynamic pressure and the magnetic pressure[1].
We also introduce the (electron) plasma frequency by:

$$\omega_{pe}^2 = \frac{n_0e^2}{\varepsilon_0 m_e} = \frac{n_0e^2c^2\mu_0}{m_e}. \tag{63}$$

as well as the length scale:

$$\delta_e^2 = \frac{c^2}{\omega_{pe}^2} = \frac{m_e}{n_0e^2\mu_0}. \tag{64}$$

This ratio is called the electron skin depth[2] in [20] while it is denoted electron inertial length [28] p.28 and in other references. According to [19] the value of the plasma frequency ω_{pe} varies between 6.10^{11} in tokamaks and 6.10^{15} in inertial confinement experiments while [28] gives the value of 6.10^{14} for laser plasma. Therefore the electron skin depth is always small in fusion plasma. Similar definitions exist to define the ion plasma frequency and inertial length:

$$\omega_{pi}^2 = \frac{n_0e^2}{\varepsilon_0 m_i} = \frac{n_0e^2c^2\mu_0}{m_i}, \qquad \delta_i^2 = \frac{c^2}{\omega_{pi}^2} = \frac{m_i}{n_0e^2\mu_0}. \tag{65}$$

The ratio between the ion and electron inertial lengths $\sqrt{m_i/m_e} \sim 40$ and thus the electron inertial length is significantly smaller than its ion counterpart.

Remark: Another commonly used parameters in magnetized plasma are the Larmor radii defined by:

$$\rho_{e,i} = \frac{m_{e,i}\nu_{e,i}}{eB_0}, \tag{66}$$

[1] this parameter is usually defined as $\beta = \dfrac{(m_e+m_i)n_0u_0^2}{B_0^2/2\mu_0}$, the difference by a factor 2 with the definition given in this section is of no importance since in the sequel we are considering the asymptotic form of the equation obtained when $\beta \to +\infty$

[2] not to be confused with the resistive skin depth

where $\nu_{e,i} = \sqrt{\dfrac{k_B T_{e,i}}{m_{e,i}}}$ are the thermal velocities of respectively the electrons and ions. We note the following relation between inertial lengths, plasma β and Larmor radii:

$$\rho_{e,i}^2 = \beta \delta_{e,i}^2,$$

and thus the non-dimensional form of the governing equations can also be done in term of Larmor radii instead of inertial lengths. Here we choose to use the inertial lengths in order to separate the magnetic effects from the electric ones.

Now let us introduce the non-dimensional version of the inertial lengths by:

$$\delta_{e,i}^* = \frac{\delta_{e,i}}{L_0}. \tag{67}$$

With these definitions and the choice (60) of the velocity scale, we can re-write (61) as

$$\begin{aligned} &\widetilde{\partial}_t(\widetilde{\rho}\widetilde{\mathbf{u}}) + \widetilde{\nabla}\cdot(\widetilde{\rho}\widetilde{\mathbf{u}}\otimes\widetilde{\mathbf{u}}) + c_i\frac{(\delta_e^*)^2}{\beta}\widetilde{\nabla}\cdot\left[\frac{1}{\widetilde{n}}\widetilde{\mathbf{J}}\otimes\widetilde{\mathbf{J}}\right] \\ &+\frac{T_{e,0}}{T_{e,0}+T_{i,0}}\widetilde{\nabla}\widetilde{p}_e + \frac{T_{i,0}}{T_{e,0}+T_{i,0}}\widetilde{\nabla}\widetilde{p}_i = \frac{1}{\beta}\widetilde{\mathbf{J}}\times\widetilde{\mathbf{B}}. \end{aligned} \tag{68}$$

This expression establishes that except for small β the factor in front of the quadratic term in the current in the equation (68) is small and therefore the current term can be neglected in this equation. Note that this result is valid independently of the mass ratio between electrons and ions. In particular, this result does not rely on the usual assumption that the electrons can be considered as massless. Actually, in the sequel, as we will consider large plasma β parameter, we do not need any assumption on the inertial length except that it is bounded.

We have now to consider the entropy equation. Nevertheless, since this is equivalent, we will work here with the electronic pressure equation

$$\partial_t p_e + \mathbf{u}\cdot\nabla p_e + \gamma p_e \nabla\cdot\mathbf{u} - c_i\left[\frac{1}{ne}\mathbf{J}\cdot\nabla p_e + \gamma p_e\nabla\cdot\left(\frac{1}{ne}\mathbf{J}\right)\right] = (\gamma-1)\left[\nu_{ei}^{\mathcal{E}}(T_i - T_e) + \zeta_{ei}\eta\mathbf{J}^2\right].$$

We recall definition (19) giving the expression of the temperature relaxation coefficient (note that $(\gamma-1)^{-1} = 3/2$ in the mono-atomic case)

$$\nu_{ei}^{\mathcal{E}} = \frac{k_B}{\gamma-1}\frac{n}{\tau_{ei}+\tau_{ie}},$$

and that the resistivity (57) is given by

$$\eta = \frac{m_i m_e}{ne^2(\tau_{ie}m_e + \tau_{ei}m_i)}.$$

Hence, we deduce that the non-dimensional pressure equation can be written

$$\begin{aligned} &\widetilde{\partial}_t\widetilde{p}_e + \widetilde{\mathbf{u}}\cdot\widetilde{\nabla}\widetilde{p}_e + \gamma\widetilde{p}_e\widetilde{\nabla}\cdot\widetilde{\mathbf{u}} - \sqrt{c_i}\frac{\delta_i^*}{\sqrt{\beta}}\left[\frac{1}{\widetilde{n}}\widetilde{\mathbf{J}}\cdot\widetilde{\nabla}\widetilde{p}_e + \gamma\widetilde{p}_e\widetilde{\nabla}\cdot\left(\frac{1}{\widetilde{n}}\widetilde{\mathbf{J}}\right)\right] \\ &= \left(\frac{T_{i,0}}{T_{e,0}}\widetilde{T}_i - \widetilde{T}_e\right)\widetilde{\nu}_{ei}^{\mathcal{E}} + (\gamma-1)\zeta_{ei}\left(1+\frac{T_{i,0}}{T_{e,0}}\right)\frac{(\delta_e^*)^2}{\beta}\widetilde{\eta}\widetilde{\mathbf{J}}^2. \end{aligned} \tag{69}$$

where the non dimensional temperature relaxation coefficient is defined as

$$\widetilde{\nu}_{ei}^{\mathcal{E}} = \frac{\widetilde{n}}{\widetilde{\tau}_{ei} + \widetilde{\tau}_{ie}},$$

where $\widetilde{\tau}_{ei} = \tau_{ei} u_0 / L_0$, and $\widetilde{\tau}_{ie} = \tau_{ie} u_0 / L_0$ denote the non-dimensional temperature relaxation times while the non-dimensional resistivity is

$$\widetilde{\eta} = \frac{m_i}{\widetilde{n}(\widetilde{\tau}_{ie} m_e + \widetilde{\tau}_{ei} m_i)}.$$

We notice that in this equation, ζ_{ei} does not change. Indeed, according to its definition (58), ζ_{ei} is already a non-dimension variable.

Note that in this equation the advective terms involving the current are multiplied by the *ion* inertial length. Symmetrically the corresponding term in the ion pressure equation will involve the *electron* inertial length.
The last term in equation (69) corresponds to Ohmic heating and is representative of the transfer between electromagnetic and internal energy.

According to the definition of the electronic entropy (49), the non-dimensional corresponding variable is

$$\widetilde{S}_e = \widetilde{\rho_e}^{-\gamma} \widetilde{p}_e,$$

then, the equation (69) re-writes

$$\begin{aligned} &\widetilde{\partial}_t(\widetilde{\rho}_e \widetilde{S}_e) + \widetilde{\nabla} \cdot (\widetilde{\rho}_e \widetilde{S}_e \widetilde{\mathbf{u}}) - \sqrt{c_i} \frac{\delta_i^*}{\sqrt{\beta}} \widetilde{\nabla} \cdot \left[\frac{\widetilde{\rho}_e \widetilde{S}_e}{\widetilde{n}} \widetilde{\mathbf{J}} \right] \\ &= \widetilde{\rho}_e^{1-\gamma} \left[\left(\frac{T_{i,0}}{T_{e,0}} \widetilde{T}_i - \widetilde{T}_e \right) \widetilde{\nu}_{ei}^{\mathcal{E}} + (\gamma - 1) \zeta_{ei} \left(1 + \frac{T_{i,0}}{T_{e,0}} \right) \frac{(\delta_e^*)^2}{\beta} \widetilde{\eta} \widetilde{\mathbf{J}}^2 \right]. \end{aligned} \tag{70}$$

We now consider the total energy equation (59). With the choice of the velocity scaling (60), the kinetic energy is of the same order as the thermal energy and therefore we choose to define the non-dimensional total energy and the non-dimensional total energy by species by:

$$\mathcal{E} = n_0 (m_e + m_i) u_0^2 \widetilde{\mathcal{E}}, \quad \mathcal{E}_\alpha = n_0 k_B T_{\alpha,0} \widetilde{\mathcal{E}}_\alpha, \ \alpha = e, i.$$

The choice of a scale for the electric field is delicate. Faraday's law favours the use of the scaling

$$\mathbf{E} = B_0 u_0 \widetilde{\mathbf{E}}.$$

and this is the choice that is usually done in MHD. However, since Faraday's law involve the curl of $\mathbf{E}$, we see that the gradient part of $\mathbf{E}$ (if it exists) has no reason to scale with $B_0 u_0$. To take this possibility into account, we will set

$$\mathbf{E} = \kappa B_0 u_0 \widetilde{\mathbf{E}},$$

leaving for the present time the parameter κ unspecified[3]. With these choices, we obtain:

$$\begin{aligned}&\widetilde{\partial}_t\left(\widetilde{\mathcal{E}}+\frac{\widetilde{\mathbf{B}}^2}{2\beta}\right)+\widetilde{\nabla}\cdot\left[(\widetilde{\mathcal{E}}+\frac{T_{e,0}}{T_{e,0}+T_{i,0}}\widetilde{p}_e+\frac{T_{i,0}}{T_{e,0}+T_{i,0}}\widetilde{p}_i)\widetilde{\mathbf{u}}+\frac{\kappa\widetilde{\mathbf{E}}\times\widetilde{\mathbf{B}}}{\beta}\right]+\\&\frac{1}{\sqrt{\beta}}\widetilde{\nabla}\cdot\left[\left(\sqrt{c_e}\delta_e^*\frac{T_{i,0}}{T_{e,0}+T_{i,0}}(\widetilde{p}_i+\widetilde{\mathcal{E}}_i)-\sqrt{c_i}\delta_i^*\frac{T_{e,0}}{T_{e,0}+T_{i,0}}(\widetilde{p}_e+\widetilde{\mathcal{E}}_e)\right)\frac{\widetilde{\mathbf{J}}}{\widetilde{n}}\right]=0.\end{aligned}\tag{71}$$

Again, the terms containing the current are multiplied by expressions involving the inertial lengths.

It remains to consider the electron momentum equations or alternatively the equation governing the evolution of the current. For the Ohm's law, the same scaling procedure gives:

$$\begin{aligned}&\kappa\widetilde{\mathbf{E}}+\widetilde{\mathbf{u}}\times\widetilde{\mathbf{B}}=(\delta_e^*)^2\widetilde{\eta}\widetilde{\mathbf{J}}+\frac{\sqrt{c_i}\delta_i^*-\sqrt{c_e}\delta_e^*}{\sqrt{\beta}}\frac{\widetilde{\mathbf{J}}\times\widetilde{\mathbf{B}}}{\widetilde{n}}\\&-\sqrt{c_i}\delta_i^*\sqrt{\beta}\frac{T_{e,0}}{T_{e,0}+T_{i,0}}\frac{1}{\widetilde{n}}\widetilde{\nabla}\widetilde{p}_e+\sqrt{c_e}\delta_e^*\sqrt{\beta}\frac{T_{i,0}}{T_{e,0}+T_{i,0}}\frac{1}{\widetilde{n}}\widetilde{\nabla}\widetilde{p}_i\\&+c_i(\delta_e^*)^2\frac{1}{\widetilde{n}}\left[\widetilde{\partial}_t\widetilde{\mathbf{J}}+\widetilde{\nabla}\cdot\left(\widetilde{\mathbf{u}}\otimes\widetilde{\mathbf{J}}+\widetilde{\mathbf{J}}\otimes\widetilde{\mathbf{u}}\right)\right]+\sqrt{c_i}(c_i-c_e)\frac{(\delta_e^*)^2\delta_i^*}{\sqrt{\beta}}\frac{1}{\widetilde{n}}\widetilde{\nabla}\cdot\left[\frac{1}{\widetilde{n}}\widetilde{\mathbf{J}}\otimes\widetilde{\mathbf{J}}\right].\end{aligned}\tag{72}$$

3.3 The final bi-temperature model for large β parameter

In equations (68), (69), (71), and (72), the non-dimensional parameters $c_{e,i}, \delta_{e,i}^*, \beta$,and κ appear. According to the different values of these parameters, the equations can take many different limiting forms describing a huge range of phenomena. Ideal MHD for instance, corresponds to situations where $\delta_{e,i}^* \to 0$ while β stays bounded. In this Section, with applications to laser plasma in mind, we will consider phenomena characterized by very large plasma β parameter where the dynamical pressure is far larger than the magnetic one. Although the model considers two different temperatures, we will also assume that these temperatures remain comparable and that the ratio $T_{i,0}/T_{e,0}$ remains bounded. We then formally consider the limit $\beta \to +\infty$ in equations (68), (71) and (70) and we obtain the system:

$$\left\{\begin{array}{lcl}\partial_t\rho+\nabla\cdot(\rho\mathbf{u}) & = & 0,\\ \partial_t(\rho\mathbf{u})+\nabla\cdot(\rho\mathbf{u}\otimes\mathbf{u})+\nabla(p_e+p_i) & = & 0,\\ \partial_t\mathcal{E}+\nabla\cdot[(\mathcal{E}+p_e+p_i)\,\mathbf{u}] & = & 0,\\ \partial_t(\rho_eS_e)+\nabla\cdot(\rho_eS_e\mathbf{u}) & = & \rho_e^{\gamma-1}(\gamma-1)\nu_{ei}^{\mathcal{E}}(T_i-T_e).\end{array}\right.\tag{73}$$

The system (73) has been obtained with the assumption that $\kappa/\beta \to 0$. In this case, we emphasize that (73) is a *closed* system: Corresponding to the hypothesis of large β the electromagnetic energy becomes negligible with respect to the mechanical one. Moreover in the definition of the mechanical energy (44)

$$\mathcal{E}=\frac{p_i+p_e}{\gamma-1}+\frac{1}{2}\rho_i\mathbf{u}_i^2+\frac{1}{2}\rho_e\mathbf{u}_e^2=\frac{p_i+p_e}{\gamma-1}+\frac{1}{2}\rho\mathbf{u}^2+\frac{m_em_i}{m_e+m_i}\frac{\mathbf{J}^2}{ne^2},\tag{74}$$

[3]To be more specific, we note that $\mathbf{E}$ being a 3-D vector field, the 3 components of this vector have no reason to have the same scales. In particular, Ohm's law shows that the parallel component (defined as $\mathbf{E}\cdot\mathbf{B}/|\mathbf{B}|$) of the electric field has no reason to scale with B_0u_0. A detailed analysis would therefore imply to use different scalings according to the different spatial directions. Here we simplify this analysis by introducing an additional parameter

the last term is of order $\mathcal{O}(c_i(\delta_e^*)^2/\beta)$ and thus must be neglected.

Let us remark that to obtain (73), we do not need to consider Ohm's law (72). In this sense, (73) is independent of the precise form of Ohm's that is used. However if we check for consistency the behaviour of Ohm's law in the limit $\beta \to +\infty$, we will get at the higher order in β:

$$\kappa \widetilde{\mathbf{E}} = -\sqrt{c_i}\delta_i^* \sqrt{\beta} \frac{T_{e,0}}{T_{e,0}+T_{i,0}} \frac{1}{\widetilde{n}} \widetilde{\nabla} \widetilde{p}_e + \sqrt{c_e}\delta_e^* \sqrt{\beta} \frac{T_{i,0}}{T_{e,0}+T_{i,0}} \frac{1}{\widetilde{n}} \widetilde{\nabla} \widetilde{p}_i, \tag{75}$$

and this relation establishes that the parameter κ (ratio between the electric field and the product $u_0 B_0$) has to scale with $\delta_i^* \sqrt{\beta}$ in the $\beta \to +\infty$ limit. Therefore the ratio $\kappa/\beta \to 0$ when $\beta \to +\infty$ and the scaling is self-consistent.

Note also that in this derivation of (73), we have never used any assumption on the electron mass. This system is therefore also relevant in the case where instead of electrons, a mixture of positive and negative ions is considered. However, in this case, there is no definite reason to choose the electronic entropy equation to close the system and another choice can be more physically relevant.

The system (73) can be also established using different assumptions. In [1], a bi-fluid model in the absence of any magnetic field is considered with the assumption that the two species have the same velocity. Then the comparison of the momentum equations from (36) (with $\mathbf{u}_e = \mathbf{u}_i = \mathbf{u}$) implies Ohm's law (75) from which a non-conservative system equivalent for smooth solutions to (73) is derived. The same assumptions (with in addition $m_e = 0$) is also used in [16].

System (73) is also considered in [36], with the assumption that the electron mass is small. The derivation we have presented here seems more general and do not rely on the strong assumptions of the absence of current and magnetic field and that the two species have the same velocities. It only requires quasi-neutrality and that the magnetic effects are weak.

The next subsection is devoted to a study of the mathematical properties of this system.

3.4 Properties of the bi-temperature Euler model

This subsection presents a mathematical study of (73) for the mono-atomic case (43). In [16], a mathematical study of the multi-fluid system with the equation on the electronic entropy is also presented. Since the bi-temperature Euler system is invariant by rotation, then it is sufficient to study the system in 1-D in the x-direction

$$\left\{ \begin{array}{lcl} \partial_t \rho + \partial_x(\rho u) & = & 0, \\ \partial_t(\rho u) + \partial_x(\rho u^2 + p_e + p_i) & = & 0, \\ \partial_t(\rho v) + \partial_x(\rho u v) & = & 0, \\ \partial_t(\rho w) + \partial_x(\rho u w) & = & 0, \\ \partial_t \mathcal{E} + \partial_x\left[(\mathcal{E} + p_e + p_i)u\right] & = & 0, \\ \partial_t(\rho_e S_e) + \partial_x(\rho_e S_e u) & = & (\gamma-1)\nu_{ei}^{\mathcal{E}} \rho_e^{1-\gamma}(T_i - T_e). \end{array} \right. \tag{76}$$

The system (76) is written in the form

$$\partial_t U + \partial_x F(U) = S(U),$$

where

$$U = \begin{bmatrix} \rho \\ \rho u \\ \rho v \\ \rho w \\ \mathcal{E} \\ \rho_e S_e \end{bmatrix}, \; F(U) = \begin{bmatrix} \rho u \\ \rho u^2 + p_e + p_i \\ \rho u v \\ \rho u w \\ (\mathcal{E} + p_e + p_i) u \\ \rho_e S_e u \end{bmatrix}, \; S(U) = \begin{bmatrix} 0 \\ 0 \\ 0 \\ 0 \\ 0 \\ (\gamma - 1)\nu_{ei}^{\mathcal{E}} \rho_e^{1-\gamma}(T_i - T_e) \end{bmatrix}.$$

In order to determine the eigensystem of the problem, we compute the Jacobian $A(U) = \partial_U F(U)$ and get

$$\begin{bmatrix} 0 & 1 & 0 & 0 & 0 & 0 \\ \frac{\gamma-3}{2}u^2 + \frac{\gamma-1}{2}(v^2+w^2) & (3-\gamma)u & (1-\gamma)v & (1-\gamma)w & \gamma - 1 & 0 \\ -uv & v & u & 0 & 0 & 0 \\ -uw & w & 0 & u & 0 & 0 \\ u\left[-\frac{c_s^2}{\gamma-1} + \frac{\gamma-2}{2}(u^2+v^2+w^2)\right] & \frac{c_s^2}{\gamma-1} + \frac{3-2\gamma}{2}u^2 + \frac{v^2+w^2}{2} & (1-\gamma)uv & (1-\gamma)uw & \gamma u & 0 \\ -c_e S_e u & c_e S_e & 0 & 0 & 0 & u \end{bmatrix}.$$

This matrix has three different eigenvalues given by

$$\begin{cases} \lambda_1 &= u - c_s, \\ \lambda_2 &= u, \\ \lambda_3 &= u + c_s, \end{cases} \tag{77}$$

where c_s is the sound speed of the mixture

$$c_s = \sqrt{\gamma \, \frac{p_e + p_i}{\rho}}.$$

Those eigenvalues and the definition of the sound speed of the mixture correspond to the one given in [16]. The eigenvalue λ_2 has an order of multiplicity of 4, and the eigenvectors R_1, R_2, and R_3, respectively associated to λ_1, λ_2, and λ_3, are given by

$$\left\{\begin{array}{rcl} R_1 & = & \begin{bmatrix} 1 \\ u-c_s \\ v \\ w \\ \dfrac{c_s^2}{\gamma-1}+\dfrac{u^2+v^2+w^2}{2}-uc_s \\ c_eS_e \end{bmatrix}, \quad R_2 \quad = \quad \begin{bmatrix} 1 \\ u \\ v \\ w \\ \dfrac{u^2+v^2+w^2}{2} \\ 1 \end{bmatrix}, \\ R_3 & = & \begin{bmatrix} 1 \\ u+c_s \\ v \\ w \\ \dfrac{c_s^2}{\gamma-1}+\dfrac{u^2+v^2+w^2}{2}+uc_s \\ c_eS_e \end{bmatrix}. \end{array}\right. \tag{78}$$

With the results (77) and (78), we find that the waves λ_1 and λ_3 are genuinely non linear and consequently those two waves can be shock or rarefaction waves. Concerning the wave λ_2, the computations lead to determine that this wave is linearly degenerate meaning that it is a contact discontinuity.

We now consider the Riemann problem with the initial data U_L, and U_R associated to the homogeneous conservative system

$$\partial_t U + \partial_x F(U) = 0.$$

The intermediate states are denoted U_L^* and U_R^* (see Figure 1). The Riemann invariants associated to each waves are

$$\begin{array}{lcl} (u-c_s)-\text{wave} & : & v,\ w,\ \rho_e p_e^{-\gamma},\ \rho_i p_i^{-\gamma},\ \text{and } u+\dfrac{2}{\gamma-1}c_s, \\ u-\text{wave} & : & u,\ \text{and } p_e+p_i, \\ (u+c_s)-\text{wave} & : & v,\ w,\ \rho_e p_e^{-\gamma},\ \rho_i p_i^{-\gamma},\ \text{and } u-\dfrac{2}{\gamma-1}c_s. \end{array}$$

For the 1-wave, associated to the $u-c_s$ eigenvalue, the shock and the rarefaction conditions are given by

$$\left\{\begin{array}{lll} \lambda_1(U_L) & \leq S_1 \leq & \lambda_1(U_L^*) \quad \text{Rarefaction condition,} \\ \lambda_1(U_L) & \geq S_1 \geq & \lambda_1(U_L^*) \quad \text{Shock condition,} \end{array}\right.$$

where S_1 is the speed of the 1-wave. To compute, the intermediate state U_L^* in the case of a 1-shock the Rankine-Hugoniot relation has to be used

$$F(U_L^*) - F(U_L) = S_1\left(U_L^* - U_L\right).$$

The Rankine-Hugoniot condition is not any more valuable for the 1-rarefaction and then the Riemann invariant of λ_1 are used to compute U_L^*.

Likewise, the shock and the rarefaction conditions for the 3-wave, associated to the $u+c_s$ eigenvalue, are given by

$$\left\{\begin{array}{lll} \lambda_3(U_R^*) & \leq S_3 \leq & \lambda_3(U_R) \quad \text{Rarefaction condition,} \\ \lambda_3(U_R^*) & \geq S_3 \geq & \lambda_3(U_R) \quad \text{Shock condition,} \end{array}\right.$$

where S_3 is the speed of the 3-wave. The Rankine-Hugoniot relation for the 3-shock is given by

$$F(U_R^*) - F(U_R) = S_3 \left(U_R^* - U_R\right).$$

For the 3-rarefaction, we use the Riemann invariants of λ_3 to get U_R^*. The four different cases are shown in Figure 1.

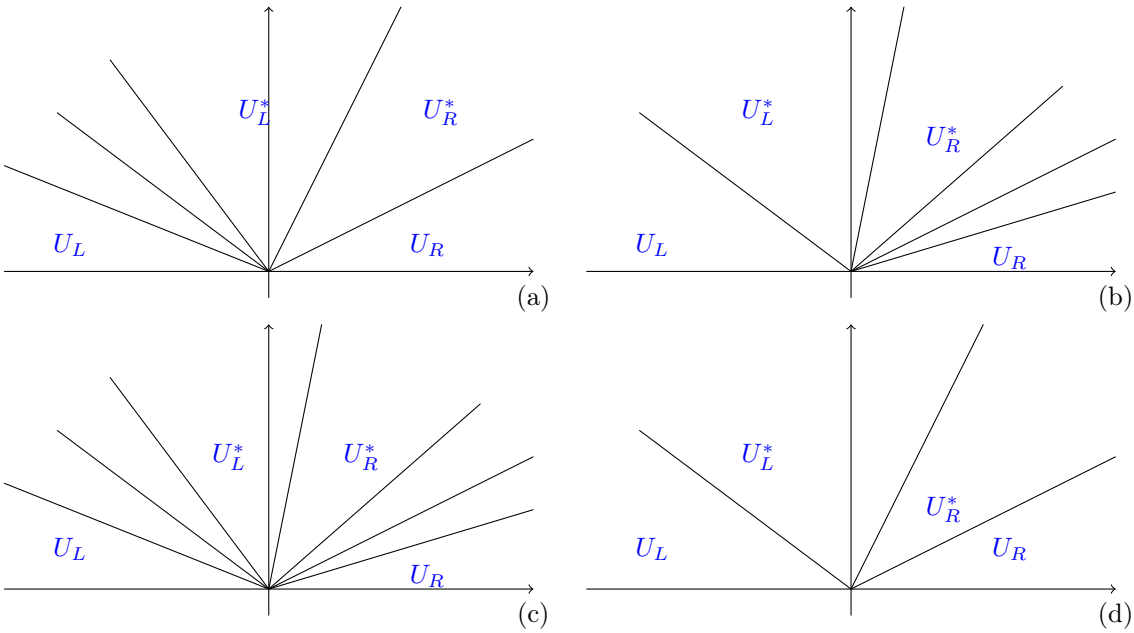

Figure 1: The four cases of Riemann problem for the bi-temperature Euler equation: (a) 1-Rarefaction and 3-Shock, (b) 1-Shock and 3-Rarefaction, (c) 1-Rarefaction and 3-Rarefaction, (d) 1-Shock and 3-Shock.

4 Finite volume method

This Section is devoted to the finite volume method. First, we give the general form of the method for a cell-centered with a 2-D mesh made of rectangles, and for a vertex-centered with 2-D mesh made of triangular elements. Then, we adapt the vertex-centered finite volume method to the toroidal geometry.

4.1 Generalities on finite volume method

Here, we consider a general hyperbolic conservative system written in the form

$$\partial_t U + \nabla \cdot F(U) = 0. \tag{79}$$

A tessellation is used to mesh the computational domain. Then, the control cells Ω are constructed. Let Ω be a typical control cell. We suppose that the solution U_Ω^n is known on the control cell Ω at the time t^n. In order to have the solution U_Ω^{n+1} at the time $t^{n+1} = t^n + \Delta t$

where Δt is obtained with a CFL-type condition [23, 31, 39, 25], the equation (79) is integrated over $\Omega \times \left[t^n, t^{n+1}\right]$

$$\int_\Omega \int_{t^n}^{t^{n+1}} \partial_t U(\mathbf{x},t) dt d\Omega + \int_{t^n}^{t^{n+1}} \int_\Omega \nabla \cdot F(U(\mathbf{x},t)) d\Omega dt = 0,$$

which is equivalent to

$$\int_\Omega U(\mathbf{x},t^{n+1}) d\Omega - \int_\Omega U(\mathbf{x},t^n) d\Omega + \int_{t^n}^{t^{n+1}} \int_\Omega \nabla \cdot F(U(\mathbf{x},t)) d\Omega dt = 0. \tag{80}$$

The solution U_Ω^n is defined as the average of U on the control cell Ω

$$U_\Omega^n = \frac{1}{|\Omega|} \int_\Omega U(\mathbf{x},t^n) dt d\Omega, \ |\Omega| = \int_\Omega d\Omega. \tag{81}$$

Hence, the equation (80) is equivalent to

$$U_\Omega^{n+1} = U_\Omega^n - \frac{1}{|\Omega|} \int_{t^n}^{t^{n+1}} \int_\Omega \nabla \cdot F(U(\mathbf{x},t)) d\Omega dt.$$

In our numerical tests, we only use explicit numerical fluxes then we have

$$U_\Omega^{n+1} = U_\Omega^n - \frac{\Delta t}{|\Omega|} \int_\Omega \nabla \cdot F(U(\mathbf{x},t^n)) d\Omega. \tag{82}$$

The computation of the numerical flux term $\int_\Omega \nabla \cdot F(U(\mathbf{x},t^n)) d\Omega$ depends on the approach and of the control cell form. The two next subsections are devoted to the computation of the numerical flux for both cell-centered and vertex-centered approaches.

4.1.1 2-D cell-centered finite volume on rectangular mesh

In this subsection, the computational domain used is a rectangle meshed with rectangular cells aligned with the x and the y-directions. Then, we denote N_x as the number of cells in the x-direction, and N_y as the number of cells in the y-direction. The control cells are now denoted $\Omega_{i,j}$ for $i = 1..N_x$ and $j = 1..N_y$. As shown in Figure 2, a typical control cell $\Omega_{i,j}$ [23] is defined by

$$\Omega_{i,j} = [x_{i-1/2}, x_{i+1/2}] \times [y_{j-1/2}, y_{j+1/2}], \ i = 1..N_x, \ j = 1..N_y.$$

The center point (x_i, y_j) of the cell is given by

$$\begin{cases} x_i &= \dfrac{x_{i-1/2} + x_{i+1/2}}{2}, \quad i = 1..N_x, \\ \\ y_j &= \dfrac{y_{j-1/2} + y_{j+1/2}}{2}, \quad j = 1..N_y. \end{cases}$$

We also define the space increments in x and y-directions

$$\begin{cases} \Delta x_i &= x_{i+1/2} - x_{i-1/2}, \quad i = 1..N_x, \\ \Delta y_j &= y_{j+1/2} - y_{j-1/2}, \quad j = 1..N_y. \end{cases}$$

According to the Cartesian coordinates, we rewrite the divergence as

$$\nabla \cdot F(U) = \partial_x F_x(U) + \partial_y F_y(U).$$

With all this description, we have

$$|\Omega_{i,j}| = \Delta x_i \Delta y_j,$$

and the equation (82) becomes

$$\begin{aligned} U_{i,j}^{n+1} = U_{i,j}^{n} \quad &- \quad \frac{\Delta t}{\Delta x_i \Delta y_j} \int_{x_{i-1/2}}^{x_{i+1/2}} \int_{y_{j-1/2}}^{y_{j+1/2}} \partial_x F_x(U) dx dy \\ &- \quad \frac{\Delta t}{\Delta x_i \Delta y_j} \int_{x_{i-1/2}}^{x_{i+1/2}} \int_{y_{j-1/2}}^{y_{j+1/2}} \partial_y F_y(U) dx dy, \end{aligned} \tag{83}$$

where $U_{i,j}^n$ is computed with the definition (81)

$$U_{i,j}^n = \frac{1}{\Delta x_i \Delta y_j} \int_{x_{i-1/2}}^{x_{i+1/2}} \int_{y_{j-1/2}}^{y_{j+1/2}} U(x, y, t^n) dx dy.$$

The equation (83) becomes

$$\begin{aligned} U_{i,j}^{n+1} = U_{i,j}^{n} \quad &- \quad \frac{\Delta t}{\Delta x_i \Delta y_j} \int_{y_{j-1/2}}^{y_{j+1/2}} \Big[F_x\Big(U(x_{i+1/2}, y, t^n)\Big) - F_x\Big(U(x_{i-1/2}, y, t^n)\Big) \Big] dy \\ &- \quad \frac{\Delta t}{\Delta x_i \Delta y_j} \int_{x_{i-1/2}}^{x_{i+1/2}} \Big[F_y\Big(U(x, y_{j+1/2}, t^n)\Big) - F_y\Big(U(x, y_{j-1/2}, t^n)\Big) \Big] dx. \end{aligned}$$

The numerical fluxes are defined by

$$\begin{aligned} F_{x,i+1/2,j}^n &= \frac{1}{\Delta y_j} \int_{y_{j-1/2}}^{y_{j+1/2}} F_x\Big(U(x_{i+1/2}, y, t^n)\Big) dy, \\ F_{y,i,j+1/2}^n &= \frac{1}{\Delta x_i} \int_{x_{i-1/2}}^{x_{i+1/2}} F_y\Big(U(x, y_{j+1/2}, t^n)\Big) dx. \end{aligned}$$

Those numerical fluxes are obtained with a Riemann type scheme in the numerical tests. Finally, the finite volume method for this 2-D cell-centered geometry is

$$U_{i,j}^{n+1} = U_{i,j}^n - \frac{\Delta t}{\Delta x_i} \left(F_{x,i+1/2,j}^n - F_{x,i-1/2,j}^n \right) - \frac{\Delta t}{\Delta y_j} \left(F_{y,i,j+1/2}^n - F_{y,i,j-1/2}^n \right).$$

In this case, the CFL condition is given by

$$\lambda_{max} \frac{\Delta t}{h_{min}} \leq 1.$$

There are a large various ways of chosing the coefficient λ_{max} [6, 18, 40]. For instance, this coefficient λ_{max} can be defined as the maximum of wave all over the computational domain. Indeed, for a cell $\Omega_{i,j}$, we denote

$$\lambda_{max,i,j} = \max_{\lambda \in Sp(A_{i,j}^n)} (|\lambda|), \;\; A_{i,j}^n = \partial_U F(U_{i,j}^n).$$

Then we have

$$\lambda_{max} = \max_{i=1..N_x, j=1..N_y} (\lambda_{max,i,j}).$$

The variable h_{min} is given by

$$h_{min} = \min(\Delta x_{min}, \Delta y_{min}),\ \Delta x_{min} = \min_{i=1..N_x} (\Delta x_i),\ \Delta y_{min} = \min_{j=1..N_y} (\Delta y_j).$$

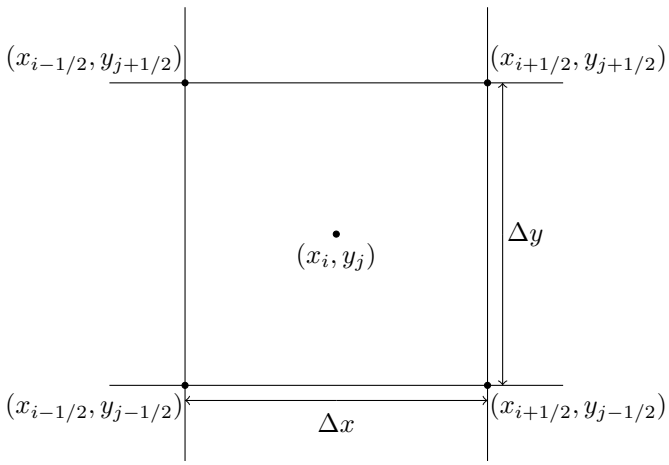

Figure 2: Representation of a control cell $\Omega_{i,j}$ in the cell-centered approach.

4.1.2 2-D vertex-centered finite volume on a triangular mesh

Here, we consider a triangulation of the computational domain. We denote N_τ the number of triangles and N_p the number of points in the mesh. For the vertex-centered approach [23, 41, 25], the control cells are constructed in the following way. Let us first consider a vertex i, with $i = 1..N_p$, the control cell associated is denoted Ω_i. Then,

$$\Omega_i = \bigcup_{\tau \in \mathcal{V}^\tau(i)} \Omega_i^\tau,$$

where $\mathcal{V}^\tau(i)$ is the set of the triangles in which i is a vertex, and Ω_i^τ is a subset of the triangle τ. To build Ω_i^τ, the triangle τ is divided in six equal triangles, which means that those triangles are formed with the three medians of the triangle. Then, Ω_i^τ is given by the two resulting triangles which share the vertex i (see Figure 3). Thus the surface of the control cell is

$$|\Omega_i| = \frac{1}{3} \sum_{\tau \in \mathcal{V}^\tau(i)} |\tau|, \tag{84}$$

where $|\tau|$ is the surface of the triangle τ.

Concerning the flux term of (82), we have

$$\int_{\Omega_i} \nabla \cdot F\Big(U(\mathbf{x}, t^n)\Big) d\Omega = \int_{\partial\Omega_i} F(U)\mathbf{n} d(\partial\Omega),$$

where $\partial\Omega_i$ is the boundary of the control cell Ω_i. According to the Figure 3, $\partial\Omega_i$ is

$$\partial\Omega_i = \bigcup_{j\in\mathcal{V}(i)} \partial\Omega_{ij},$$

where $\mathcal{V}(i)$ is the set of the neighbour point of i, and

$$\partial\Omega_{ij} = \Omega_i \bigcap \Omega_j,\ j \in \mathcal{V}(i).$$

Hence we have

$$\int_{\Omega_i} \nabla \cdot F\Big(U(\mathbf{x},t)\Big) d\Omega = \sum_{j\in\mathcal{V}(i)} \int_{\partial\Omega_{ij}} F(U)\mathbf{n} d(\partial\Omega).$$

The numerical flux is defined as

$$F_{ij}(U_i^n, U_j^n, \mathbf{n}_{ij}) = \frac{1}{|\partial\Omega_{ij}|} \int_{\partial\Omega_{ij}} F(U)\mathbf{n} d(\partial\Omega),\ |\partial\Omega_{ij}| = \int_{\partial\Omega_{ij}} d(\partial\Omega),$$

where

$$\mathbf{n}_{ij} = \frac{1}{\| \int_{\partial\Omega_{ij}} \mathbf{n} d\partial\Omega \|} \int_{\partial\Omega_{ij}} \mathbf{n} d\partial\Omega. \tag{85}$$

Finally the finite volume scheme for the vertex-centered approach presented is

$$U_i^{n+1} = U_i^n - \sum_{j\in\mathcal{V}(i)} \frac{\Delta t |\partial\Omega_{ij}|}{|\Omega_i|} F(U_i^n, U_j^n, \mathbf{n}_{ij}),$$

where the numerical fluxes are computed with a Riemann type scheme. The CFL condition is given by

$$\lambda_{max} \max_{i,j=1..N_p} \left(\frac{|\partial\Omega_{ij}|}{|\Omega_i|} \right) \Delta t \leq 1.$$

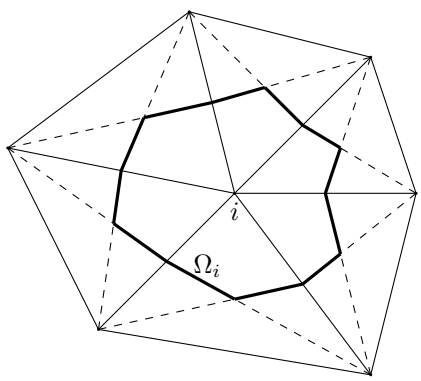

Figure 3: Representation of a control cell Ω_i in the vertex-centered approach.

4.2 Toroidal geometry

This subsection deals with the toroidal geometry and its adaptation to the finite volume method. First, the toroidal coordinates are presented with some mathematical properties. Next, the mesh design is explained with the computations of volumes, surfaces and unitary normals.

4.2.1 Cylindrical coordinates for toroidal problem and divergence form

The toroidal geometry is particularly useful for simulations taking place in a tokamak. Indeed, a tokamak can be modelled as a 2-D plane in rotation about an axis [12]. The 2-D plane is named poloidal plane. Hence, the axisymetric feature of a tokamak makes pertinent to use cylindrical coordinates.

Let us consider the Cartesian coordinates of a tokamak point $\mathbf{x} = (x, y, z)^T$. The relation between its Cartesian coordinates and its cylindrical coordinates $(R, Z, \varphi)^T$ is given by

$$\left\{ \begin{array}{lcl} x & = & R\cos\varphi, \\ y & = & R\sin\varphi, \\ z & = & Z, \end{array} \right.$$

where $R \in \mathbb{R}_+^*$, $\varphi \in [0, 2\pi[$, and $Z \in \mathbb{R}$.

The mapping $\Psi : \mathbb{R}^3 \to \mathbb{R}^3$, $\mathbf{x} = (x, y, z)^T \mapsto (R,\, Z,\, \varphi)^T$ leads to the following covariant basis:

$$\left\{ \begin{array}{lcl} \mathbf{e}_R & = & \partial_R x\ \mathbf{e}_x + \partial_R y\ \mathbf{e}_y + \partial_R z\ \mathbf{e}_z, \\ \mathbf{e}_Z & = & \partial_Z x\ \mathbf{e}_x + \partial_Z y\ \mathbf{e}_y + \partial_Z z\ \mathbf{e}_z, \\ \mathbf{e}_\varphi & = & \partial_\varphi x\ \mathbf{e}_x + \partial_\varphi y\ \mathbf{e}_y + \partial_\varphi z\ \mathbf{e}_z, \end{array} \right.$$

where $(\mathbf{e}_x, \mathbf{e}_y, \mathbf{e}_z)$ is the canonical base of $\mathbb{R}^3$. The Jacobian determinant of Ψ is

$$\mathbf{e}_R \cdot (\mathbf{e}_\varphi \times \mathbf{e}_Z) = R > 0,$$

which means that the transformation Ψ is one-to-one. The scaled covariant basis is useful and is given by

$$\widetilde{\mathbf{e}}_R = \frac{\mathbf{e}_R}{\|\mathbf{e}_R\|},\ \widetilde{\mathbf{e}}_Z = \frac{\mathbf{e}_Z}{\|\mathbf{e}_Z\|},\ \widetilde{\mathbf{e}}_\varphi = \frac{\mathbf{e}_\varphi}{\|\mathbf{e}_\varphi\|}.$$

It is also worthwhile to define the contravariant basis associated to the transformation Ψ. The contravariant basis $(\mathbf{e}^R, \mathbf{e}^Z, \mathbf{e}^\varphi)$ is defined by duality relations

$$\mathbf{e}_k.\mathbf{e}^l = \delta_k^l,$$

where δ_k^l is the Kronecker's symbol and $k, l = R, Z, \varphi$.

In the cylindrical coordinates, the divergence operator writes for a vector $\mathbf{V} = V_R\widetilde{\mathbf{e}}_R + V_Z\widetilde{\mathbf{e}}_Z + V_\varphi\widetilde{\mathbf{e}}_\varphi$

$$\nabla \cdot \mathbf{V} = \frac{1}{R}\partial_R(RV_R) + \partial_Z V_z + \frac{1}{R}\partial_\varphi V_\varphi.$$

For a tensor $\overline{\overline{T}}$ given by

$$\overline{\overline{T}} = \left[\begin{array}{ccc} T_{RR} & T_{RZ} & T_{R\varphi} \\ T_{ZR} & T_{ZZ} & T_{Z\varphi} \\ T_{\varphi R} & T_{\varphi Z} & T_{\varphi\varphi} \end{array} \right],$$

the divergence operator writes

$$
\begin{aligned}
(\nabla \cdot \overline{\overline{T}})_R &= \frac{1}{R}\partial_R(RT_{RR}) + \frac{1}{R}\partial_\varphi T_{R\varphi} + \partial_Z T_{RZ} - \frac{1}{R}T_{\varphi\varphi}, \\
(\nabla \cdot \overline{\overline{T}})_Z &= \frac{1}{R}\partial_R(RT_{ZR}) + \frac{1}{R}\partial_\varphi T_{Z\varphi} + \partial_Z T_{ZZ}, \\
(\nabla \cdot \overline{\overline{T}})_\varphi &= \frac{1}{R}\partial_R(RT_{\varphi R}) + \frac{1}{R}\partial_\varphi T_{\varphi\varphi} + \partial_Z T_{\varphi Z} + \frac{1}{R}T_{R\varphi}.
\end{aligned}
$$

The projection onto the cylidrical base $(\widetilde{\mathbf{e}}_R, \widetilde{\mathbf{e}}_Z, \widetilde{\mathbf{e}}_\varphi)$ of the vectorial equation

$$\partial_t \mathbf{V} + \nabla \cdot \overline{\overline{T}} = 0,$$

gives

$$
\left\{
\begin{array}{lcl}
\partial_t(RV_R) + \partial_R(RT_{RR}) + \partial_Z(RT_{RZ}) + \partial_\varphi T_{R\varphi} & = & T_{\varphi\varphi}, \\
\partial_t(RV_z) + \partial_R(RT_{ZR}) + \partial_Z(RT_{ZZ}) + \partial_\varphi T_{Z\varphi} & = & 0, \\
\partial_t(RV_\varphi) + \partial_R(RT_{\varphi R}) + \partial_Z(RT_{\varphi Z} + \partial_\varphi T_{\varphi\varphi} & = & -T_{R\varphi}.
\end{array}
\right.
$$

Then, artificial source terms are created by the spatial variation of the local basis. Therefore, to keep the strong conservative form of (79), we use the general definition of the divergence operator as it has been done in [12, 13]

$$\nabla \cdot \mathbf{V} = \frac{1}{R}\partial_k \left(R\mathbf{V} \cdot \mathbf{e}^k\right),$$

where $\mathbf{V}$ is either a vector or a tensor. In this formula, the Einstein summation convention is used. Taking $\mathbf{V} = U$ and $\overline{\overline{T}} = F(U)$, using the above definition of the divergence operator and considering R time independent lead to a conservative form of (79). It writes:

$$\partial_t(RU) + \partial_k \left(RF(U) \cdot \mathbf{e}^k\right) = 0. \tag{86}$$

Finally, the finite volume-type method is applied to this equation.

4.2.2 Mesh design and adaptation to the finite volume method

Concerning the simulation for the toroidal geometry, the vertex-centered approach is used. The mesh is designed in a way to take into account the axisymmetry of tokamak geometry as in [12, 13]. Let us first consider a 2-D mesh as the poloidal plane (R, Z) made of N_τ triangles. The 3-D mesh is generated by the rotation of this plane about the Z-axis between 0 and 2π.

The interval $[0, 2\pi]$ is divided in N_{plan} segments. Those segments are defined by the points $(\varphi_{j+1/2})_{0 \le j \le N_{plan}}$ with $\varphi_{1/2} = \varphi_{N_{plan}+1/2} = 0$ with a 2π-periodicity. We define the centers of the N_{plan} segments by

$$\varphi_j = \frac{\varphi_{j-1/2} + \varphi_{j+1/2}}{2}, \ j = 1...N_{plan}.$$

We denote R_0 the major radius of the torus, so that the radial coordinate can be rewritten as

$$R = R_0 + r, \ r \in \mathbb{R}_+.$$

A modelling of such a mesh is shown in Figure 4 where N_{2D} is the number of points in the 2-D mesh, Ω_i is the cell control of the 3-D point i, $\Omega^{2D}_{i_{2D}}$ is the 2-D cell control of the i_{2D} point in the poloidal plane. The global ordering of mesh points used is given by

$$i = (i_{2D} - 1)N_{plan} + j, \ i_{2D} = 1..N_{2D}, \ j = 1..N_{plan}.$$

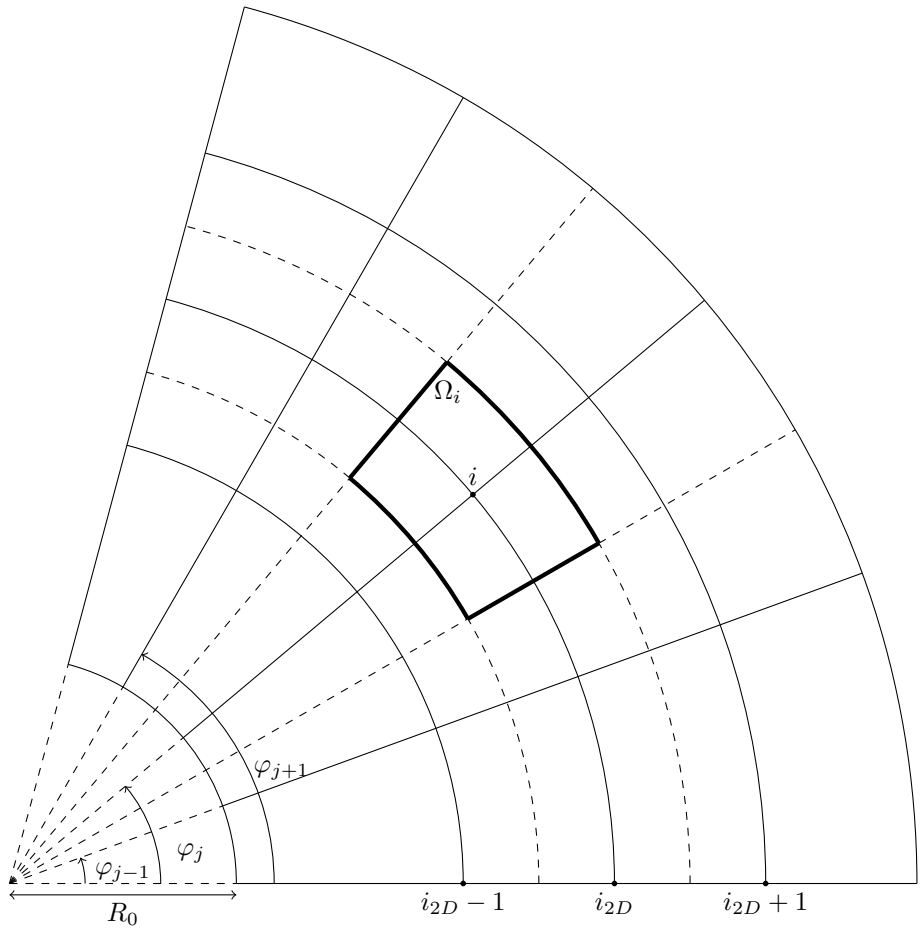

Figure 4: Projection on $\widetilde{\mathbf{e}}_\varphi$ of the Ω_i cell control.

The finite volume method for the hyperbolic system (86) using explicit time integration writes

$$\begin{aligned}&\int_{\Omega_i} RU(R,Z,\varphi,t^{n+1})dRdZd\varphi - \int_{\Omega_i} RU(R,Z,\varphi,t^{n})dRdZd\varphi\\&+\Delta t\int_{\Omega_i}\partial_k\left[RF\Big(U(R,Z,\varphi,t^n)\Big)\cdot\mathbf{e}^k\right]d\Omega = 0.\end{aligned} \tag{87}$$

Hence, the average value U_i^n is given by

$$U_i^n = \frac{1}{|\Omega_i|}\int_{\Omega_i} RU(R,Z,\varphi,t^n)dRdZd\varphi,\ |\Omega_i| = \int_{\Omega_i} RdRdZd\varphi.$$

According to the mesh design, the expression of the cell control volume writes

$$|\Omega_i| = \left(\int_{\Omega^{2D}_{i_{2D}}} RdRdZ\right)\left(\int_{\varphi_{j-1/2}}^{\varphi_{j+1/2}} d\varphi\right) = |\Omega^{2D}_{i_{2D}}|\Delta\varphi_j,$$

where $\Delta\varphi_j = \varphi_{j+1/2} - \varphi_{j-1/2}$, $j = 1...N_{plan}$. The surface $|\Omega^{2D}_{i_{2D}}|$ is given by

$$|\Omega^{2D}_{i_{2D}}| = \frac{1}{6} \sum_{\tau \in \mathcal{V}^\tau(i_{2D})} R^\tau_{i_{2D}} |\tau|,$$

with

$$R^\tau_{i_{2D}} = \frac{11}{9} R_{i_{2D}} + \frac{7}{18}(R_{l_{2D}} + R_{m_{2D}}),$$

with l_{2D} and m_{2D} are the two other vertices of τ.

The last term of (87) writes

$$\int_{\Omega_i} \partial_k \left[RF\Big(U(R,Z,\varphi,t^n)\Big) \cdot \mathbf{e}^k \right] d\Omega = \int_{\partial\Omega_i} R \left[F\Big(U(R,Z,\varphi,t^n)\Big) \cdot \mathbf{e}^k \right] \left(\mathbf{n} \cdot \mathbf{e}^k\right) d\partial\Omega.$$

Writing that $\partial\Omega_i = \bigcup \partial\Omega^b_i$ where $\partial\Omega^b_i$ are boundaries of the cell Ω_i, we have

$$\int_{\partial\Omega_i} R \left[F\Big(U(R,Z,\varphi,t^n)\Big) \cdot \mathbf{e}^k \right] \left(\mathbf{n} \cdot \mathbf{e}^k\right) d\partial\Omega = \sum_{\partial\Omega^b_i \in \partial\Omega_i} \int_{\partial\Omega^b_i} \left[RF\Big(U(R,Z,\varphi,t^n)\Big) \cdot \mathbf{e}^k \right] \left(\mathbf{n} \cdot \mathbf{e}^k\right) d\partial\Omega.$$

In the rest of this subsection, $(\widetilde{\mathbf{e}}_{R,j}, \widetilde{\mathbf{e}}_Z, \widetilde{\mathbf{e}}_{\varphi,j})$ is the cylindrical basis at the angle φ_j. In order to approach correctly flux integrals, we present here the different types of boundary surfaces and the computation linked to it. The boundary surfaces $\partial\Omega^b_i$ can be divided into three types:

- The surfaces $\partial\Omega^+_i$ of outgoing normal $\mathbf{n} = \widetilde{\mathbf{e}}_{\varphi,j+1/2}$,
- The surfaces $\partial\Omega^-_i$ of outgoing normal $\mathbf{n} = -\widetilde{\mathbf{e}}_{\varphi,j-1/2}$,
- The curved surfaces $\mathcal{S}_i$ directed along the toroidal direction $\widetilde{\mathbf{e}}_\varphi$,

with $\partial\Omega_i = \partial\Omega^+_i \bigcup \partial\Omega^-_i \bigcup \mathcal{S}_i$. To be more precise, the two first types of surfaces are similar and we have

$$\partial\Omega^\pm_i = \Omega^{2D}_{i_{2D}},$$

and

$$\int_{\partial\Omega^\pm_i} R \left[F(U,R,Z,\varphi,t^n) \cdot \mathbf{e}^k \right] (\mathbf{n} \cdot \mathbf{e}^k) d\partial\Omega = F\left(U^n_i, U^n_l, \pm\widetilde{\mathbf{e}}_{\varphi_{j\pm1/2}}\right) \int_{\Omega^{2D}_{i_{2D}}} dRdZ.$$

We deduce from (84) that

$$|\partial\Omega^\pm_i| = \frac{1}{3} \sum_{\tau \in \mathcal{V}^\tau(i_{2D})} |\tau|,$$

and

$$\int_{\partial\Omega^\pm_i} R \left[F(U,R,Z,\varphi,t^n) \cdot \mathbf{e}^k \right] (\mathbf{n} \cdot \mathbf{e}^k) d\partial\Omega = |\partial\Omega^\pm_i| F\left(U^n_i, U^n_l \pm \widetilde{\mathbf{e}}_{\varphi,j\pm1/2}\right),$$

where $l = i + N_{plan}$ for $\partial\Omega^+_i$ and $l = i - N_{plan}$ for $\partial\Omega^-_i$ the neighbours of i in the φ-direction.

Finally, the surface $\mathcal{S}_i$ is the rest of the boundary surfaces. It can be described as

$$S_i = \bigcup_{l \in \mathcal{V}^{2D}(i)} S_{il},$$

where $\mathcal{V}^{2D}(i)$ is the set of the neighbours of i in the poloidal plane. For $l \in \mathcal{V}^{2D}(i)$, the surface S_{il} is given by

$$S_{il} = \prod_{\varphi \in [\varphi_{j-1/2}, \varphi_{j+1/2}]} \mathcal{R}_\varphi\left(S^{2D}_{il}\right), \; S^{2D}_{il} = \Omega^{2D}_{i_{2D}} \bigcap \Omega^{2D}_{l_{2D}},$$

where i_{2D} and l_{2D} are the poloidal number of i and l, and the operator $\mathcal{R}_\varphi(S_{il}^{2D})$ is the rotation of S_{il}^{2D} around the Z-axis about the angle φ. To compute the numerical flux over the surface S_{il}, we write its unitary normal in the Cartesian coordinates

$$\mathbf{n} = \begin{bmatrix} n_R\cos(\varphi) \\ n_R\sin(\varphi) \\ n_Z \end{bmatrix}.$$

Then we have

$$\int_{\mathcal{S}_{il}} \left[RF\Big(U(R,Z,\varphi)\Big)\cdot \mathbf{e}^k\right]\left(\mathbf{n}\cdot\mathbf{e}^k\right) d\mathcal{S} = |\mathcal{S}_{il}| F\left(U_i^n, U_l^n, \mathbf{n}_{il}\right),$$

where $F(U_i^n, U_l^n, \mathbf{n}_{il})$ is the numerical flux determined with a Riemann-type scheme, and $\mathbf{n}_{il}$ is the average unitary normal of $\mathcal{S}_{il}$ given by the definition (85)

$$\begin{aligned}
\mathbf{n}_{il} &= \frac{1}{|\mathcal{S}_{il}|}\int_{\mathcal{S}_{il}} \mathbf{n} d\mathcal{S} = \frac{1}{|\mathcal{S}_{il}|}\int_{\mathcal{S}_{il}^{2D}} R d\mathcal{S}^{2D} \int_{\varphi_{j-1/2}}^{\varphi_{j+1/2}} \begin{bmatrix} n_R\cos(\varphi) \\ n_R\sin(\varphi) \\ n_Z \end{bmatrix} d\varphi, \\
&= \frac{|\mathcal{S}_{il}^{2D}|}{|\mathcal{S}_{il}|}\begin{bmatrix} 2n_R\cos\left(\dfrac{\Delta\varphi_j}{2}\right)\cos(\varphi_j) \\ 2n_R\cos\left(\dfrac{\Delta\varphi_j}{2}\right)\sin(\varphi_j) \\ n_Z\Delta\varphi_j \end{bmatrix},
\end{aligned}$$

where

$$|\mathcal{S}_{il}^{2D}| = \int_{\mathcal{S}_{il}^{2D}} R d\mathcal{S}^{2D}, |\mathcal{S}_{il}| = \int_{\mathcal{S}_{il}} R d\mathcal{S}.$$

Using the form of $\mathcal{S}_{il}$, we deduce that

$$|\mathcal{S}_{il}| = \Delta\varphi_j |\mathcal{S}_{il}^{2D}|.$$

Then, the normal $\mathbf{n}_{il}$ becomes

$$\mathbf{n}_{il} = \begin{bmatrix} \beta_j n_R\cos(\varphi_j) \\ \beta_j n_R\sin(\varphi_j) \\ n_Z \end{bmatrix}_{(\mathbf{e}_x,\mathbf{e}_y,\mathbf{e}_z)} = \begin{bmatrix} \beta_j n_R \\ n_Z \\ 0 \end{bmatrix}_{(\widetilde{\mathbf{e}}_{R,j},\widetilde{\mathbf{e}}_Z,\widetilde{\mathbf{e}}_{\varphi,j})}, \ \beta_j = \frac{\sin\left(\frac{\Delta\varphi_j}{2}\right)}{\frac{\Delta\varphi_j}{2}},$$

Finally, the finite volume method for the toroidal geometry writes

$$\begin{aligned}
U_i^{n+1} = U_i^n \quad &- \sum_{l\in\mathcal{V}^{2D}(i)} \left(\frac{|S_{il}|}{|\Omega_i|} F(U_i^n, U_l^n, \mathbf{n}_{il})\right) \\
&- \frac{|\partial\Omega_i^{\pm}|}{|\Omega_i|}\left[F\left(U_i^n, U_{i+N_{plan}}^n, \widetilde{\mathbf{e}}_{\varphi,j+1/2}\right) - F\left(U_{i-N_{plan}}^n, U_i^n, \widetilde{\mathbf{e}}_{\varphi,j-1/2}\right)\right].
\end{aligned}$$

For a scalar variable u, the average value is given by

$$u_i = \frac{1}{|\Omega_i|}\int_{\Omega_i} R u d\Omega.$$

Whereas the avarage value of a vectorial variable $\mathbf{u}$ is

$$\mathbf{u}_i = \frac{1}{|\Omega_i|}\int_{\Omega_i} R \begin{bmatrix} u_R \\ u_Z \\ u_\varphi \end{bmatrix}_{(\widetilde{\mathbf{e}}_R,\widetilde{\mathbf{e}}_Z,\widetilde{\mathbf{e}}_\varphi)} d\Omega.$$

As the cylindrical basis is moving in the control cell Ω_i and the finite volume method is applied to the entire vector, we have also to compute the average value of this basis in Ω_i. Hence, we have

$$\begin{cases} \mathbf{e}_{R,j} &= \dfrac{1}{|\Omega_i|}\displaystyle\int_{\Omega_i} R\widetilde{\mathbf{e}}_R d\Omega &= \beta_j \widetilde{\mathbf{e}}_{R,j}, \\ \mathbf{e}_{Z,j} &= \dfrac{1}{|\Omega_i|}\displaystyle\int_{\Omega_i} R\widetilde{\mathbf{e}}_Z d\Omega &= \widetilde{\mathbf{e}}_{Z,j}, \\ \mathbf{e}_{\varphi,j} &= \dfrac{1}{|\Omega_i|}\displaystyle\int_{\Omega_i} R\widetilde{\mathbf{e}}_\varphi d\Omega &= \beta_j \widetilde{\mathbf{e}}_{\varphi,j}. \end{cases}$$

Thus the average value of the vector $\mathbf{u}$ on Ω_i is

$$\mathbf{u}_i = \begin{bmatrix} \beta_j u_{R,i} \\ u_{Z,i} \\ \beta_j u_{\varphi,i} \end{bmatrix}.$$

We define the function μ_j^k

$$\mu_j^k = \begin{cases} \beta_j & \text{if} \quad k = R, \varphi, \\ 1 & \text{if} \quad k = Z. \end{cases}$$

Then, the finite volume method for each component of the $\mathbf{u}$ writes

$$\begin{aligned} \mathbf{u}_{k,i}^{n+1} = \mathbf{u}_{k,i}^n \quad &- \sum_{l\in\mathcal{V}^{2D}(i)} \left(\frac{|S_{il}|}{\mu_j^k |\Omega_i|} F(U_i^n, U_l^n, \mathbf{n}_{il}) \right) \\ &- \frac{|\partial\Omega_i^{\pm}|}{\mu_j^k |\Omega_i|} \left[F\left(U_i^n, U_{i+N_{plan}}^n, \widetilde{\mathbf{e}}_{\varphi,j+1/2}\right) - F\left(U_{i-N_{plan}}^n, U_i^n, \widetilde{\mathbf{e}}_{\varphi,j-1/2}\right) \right]. \end{aligned}$$

5 Relaxation scheme for the bi-temperature Euler model

This Section is devoted to the numerical scheme used to solve the bi-temperature Euler conservative equations (73). Using the rotational invariance of this system, a relaxation scheme is designed for the 1-D equations. The numerical scheme and the numerical experiments are presented for the mono-atomic case (43).

5.1 Presentation of the scheme

Here, we present the principle of the scheme used in the numerical tests. This scheme is a relaxation-type scheme based on the one designed for mono-temperature Euler equations in [14, 31, 39, 9, 8]. The relaxation scheme for bi-temperature Euler equations is given in [1] for the non-conservative system and detailed here for the conservative system (73). We relax the system

on the pressures of the two species $\alpha = e, i$. The relaxation variables are denoted π_α, $\alpha = e, i$. Hence, the relaxed system is given by

$$\left\{\begin{array}{lcl}
\partial_t\rho + \partial_x(\rho u) & = & 0, \\
\partial_t(\rho u) + \partial_x(\rho u^2 + \pi_e + \pi_i) & = & 0, \\
\partial_t(\rho v) + \partial_x(\rho u v) & = & 0, \\
\partial_t(\rho w) + \partial_x(\rho u w) & = & 0, \\
\partial_t(\mathcal{E}) + \partial_x\left[(\mathcal{E} + \pi_e + \pi_i)\, u\right] & = & 0, \\
\partial_t(\rho_e S_e) + \partial_x(\rho_e S_e u) & = & (\gamma - 1)\nu_{ei}^{\mathcal{E}}\rho_e^{1-\gamma}(T_i - T_e), \\
\partial_t\pi_e + \dfrac{a^2 c_e}{\rho}\partial_x u + u\partial_x\pi_e & = & \nu\left(p_e - \pi_e\right), \\
\partial_t\pi_i + \dfrac{a^2 c_i}{\rho}\partial_x u + u\partial_x\pi_i & = & \nu\left(p_i - \pi_i\right).
\end{array}\right.$$

According to [1], the parameter a has to satisfy the stability condition

$$a \geq \rho \max(c_{s,e}, c_{s,i}),\ c_{s,\alpha} = \sqrt{\frac{\gamma p_\alpha}{\rho_\alpha}},\ \alpha = e, i.$$

In order to have a more precise solution, the parameter a can be chosen as non-uniform variable. Then the relaxed system becomes

$$\left\{\begin{array}{lcl}
\partial_t\rho + \partial_x(\rho u) & = & 0, \\
\partial_t(\rho u) + \partial_x(\rho u^2 + \pi_e + \pi) & = & 0, \\
\partial_t(\rho v) + \partial_x(\rho u v) & = & 0, \\
\partial_t(\rho w) + \partial_x(\rho u w) & = & 0, \\
\partial_t(\mathcal{E}) + \partial_x\left[(\mathcal{E} + \pi_e + \pi_i)\, u\right] & = & 0, \\
\partial_t(\rho_e S_e) + \partial_x(\rho_e S_e u) & = & (\gamma - 1)\nu_{ei}^{\mathcal{E}}\rho_e^{1-\gamma}(T_i - T_e), \\
\partial_t\pi_e + \dfrac{a^2 c_e}{\rho}\partial_x u + u\partial_x\pi_e & = & \nu\left(p_e - \pi_e\right), \\
\partial_t\pi_i + \dfrac{a^2 c_i}{\rho}\partial_x u + u\partial_x\pi_i & = & \nu\left(p_i - \pi_i\right), \\
\partial_t(\rho a) + \partial_x(\rho a u) & = & 0.
\end{array}\right.$$

The system is now written in the hyperbolic conservative form

$$\partial_t U + \partial_x F(U) = S_\nu(U),$$

where

$$U = \begin{bmatrix} \rho \\ \rho u \\ \rho v \\ \rho w \\ \mathcal{E} \\ \rho_e S_e \\ \rho \pi_e \\ \rho \pi_i \\ \rho a \end{bmatrix}, \; F(U) = \begin{bmatrix} \rho u \\ \rho u^2 + \pi_e + \pi_i \\ \rho u v \\ \rho u w \\ (\mathcal{E} + \pi_e + \pi_i) \\ \rho_e S_e u \\ (\rho \pi_e + a^2 c_e) u \\ (\rho \pi_i + a^2 c_i) u \\ \rho a u \end{bmatrix}, \; S_\nu(U) = \begin{bmatrix} 0 \\ 0 \\ 0 \\ 0 \\ 0 \\ (\gamma - 1)\nu_{ei}^{\mathcal{E}} \rho_e^{1-\gamma}(T_i - T_e) \\ \nu(p_e - \pi_e) \\ \nu(p_i - \pi_i) \\ 0 \end{bmatrix}.$$

The relaxation scheme is composed of two steps: a transport step and a projection step. The transport step consists in solving the system

$$\partial_t U + \partial_x F(U) = 0, \tag{88}$$

with a Riemann type scheme. The projection step consists in taking the limit $\frac{1}{\nu} \to 0$ and solving the system

$$\partial_t U = S_\nu(U). \tag{89}$$

5.2 Transport step

5.2.1 Properties of the relaxed system

In this part, we construct the numerical flux of the Godunov scheme for the system (88). First, the system is rewritten in the form

$$\partial_t U + A(U)\partial_x U = 0,$$

where $A(U)$ is the Jacobian of $F(U)$ and is given by

$$A(U) = \begin{bmatrix} 0 & 1 & 0 & 0 & 0 & 0 & 0 & 0 & 0 \\ -(u^2 + \frac{\pi_e+\pi_i}{\rho}) & 2u & 0 & 0 & 0 & 0 & \frac{1}{\rho} & \frac{1}{\rho} & 0 \\ -uv & v & u & 0 & 0 & 0 & 0 & 0 & 0 \\ -uw & w & 0 & u & 0 & 0 & 0 & 0 & 0 \\ -\frac{u}{\rho}\left[\mathcal{E} + 2(\pi_e + \pi_i)\right] & \frac{1}{\rho}\left(\mathcal{E} + \pi_e + \pi_i\right) & 0 & 0 & u & 0 & \frac{u}{\rho} & \frac{u}{\rho} & 0 \\ -c_e u S_e & c_e S_e & 0 & 0 & 0 & u & 0 & 0 & 0 \\ -u\left(\pi_e + 3c_e\frac{a^2}{\rho}\right) & \pi_e + c_e\frac{a^2}{\rho} & 0 & 0 & 0 & 0 & u & 0 & 2c_e\frac{au}{\rho} \\ -u\left(\pi_i + 3c_i\frac{a^2}{\rho}\right) & \pi_i + c_i\frac{a^2}{\rho} & 0 & 0 & 0 & 0 & 0 & u & 2c_i\frac{au}{\rho} \\ -au & a & 0 & 0 & 0 & 0 & 0 & 0 & u \end{bmatrix}.$$

Hence, the matrix $A(U)$ has 3 eigenvalues given by

$$\begin{cases} \lambda_1 &= u - \dfrac{a}{\rho}, \\ \lambda_2 &= u, \\ \lambda_3 &= u + \dfrac{a}{\rho}. \end{cases}$$

where λ_2 has an order 7 of multiplicity. The eigenvectors obtained are

$$R_1 = \begin{bmatrix} 1 \\ u - \dfrac{a}{\rho} \\ v \\ w \\ \dfrac{1}{\rho}(\mathcal{E} + \pi_e + \pi_i - au) \\ c_e S_e \\ \pi_e + c_e \dfrac{a^2}{\rho} \\ \pi_i + c_i \dfrac{a^2}{\rho} \\ a \end{bmatrix}, \; R_2 = \begin{bmatrix} 1 \\ u \\ 1 \\ 1 \\ 1 \\ 1 \\ \pi_e \\ \pi_i \\ a \end{bmatrix}, R_3 = \begin{bmatrix} 1 \\ u + \dfrac{a}{\rho} \\ v \\ w \\ \dfrac{1}{\rho}(\mathcal{E} + \pi_e + \pi_i + au) \\ c_e S_e \\ \pi_e + c_e \dfrac{a^2}{\rho} \\ \pi_i + c_i \dfrac{a^2}{\rho} \\ a \end{bmatrix}.$$

The three waves are linearly degenerated hence, they are contact discontinuities. The Riemann invariants are

$$\begin{aligned}
(u - \frac{a}{\rho}) - \text{wave} \quad &: \quad u - \frac{a}{\rho},\ v,\ w,\ a,\ S_e,\ \pi_e + c_e \frac{a^2}{\rho},\ \pi_i + c_i \frac{a^2}{\rho},\ \text{and } \varepsilon - \frac{1}{2c_e a^2}\pi_e^2 - \frac{1}{2c_i a^2}\pi_i^2, \\
u - \text{wave} \quad &: \quad u,\ \text{and } \pi_e + \pi_i, \\
(u + \frac{a}{\rho}) - \text{wave} \quad &: \quad u + \frac{a}{\rho},\ v,\ w,\ a,\ S_e,\ \pi_e + c_e \frac{a^2}{\rho},\ \pi_i + c_i \frac{a^2}{\rho},\ \text{and } \varepsilon - \frac{1}{2c_e a^2}\pi_e^2 - \frac{1}{2c_i a^2}\pi_i^2,
\end{aligned}$$

where ε is the total internal energy defined by

$$\rho\varepsilon = \rho_e \varepsilon_e + \rho_i \varepsilon_i,\ \rho_\alpha \varepsilon_\alpha = (\gamma - 1) p_\alpha,\ \alpha = e, i.$$

In [1], the Riemann invariants are almost the same ones. Indeed, for the $(u - \frac{a}{\rho})$ and $(u + \frac{a}{\rho})$-waves, instead of giving the Riemann invarations on the internal energy of each species, we give the ones on the electronic entropy and the total internal energy. This difference comes from the fact that we consider the conservative system instead of the non-conservative one.

5.2.2 Relaxation flux

In this part, we consider the Riemann problem with the initial data (U_L, U_R) and compute the 2 intermediate states U_L^* and U_R^*, as shown in Figure 5). Since the three waves are contact discontinuities, we use the Riemann invariants to obtain the two intermediate states. For the 2-wave, u and $\pi_e + \pi_i$ are invariant, hence we have

$$\left\{ \begin{array}{lllll} u_L^* & = & u_R^* & = & u^*, \\ \pi_{e,L}^* + \pi_{i,L}^* & = & \pi_{e,R}^* + \pi_{i,R}^* & = & \pi^*. \end{array} \right. \tag{90}$$

For the rest of the Riemann invariants we obtain the following system for the 1-wave

$$\left\{\begin{array}{lcl} u_L - \dfrac{a_L}{\rho_L} & = & u^* - \dfrac{a_L}{\rho_L^*}, \\[2ex] \pi_{e,L} + c_e \dfrac{a_L^2}{\rho_L} & = & \pi_{e,L}^* + c_e \dfrac{a_L^2}{\rho_L^*}, \\[2ex] \pi_{i,L} + c_i \dfrac{a_L^2}{\rho_L} & = & \pi_{i,L}^* + c_i \dfrac{a_L^2}{\rho_L^*}, \\[2ex] \varepsilon_L - \dfrac{1}{2c_e a_L^2}\pi_{e,L}^2 - \dfrac{1}{2c_i a_L^2}\pi_{i,L}^2 & = & \varepsilon_L^* - \dfrac{1}{2c_e a_L^2}(\pi_{e,L}^*)^2 - \dfrac{1}{2c_i a_L^2}(\pi_{i,L}^*)^2. \end{array}\right. \tag{91}$$

The 3-wave Riemann invariants give the last system

$$\left\{\begin{array}{lcl} u_R + \dfrac{a_R}{\rho_R} & = & u^* - \dfrac{a_R}{\rho_R^*}, \\[2ex] \pi_{e,R} + c_e \dfrac{a_L^2}{\rho_R} & = & \pi_{e,R}^* + c_e \dfrac{a_R^2}{\rho_R^*}, \\[2ex] \pi_{i,R} + c_i \dfrac{a_L^2}{\rho_R} & = & \pi_{i,R}^* + c_i \dfrac{a_R^2}{\rho_R^*}, \\[2ex] \varepsilon_R - \dfrac{1}{2c_e a_R^2}\pi_{e,R}^2 - \dfrac{1}{2c_i a_R^2}\pi_{i,R}^2 & = & \varepsilon_R^* - \dfrac{1}{2c_e a_R^2}(\pi_{e,R}^*)^2 - \dfrac{1}{2c_i a_R^2}(\pi_{i,R}^*)^2. \end{array}\right. \tag{92}$$

By solving simultaneously the systems (90), (91), and (92), we obtain

$$\frac{1}{\rho_L^*} = \frac{1}{\rho_L} + \frac{a_R(u_R - u_L) + (\pi_{e,L} + \pi_{i,L}) - (\pi_{e,R} + \pi_{i,R})}{a_L(a_L + a_R)},$$

$$\frac{1}{\rho_R^*} = \frac{1}{\rho_R} + \frac{a_L(u_R - u_L) + (\pi_{e,R} + \pi_{i,R}) - (\pi_{e,L} + \pi_{i,L})}{a_R(a_L + a_R)},$$

$$u^* = \frac{a_L u_L + a_R u_R + (\pi_{e,L} + \pi_{i,L}) - (\pi_{e,R} + \pi_{i,R})}{a_L + a_R},$$

$$\pi_{\alpha,L}^* = \pi_{\alpha,L} - c_\alpha a_L \frac{a_R(u_R - u_L) + (\pi_{e,L} + \pi_{i,L}) - (\pi_{e,R} + \pi_{i,R})}{a_L + a_R}, \ \alpha = e, i,$$

$$\pi_{\alpha,R}^* = \pi_{\alpha,R} - c_\alpha a_R \frac{a_L(u_R - u_L) + (\pi_{e,R} + \pi_{i,R}) - (\pi_{e,L} + \pi_{i,L})}{a_L + a_R}, \ \alpha = e, i,$$

$$\varepsilon_K^* = \varepsilon_K + \frac{1}{2c_e a_K^2}\left[(\pi_{e,K}^*)^2 - \pi_{e,K}^2\right] + \frac{1}{2c_i a_K^2}\left[(\pi_{i,K}^*)^2 - \pi_{i,K}^2\right], \ K = L, R.$$

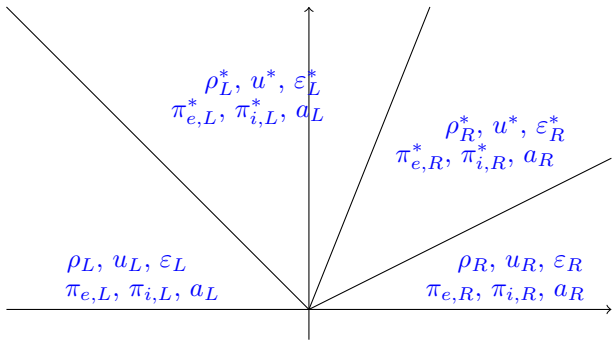

Figure 5: Riemann fan for the relaxed system (88).

The solution of the Riemann problem is given by

$$U^* = \begin{cases} U_L & \text{if} \quad 0 \leq \lambda_1, \\ U_L^* & \text{if} \quad \lambda_1 \leq 0 \leq \lambda_2, \\ U_R^* & \text{if} \quad \lambda_2 \leq 0 \leq \lambda_3, \\ U_R & \text{if} \quad \lambda_3 \leq 0. \end{cases}$$

Then, the flux of the relaxation scheme is

$$F^* = F(U^*).$$

In order to maintain a positive density and a positive internal energy, the parameter a has to fulfill the following conditions

$$\begin{cases} a_L(a_L + a_R) & \geq & \rho_L \left[(\pi_{e,R} + \pi_{i,R}) - (\pi_{e,L} + \pi_{i,L}) - a_R(u_R - u_L) \right], \\ a_R(a_L + a_R) & \geq & -\rho_R \left[(\pi_{e,R} + \pi_{i,R}) - (\pi_{e,L} + \pi_{i,L}) + a_L(u_R - u_L) \right]. \end{cases}$$

5.3 Projection step

During the projection step, we take the limit $\dfrac{1}{\nu} \to 0$. Hence, the system (89) is re-written as function of the physical variable $(\rho, u, v, w, \pi_e, \pi_u, T_e, T_i)^T$

$$\begin{cases} \partial_t \rho & = & 0, \\ \partial_t u & = & 0, \\ \partial_t v & = & 0, \\ \partial_t w & = & 0, \\ \pi_e & = & p_e, \\ \pi_i & = & p_i, \\ \partial_t T_e & = & \nu_{ei}(T_i - T_e), \\ \partial_t T_i & = & -\nu_{ie}(T_i - T_e), \end{cases}$$

where the temperature is in electron-Volt (eV). The coefficient $\nu_{\alpha\beta}$ is related to the coefficient $\nu_{ei}^{\mathcal{E}}$ defined in (19)

$$\nu_{\alpha\beta} = (\gamma - 1)\frac{\nu_{ei}^{\mathcal{E}}}{n_\alpha k_B}, \ \alpha = e, i.$$

For pratical implementation, we use the value of the coefficient $\nu_{\alpha\beta}$ given by the NRL formulary [28] at the page 34

$$\nu_{\alpha\beta} = 1.8 \times 10^{-19} \frac{\sqrt{m_e m_i}\lambda_{ei}}{(m_i T_e + m_e T_i)^{3/2}} s^{-1}, \tag{93}$$

and λ_{ei} is the Coulomb logarithm also defined by the NRL formulary [28] given at the same page

$$\lambda_{ei} = \begin{cases} 23 - \ln\left(\dfrac{\sqrt{n_e}}{T_e^{-3/2}}\right), & \dfrac{m_e}{m_i} T_i < T_e < 10eV, \\ \\ 24 - \ln\left(\dfrac{\sqrt{n_e}}{T_e}\right), & \dfrac{m_e}{m_i} T_i < 10eV < T_e. \end{cases} \tag{94}$$

In (93) and (94), the temperatures T_e, and T_i are in eV, the mass are expressed in g, and n_e is in cm^{-3}.

The final temperatures T_e^{n+1} and T_i^{n+1} are given by

$$\begin{cases} T_e^{n+1} &= -\dfrac{\nu_{ei}}{\nu_{ei}+\nu_{ie}}(T_i^n - T_e^n)e^{-(\nu_{ei}+\nu_{ie})\Delta t} + \dfrac{\nu_{ie}T_e^n + \nu_{ei}T_i^n}{\nu_{ei}+\nu_{ie}}, \\ \\ T_i^{n+1} &= \dfrac{\nu_{ie}}{\nu_{ei}+\nu_{ie}}(T_i^n - T_e^n)e^{-(\nu_{ei}+\nu_{ie})\Delta t} + \dfrac{\nu_{ie}T_e^n + \nu_{ei}T_i^n}{\nu_{ei}+\nu_{ie}}. \end{cases}$$

where T_e^n and T_i^n are the temperatures obtained with the transport step. We then get the relaxation time t_{relax} given by

$$t_{relax} = \frac{1}{\nu_{ei} + \nu_{ie}}. \tag{95}$$

At this end, we compute the new total energy and the new electronic entropy with (27), (44) and (49) in the S.I. units. To do so, the temperatures need to be express in Kelvin (K). The relation between the temperature T^{eV} in eV and the temperature T^K in K is given by

$$T^{eV} = 1.1604 \times 10^4 T^K.$$

6 Numerical tests

For all the numerical tests, the computations have been done with a second order in time and space scheme. The time integration has used a second order Runge-Kutta method while second order in space used a MUSCL method on non-structured meshes described in [25].

6.1 Shock tube

This test case is inspired by the well-known Sod's tube for Euler equations [38] and intends to test the transport step of the proposed numerical method. This test has been run in a 2-D setting on a square $[0,1] \times [0,1]$ meshed with 200×5 points. The computation is carried out until $t = 8.6289 \times 10^{-8} s$. The initial data writes

$$U(x,y) = \begin{cases} U_L, & \text{if} \quad x < 0.5, \\ U_R, & \text{if} \quad x \geq 0.5, \end{cases}$$

where U_L and U_R are given in Table 1. The initial data of the density are the usual ones, and the initial temperatures are chosen in order to keep as in [38] a ratio of 10 between the pressures of the left and right states.

	ρ	$\mathbf{u}$	T_e(K)	T_i(K)
U_L	1	0	1.04436×10^8	1.27644×10^8
U_R	0.125	0	8.1228×10^7	1.04436×10^8

Table 1: Initial data for the shock tube problem.

This solution of this problem contains three different waves: one rarefaction, one contact discontinuity, and one shock.

In order to test the transport part of the numerical method, the simulation is first realized without any source term: $\nu_{ei} = \nu_{ie} = 0$. The results are given in Figure 6. As expected, the solution is 1-D, and although the simulation has been done on a 2D mesh, the numerical scheme does not generate transverse velocities. The density follows correctly the three waves. Concerning the temperatures, we observe an overshoot at the beginning of the contact discontinuity around $x = 0.64$. With respect to the entropies, it is seen that as it has been shown by the mathematical study of the bi-temperature Euler equations, the electronic entropy is constant across the shock wave at $x \approx 0.84$ in Figure 6 while on the opposite the ionic entropy jumps across the shock.

In a second simulation, we now add the temperature relaxation source terms where ν_{ei} and ν_{ie} are given by (93). The obtained results on the electronic and ionic temperatures, pressures, and entropy are given in Figure 7 again for $t = 8.6289 \times 10^{-8} s$. According to Table 1, the equilibrium times for the left and the right states are

$$\left\{ \begin{array}{lcl} t_{eq,L} & = & 2.39 \times 10^{-8} s, \\ t_{eq,R} & = & 1.21 \times 10^{-7} s, \end{array} \right.$$

and therefore, the computation is stopped before the time where the two temperatures should have attained a common value. This time is also called thermal equilibrium time and corresponds to the relaxation time (95) denoted t_{eq}. Actually, the results show that on the left side where the relaxation time is smaller the thermal equilibrium is reached before the contact discontinuity while the two temperatures are still significantly different on the right side.

We can also see that the temperature relaxation modifies the entropies and that the electronic entropy is not any more constant across the shock wave. By comparing Figures 6 and 7, this effect is less apparent for the ionic entropy that seems to be less affected by the temperature relaxation. One can suspect that this behaviour is probably a direct consequence of the large difference of mass between the two species.

The numerical method gives satisfactory results on this problem and thus validate the numerical treatment of the transport step.

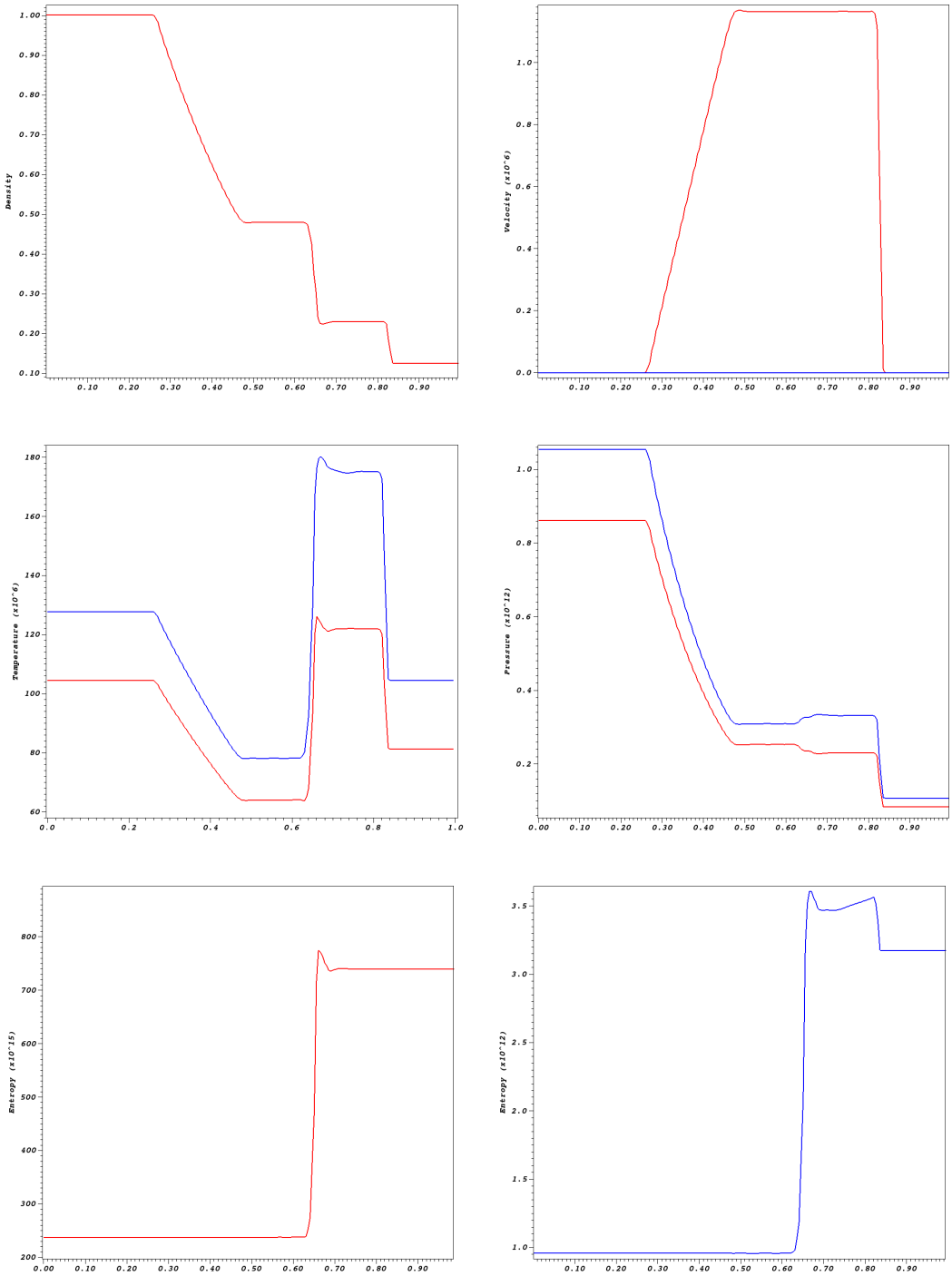

Figure 6: Shock tube problem at $t = 8.6289 \times 10^{-8} s$ with $\nu_{ei} = \nu_{ie} = 0$. Solution at $y = 0.5$. Left-Top: Density, Right-Top: x-velocity in red, and y-velocity in blue, Left-Center: Electronic (red) and ionic (blue) temperatures, Right-Center: Electronic (red) and ionic(blue) pressures, Left-Bottom: Electronic entropy, Right-Bottom: Ionic entropy.

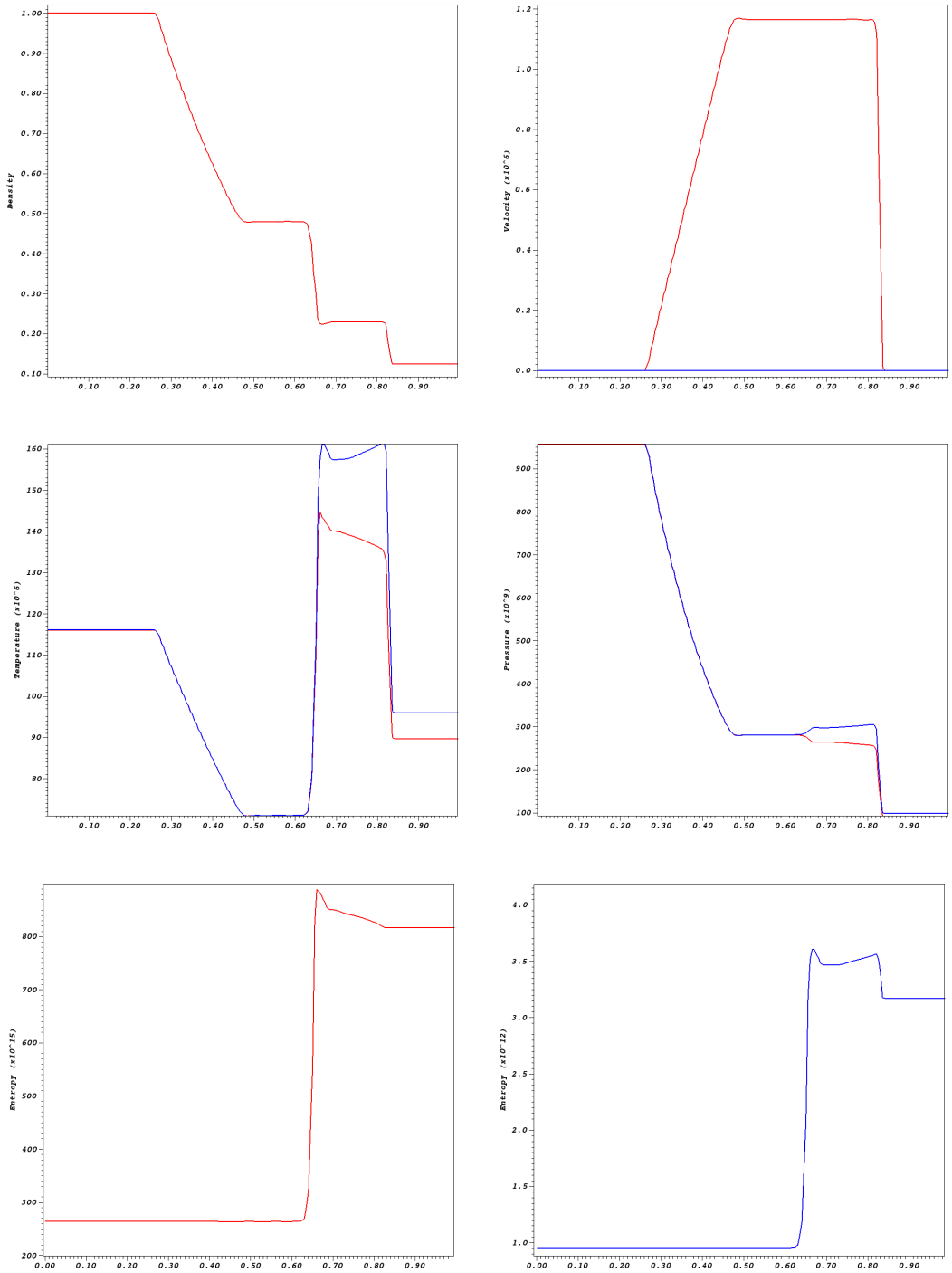

Figure 7: Shock tube problem at $t = 8.6289 \times 10^{-8} s$ with $\nu_{ei} \neq 0$, $\nu_{ie} \neq 0$. Solution at $y = 0.5$. Left-Top: Density, Right-Top: x-velocity in red, and y-velocity in blue, Left-Center: Electronic (red) and ionic (blue) temperatures, Right-Center: Electronic (red) and ionic(blue) pressures, Left-Bottom: Electronic entropy, Right-Bottom: Ionic entropy.

6.2 Implosion

This test case is inspired from [17] and adapted to the bi-temperature Euler equations. Indeed, the density and velocity initial data are the same as the ones used in [17]. The physical motivation of this test is to simulate a laser beam shooting a target in order to initiate a fusion reaction. Then, for this test, the temperatures are chosen in order to be in the laser plasma domain given in page 41 of the NRL formulary [28]. From a computational point of view, we test in this simulation the capability of the numerical scheme to handle shock focusing and reflection leading to a large and fast increase of the density. The initial data is given by

$$U(x,y) = \begin{cases} U_L, & \text{if} \quad r < 0.5, \\ U_R, & \text{if} \quad r \geq 0.5, \end{cases}, \; r = \sqrt{x^2+y^2}.$$

where the data U_L and U_R are given in Table 2.

This test has been computed in a 2-D Cartesian geometry on a simulation domain equal to a quarter of disc of radius equal to 1 meshed by 33153 points. The mesh is a refined version of the mesh presented in Figure 8. Since we want to compute the reflection of the shock wave at the origin, it has not been possible to use a polar grid that contains very small cells at the origin and thus implies the use of very small time steps. The mesh used is a good approximation of a polar mesh: the constant radius lines are almost mesh lines. However, this is not exactly true and will lead to some numerical artefacts.

This problem contains three cylindrical waves propagating towards the origin: first a shock, followed by a contact discontinuity leaving behind it a rarefaction wave. After interacting with the origin the shock will be reflected back and will propagate towards the exterior. Eventually, the reflected shock will interact with the contact discontinuity that is still propagating towards the center. At the initial time, the equilibrium temperature times for the left and the right states are

$$\begin{cases} t_{eq,L} &= 1.34 \times 10^{-10} s, \\ t_{eq,R} &= 2.97 \times 10^{-9} s, \end{cases}$$

that are quite small. Figures 9 and 10 present the results obtained at the time $t_1 = 4.0901 \times 10^{-7} s$ before the interaction of the shock with the origin. Since t_1 is significantly larger than the temperature relaxation times, the electronic and ionic temperatures had time to relax to a common value as shown on the color plot of Figure 9 and the 1-D plot of Figure 10 where the electronic and ionic pressures and temperatures are the same.

Since the initial data depends only on r, we expect a 1-D solution in a cylindrical coordinates system r, θ. As shown in Figures 9 and 11, this property is satisfied by the simulation except on the contact discontinuity where small wiggles appears. These wiggles grow along time. This loss of the 1-D character of the solution is not seen on the propagation of the shock wave but appears on the contact discontinuity. It is likely that these wiggles are initiated by the fact that the mesh is not exactly aligned with the initial data and that they are amplified by some kind of Richtmyer-Meshkov type instability although we do not claim that they have a physical origin.

Figures 11 and 12 present the results at $t = t_2 = 6.22 \times 10^{-7} s$ shortly after the reflection of the shock. The density and pressure at the origin have increased by a factor ten and a zone of positive velocity can be noticed while the contact discontinuity is still moving towards the center.

Finally at $t = t_3 = 8.4973 \times 10^{-7} s$ the shock begins to interact with the contact discontinuity. In Figure 13 are displayed the evolution of the density contours at times t_1, t_2, t_3, that show the development of instabilities on the contact discontinuity with mushroom shapes. However the mesh resolution for this computation is too coarse to pretend to capture a true physical instability

and the contact is smeared over several cells. This is a well-know problem in the computation of linearly degenerate-waves by Eulerian methods and is often taken as an argument to prefer Lagrangian methods for multi-material problems and specially for ICF simulations [34, 35, 22].

	ρ	$\mathbf{u}$	T_e(K)	T_i(K)
U_L	1	0	2.3×10^6	1.7406×10^6
U_R	1	0	2.3×10^7	1.7406×10^7

Table 2: Initial data for the implosion problem.

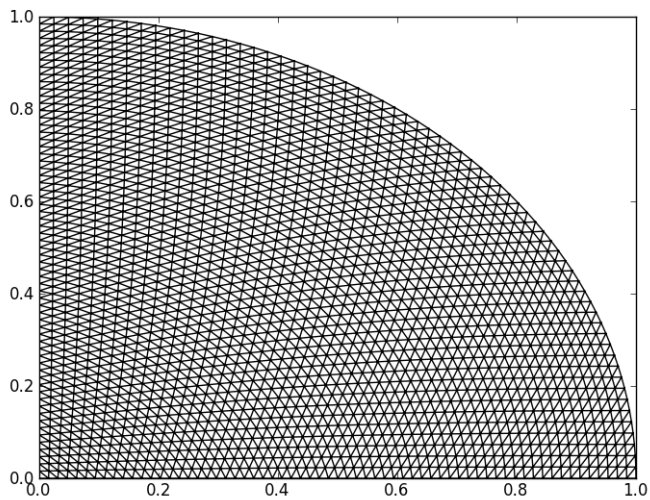

Figure 8: Implosion problem, Similar mesh with 2145 points as the one used in numerical simulation. The meshed used in Section 6.2 has been obtained by a refinement of a factor 4 from the present one and contains 33153($\approx 4 \times 4 \times 2145$).

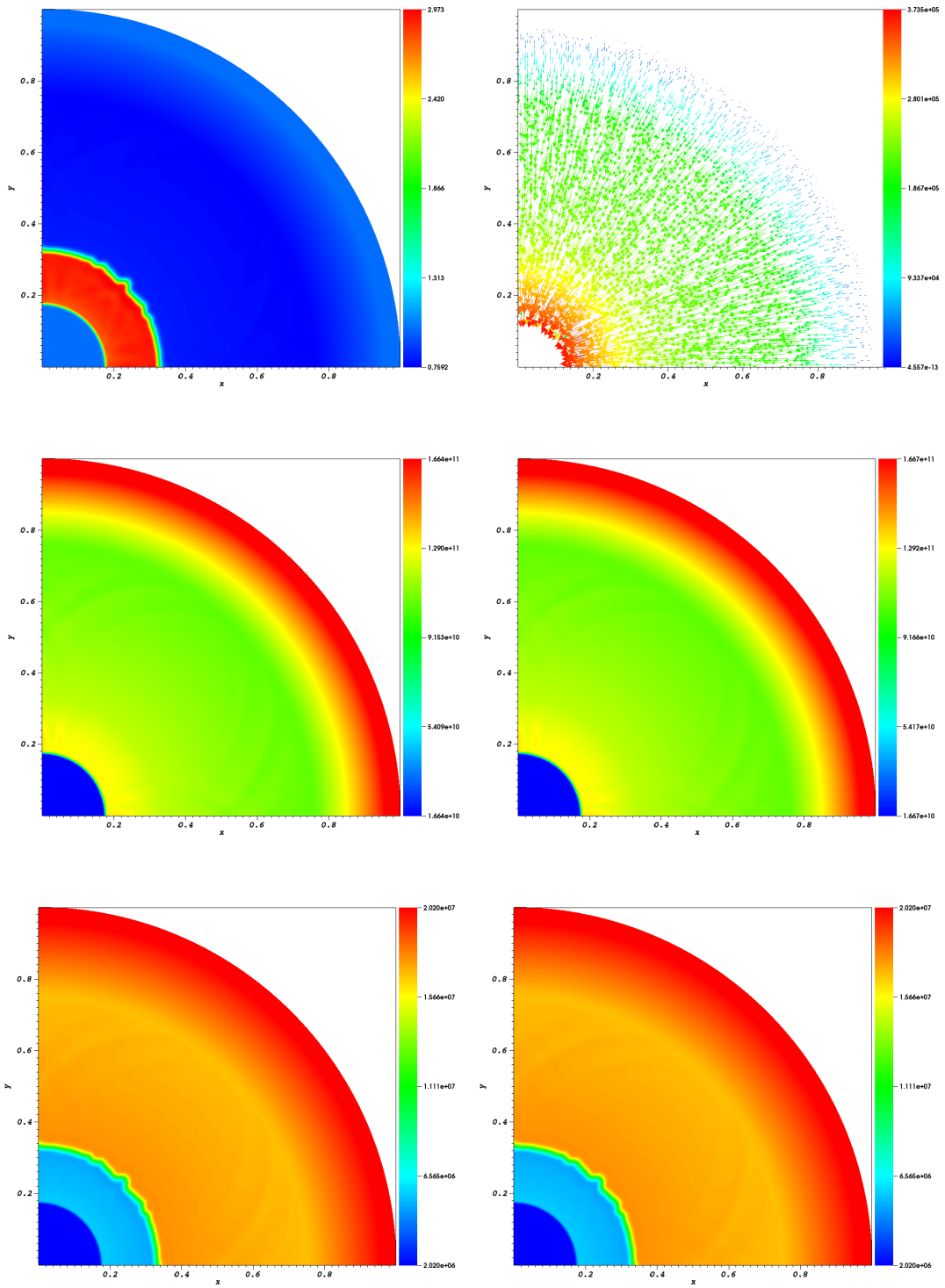

Figure 9: Implosion problem at $t_1 = 4.0901 \times 10^{-7} s$. 2-D fields of Left-Top: Density, Right-Top: Velocity, Left-Center: Electronic pressure, Right-Center: Ionic pressure, Left-Bottom: Electronic temperature, Right-Bottom: Ionic temperature.

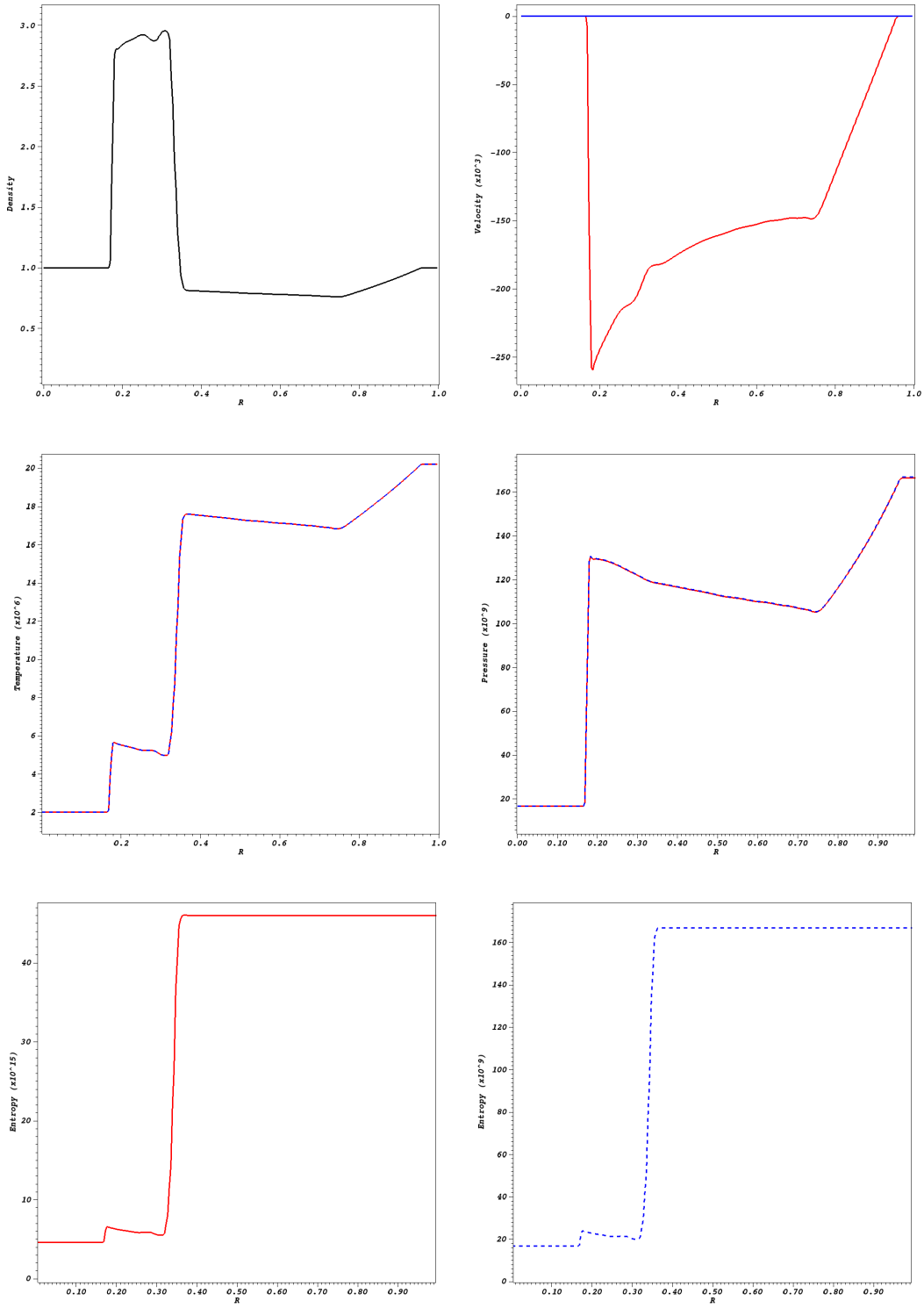

Figure 10: Implosion problem at $t_1 = 4.0901 \times 10^{-7} s$. 1-D fields at $y = x$ of Left-Top: Density, Right-Top: Radial (red) and tangential (blue) velocities, Left-Center: Electronic (red) and ionic (blue) temperatures, Right-Center: Electronic (red) and ionic (blue) pressures, Left-Bottom: Electronic entropy, Right-Bottom: Ionic entropy.

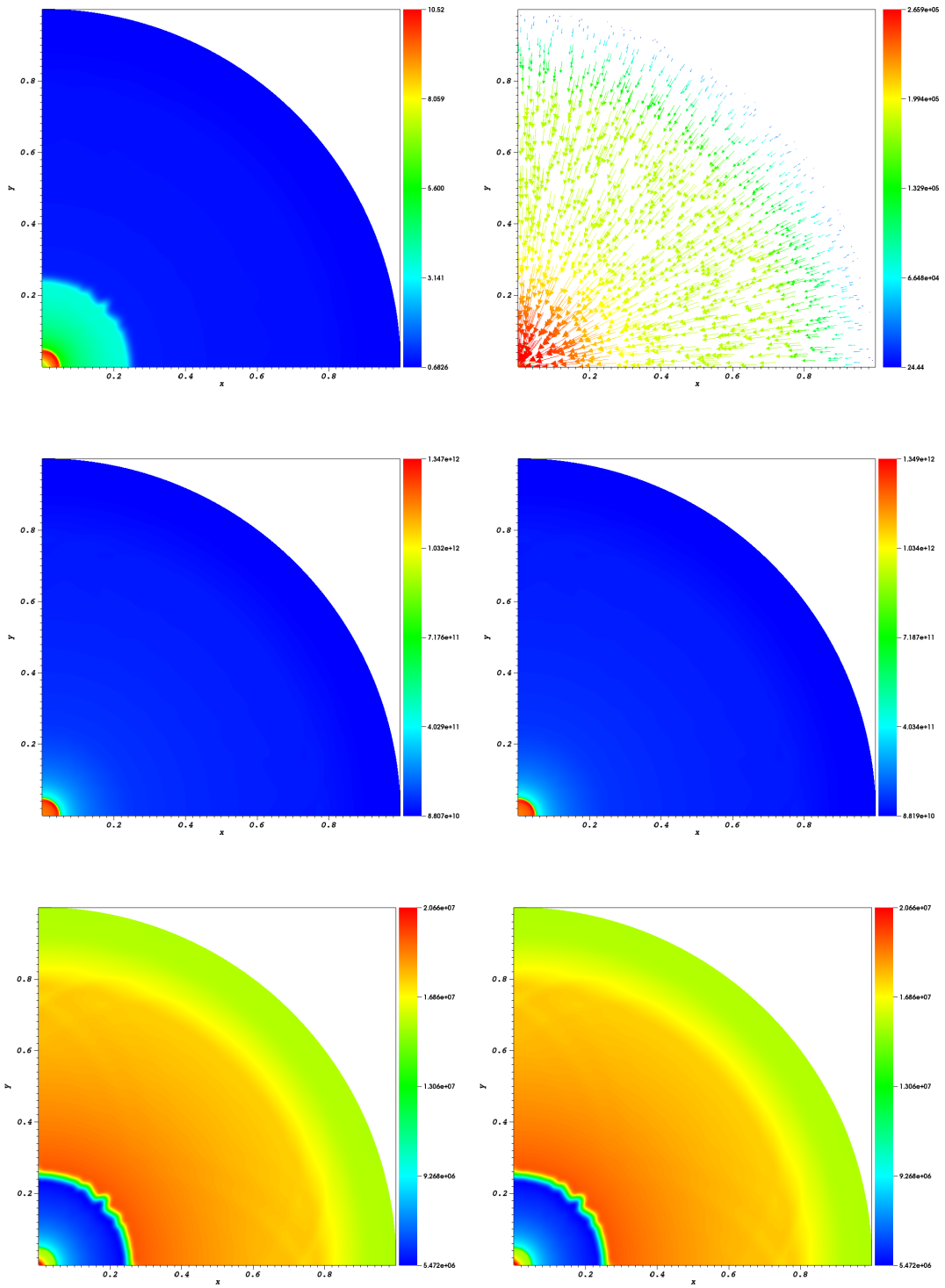

Figure 11: Implosion problem at $t_2 = 6.22 \times 10^{-7} s$. 2-D fields of Left-Top: Density, Right-Top: Velocity, Left-Center: Electronic pressure, Right-Center: Ionic pressure, Left-Bottom: Electronic temperature, Right-Bottom: Ionic temperature.

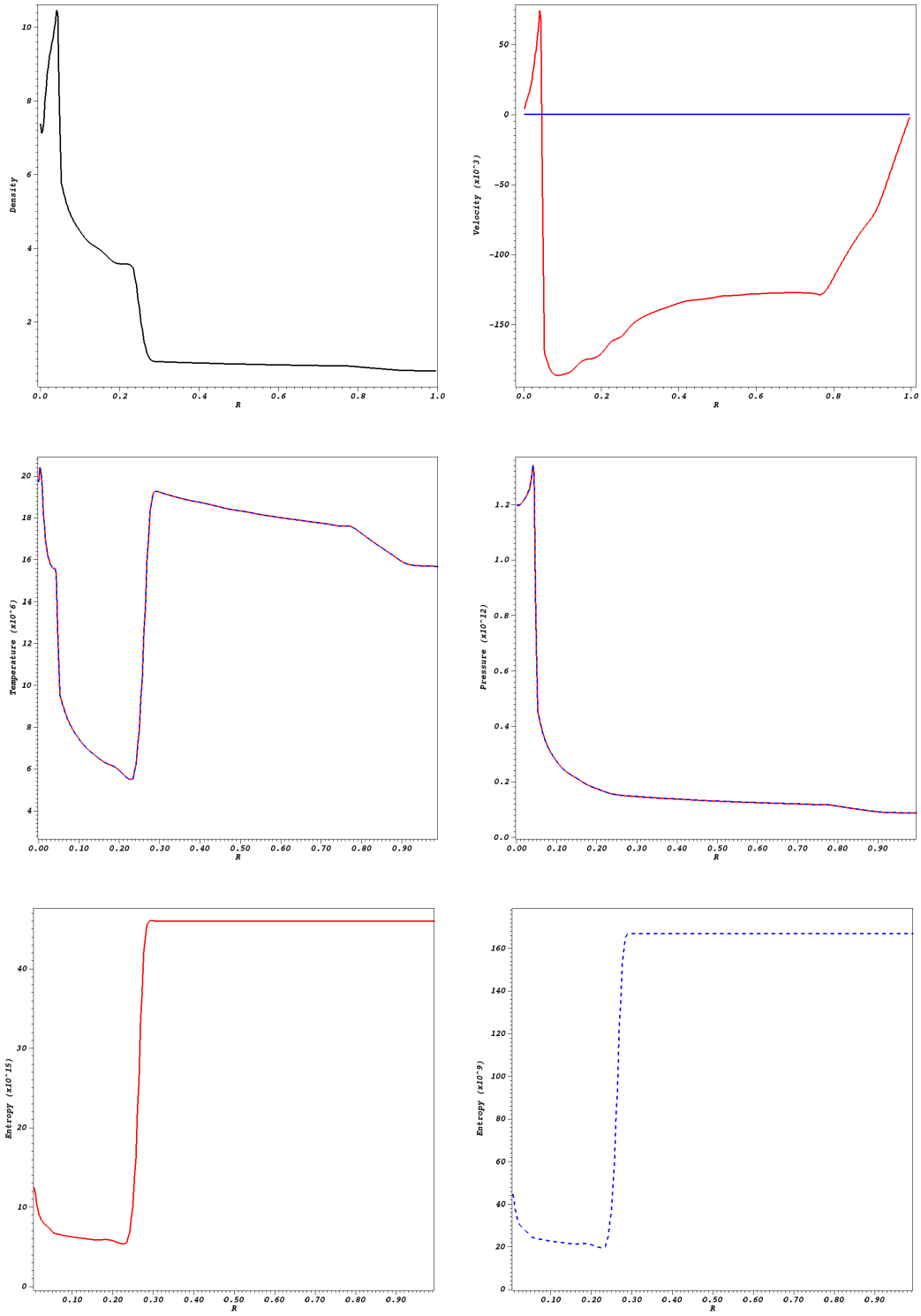

Figure 12: Implosion problem at $t_2 = 6.22 \times 10^{-7} s$. 1-D fields at $y = x$ of Left-Top: Density, Right-Top: Radial (red) and tangential (blue) velocities, Left-Center: Electronic (red) and ionic (blue) temperatures, Right-Center: Electronic (red) and ionic (blue) pressures, Left-Bottom: Electronic entropy, Right-Bottom: Ionic entropy.

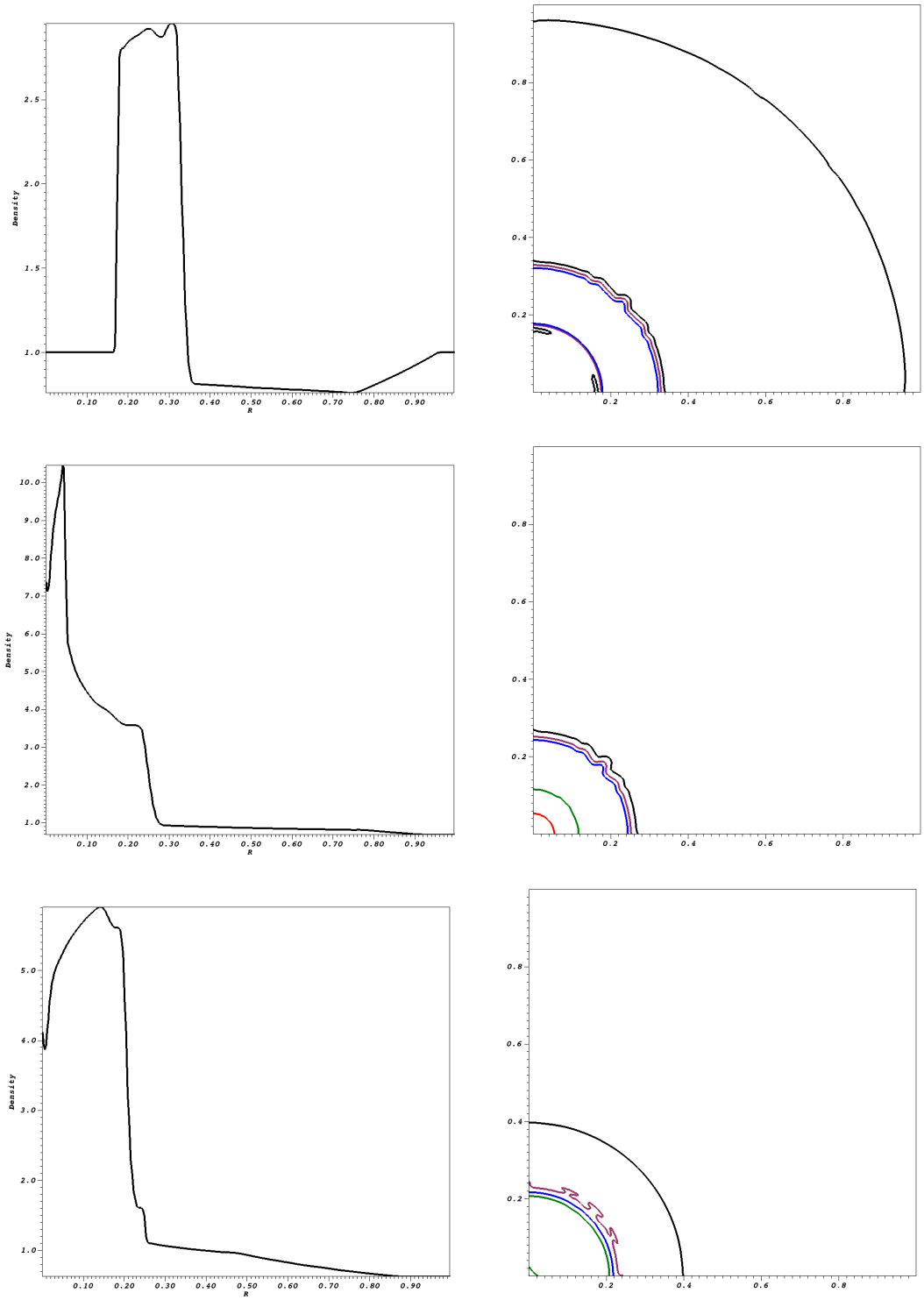

Figure 13: Implosion problem, Density, Left: 1-D fields at $y = x$, Right: 2-D isolines at $\rho = 1$ (black), $\rho = 1.585$ (violet), $\rho = 2.369$ (blue), $\rho = 4.259$ (green), and $\rho = 6.047$ (red). Top: $t_1 = 4.0901 \times 10^{-7} s$, Middle: $t_2 = 6.22 \times 10^{-7} s$, Bottom: $t_3 = 8.4973 \times 10^{-7} s$.

6.3 Sedov injection in 2-D Cartesian geometry

For this test case, a Sedov problem is considered in a uniform medium with cylindrical axisymmetry. It consists in the deposit of an intense energy spot in the center of the disc of the uniform medium. Here, we adapt this test from [34, 35] to the bi-temperature model with

$$\left\{ \begin{array}{lcl} T_e & = & 1.7406 \times 10^7 K, \\ T_i & = & 5.802 \times 10^6 K, \end{array} \right.$$

the injection temperature of the electrons and the ions. The temperatures of the rest of the domain are

$$T_e = T_i = 2.901 \times 10^4 K.$$

The rest of the data is given by

$$\left\{ \begin{array}{lcl} \rho & = & 1, \\ \mathbf{u} & = & 0. \end{array} \right.$$

In [34, 35], the domain is a quarter of disc of radius equal to 1. In this simulation, the computational domain is a complete disc of radius equal to 1 meshed with 8321 points with a mesh similar to the one of Figure 8. Such a mesh has the property that the points are almost aligned in the R-direction but avoid small cells at the center of the domain. Note also that in contrast with polar meshes, the origin is not a singular point and therefore, since the computation is done on the whole disc, there is no boundary conditions to enforce at the center of the disc which is an interior point. The injection of energy takes place in the cell containing the disc center. The final time of the computation is chosen in order to compare the results to the ones obtained in [34]. Figures 14 shows the computed results at $t = 9.7634 \times 10^{-6} s$ that consists of an expanding shock wave. Likewise the implosion problem, the initialization is 2-D in the Cartesian coordinates and the expected solution is 1-D in cylindrical coordinates. As shown in Figure 14, the numerical solution respects this property. This is what was expected from the previous test since the loss of the cylindrical symmetry of the computation was shown to occur on contact discontinuity but not on propagating shock waves. Figure 15 presents the results of the density and temperatures at three different times.

In Figure 15, at the final time, the maximum of density is about 1.2, whereas in [35] the density reaches a maximum around 3.5. It is shown in [22] that the exact density reaches a maximum of 6. This is due to the fact that the mesh used here is not fine enough.

At the initilization, the relaxation time to reach the temperature at the injection cell is $1.3 \times 10^{-9} s$ while at the end of the simulation it is $2.2 \times 10^{-9} s$. Therefore, the equilibrium is reached soon after the beginning of the simulation. Figure 15 gives a zoom near the origin of the 1-D profils of the two temperatures at two different times in the beginning of the simulation: The two temperatures attain rapidly a common value on the whole domain as the expanding shock propagates from the disc center.

This test has shown that the numerical method is able to compute a strong expanding shock wave on a 2D cartesian mesh with no loss of the 1-D cylindrical character of the solution.

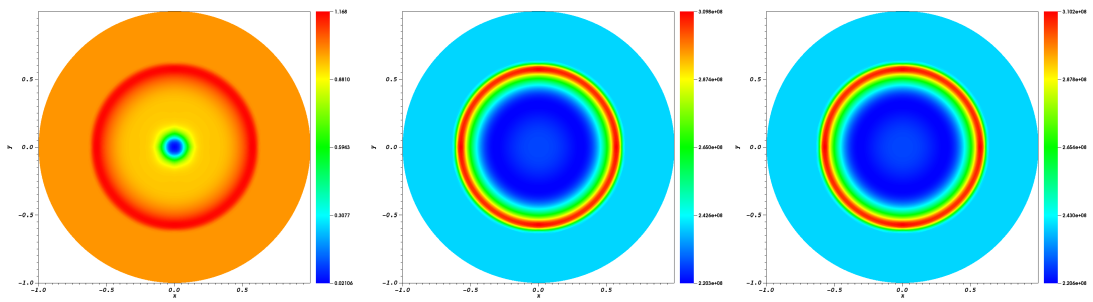

Figure 14: Sedov injection in 2-D Cartesian geometry at $t = 9.7634 \times 10^{-6}s$. Left: Density, Center: Electronic pressure, Right: Ionic pressure.

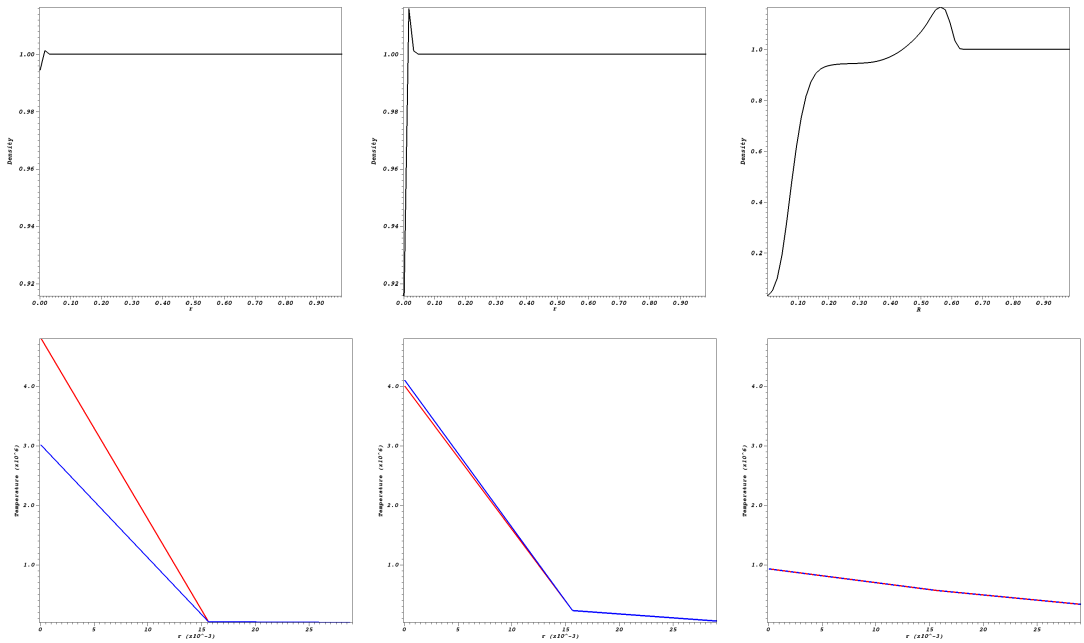

Figure 15: Sedov injection in 2-D Cartesian geometry. 1-D profils at Left: $t = 6.73 \times 10^{-10}s$, Middle: $t = 6.73 \times 10^{-9}s$, Right: $t = 9.7634 \times 10^{-6}s$, Top: Density. Bottom: Electronic (red) and Ionic (blue) temperatures.

6.4 Sedov injection in a poloidal plane of a torus with axisymmetry initialization

We are now interested in testing the 3D numerical method in cylindrical (R, Z, ϕ) geometry that we have presented in section 4.2. For this, we re-run the previous test where now the considered disc is contained in the poloidal plane of a torus. We assume that the major radius of the torus is 5 and consider two simulations. The first one is a 2D one where we assume that all derivatives in the ϕ-direction are zero and therefore we use only one poloidal plane to define the computational domain. The second simulation is a true 3D computation where 20 poloidal planes have been used to discretize the toroidal direction. In this case, the initial conditions are axisymmetric in the ϕ-direction, and do not depend on ϕ. Therefore, we expect the solution to be axisymmetric for all $t > 0$. The goal of this test is to check that the numerical method does not generate artificial toroidal velocities and does not destroy the axisymmetric character of the solution.

The results are presented at $t = 9.7634 \times 10^{-6} s$ in Figures 16.

With respect to the previous simulation, we observe that in a toroidal geometry, the solution is not anymore 1-D in a R, ϕ-coordinate system. Indeed, we can see that the wave is moving faster on the center of the torus side than on the exterior side. On the maximum value of the pressures and the density, we note small differences: the maximum density in the Cartesian case, respectively in the axisymmetric case, is 1.168, respectively 1.145. Then time when the ionic and electronic temperatures become equal is also slighly changed: it is now of $5.5 \times 10^{-8} s$ instead of $5 \times 10^{-8} s$ in the Cartesian case.

As shown in Figure 16, the 3-D results are extremely close to the 2-D ones. Indeed there is only a difference of 1×10^{-3} on the extrema of the density of each cases. Moreover, no toroidal velocities has been generated in the 3-D as shown in Figure 17 and the solution remains axisymmetric.

We find in the last three runs that our numerical method is able to handle both Cartesian and cylindrical geometries. Indeed, we obtain comparable solutions between the two 2-D runs and the difference observed in the cylindrical runs is due to force created in this geometry. Finally, the 3-D toroidal numerical method has also been validated in getting really close results to the 2-D axisymmetric run.

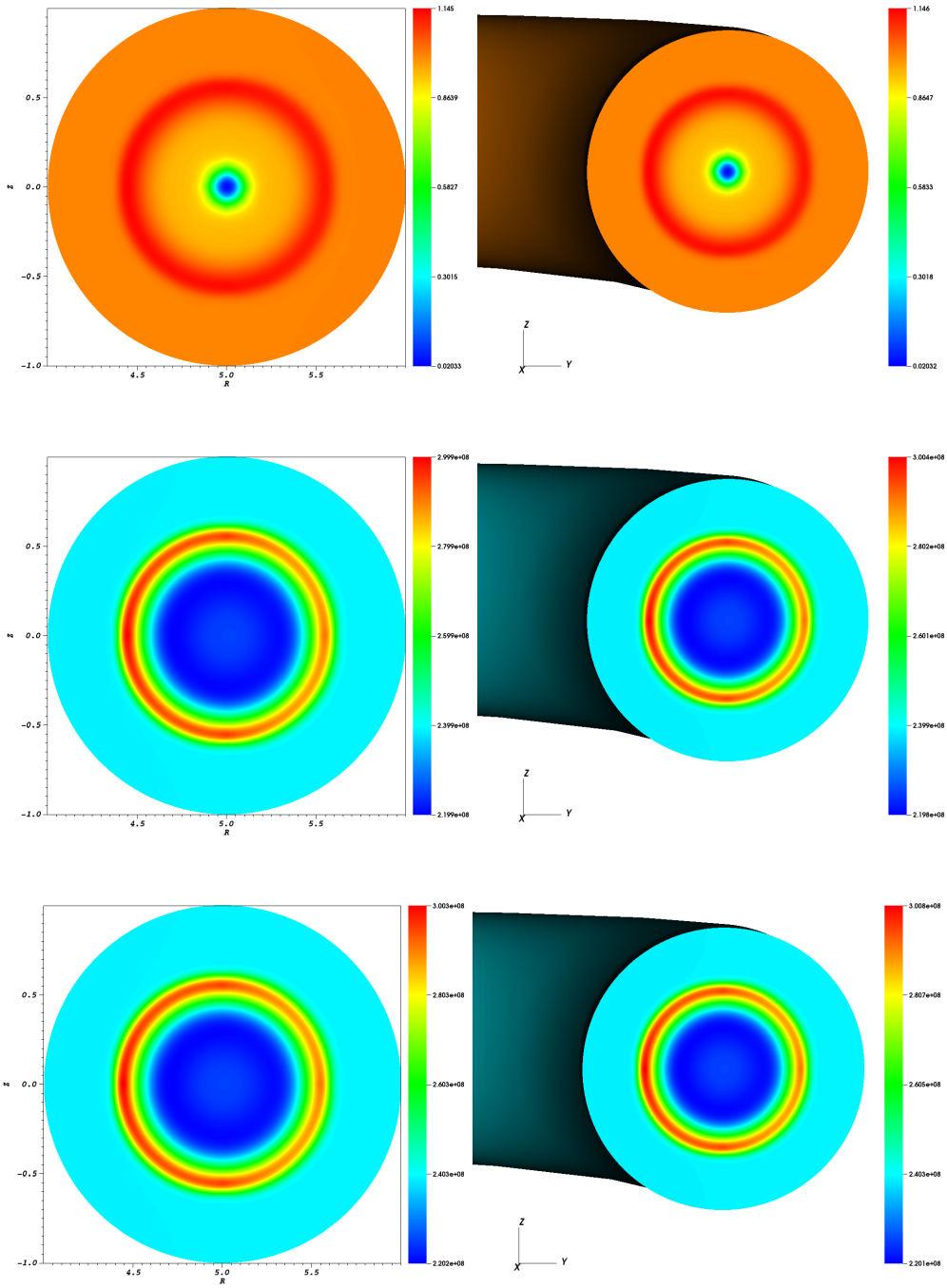

Figure 16: Sedov injection in axisymmetric toroidal geometry at $t = 9.7634 \times 10^{-6} s$. Comparison of the 2-D axisymmetric and 3D computations. Left: 2-D run, Right: 3-D run, Top: Density, Center: Electronic pressure, Bottom: Ionic pressure.

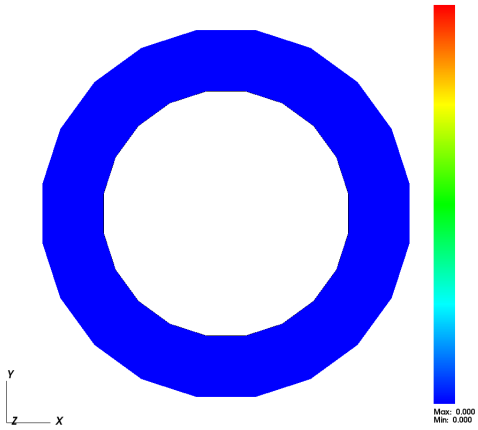

Figure 17: Sedov injection in 3-D toroidal geometry, toroidal velocity u_φ at $t = 9.7634 \times 10^{-6} s$ along $Z = 0$.

6.5 Triple point problem in a rectangular computational domain

The goal of this next experiment is to emphasize that in absence of temperature relaxation, the solution of the bi-temperature model is not identical to the solution of a single temperature model even if the electronic and ionic temperatures are initially equal.

Then, we consider a three state problem, inspired by the test case carried out in [22] and compare their results to the ones of the relaxation scheme. The electronic and ionic pressures are chosen to be equal and correspond to the same total pressure as the one fixed in [22]. The other difference between the two tests is that in our test, the adiabatic index γ is uniform and set equal to $5/3$.

The computational domain is the rectangle $[0,7]\times[-3,3]$ meshed with 70×60 points with symmetric elements around the x-axis. The domain is divided in three different sub-domains Ω_1, Ω_2, and Ω_3. The sub-domain Ω_1 is given by the rectangle $[1,7]\times[-1.5,1.5]$ and contains a high-density and low-pressure fluid. The sub-domain Ω_2 corresponds to the rectangle $[0,1]\times[-3,3]$ and is composed of a high-density and high-pressure fluid. Finally, the sub-domain Ω_3 is the rest of the domain and contains a low-density and low-pressure fluid. This description is summarized in Figure 18.

In [22], the evolution of this three-state problem is described: the intersections of the three sub-domains Ω_1, Ω_2, and Ω_3 are located at $(1,-1.5)^T$ and $(1,1.5)^T$, those two points are named triple points. Let us first consider a point located on the interface between Ω_2 and Ω_1 far from the triple points, the initial data generate three waves which are a contact discontinuity, a rightward shock, and a leftward rarefaction. This is also the case for a point on the interface between Ω_2 and Ω_3 far from the triple points. In the case of the interface between Ω_1 and Ω_3, it produces a contact discontinuity. Around the triple points, the situation is quite tricky. Since the different waves are interacting together it leads to a complex 2-D fluid flow. As it is pointed out in [22], the two rightward shock waves of Ω_1 and Ω_3 are not moving at the same sound speed due to their difference of density. Indeed we have $\rho_3 c_{s,3} < \rho_1 c_{s,1}$, then the rightward shock of Ω_3 is moving faster than the Ω_1 one. This creates a strong shear leading to a Kelvin-Helmholtz instability and to the formation of a vortex.

In our simulation, we set $\nu_{ei}=\nu_{ie}=0$ and leave the ionic and electronic temperature evolve independently. In Figure 19, we compare the results of the internal energy of the mixture given by

$$\varepsilon = \frac{1}{\gamma-1}\frac{p_e+p_i}{\rho},$$

at the time $3.5s$ and $5s$ with the results of [22]. We can see that at $t=3.5s$ the results obtained with the relaxation scheme for the bi-temperature Euler equations are quite different from the ones of [22] (note that in Figure 19 the results of [22] are obtained by two different numerical methods, this is why their results are not symmetric with respect to the $y=0$ axis.) Indeed, Figure 20 displays the ratio $\dfrac{T_i-T_e}{T_e}$ at two successive times which shows that the temperatures do not remain identical although $T_i=T_e$ at the initialization, and without the use of thermal exchange in the equations The same result can be inferred from Figure 21 that shows the density, the electronic temperature, and the ionic one at $t=3.5s$ and $t=5.0s$. This is due to the fact that in the transport step, the electronic entropy jump is assumed to be zero across a shock. Therefore the discontinuous solutions of the two-temperature model are not the same than the ones of the mono-fluid Euler equations and even if the initial temperatures are equal, in the presence of discontinuous solutions, the bi-temperature Euler model is not equivalent to the mono-fluid Euler model.

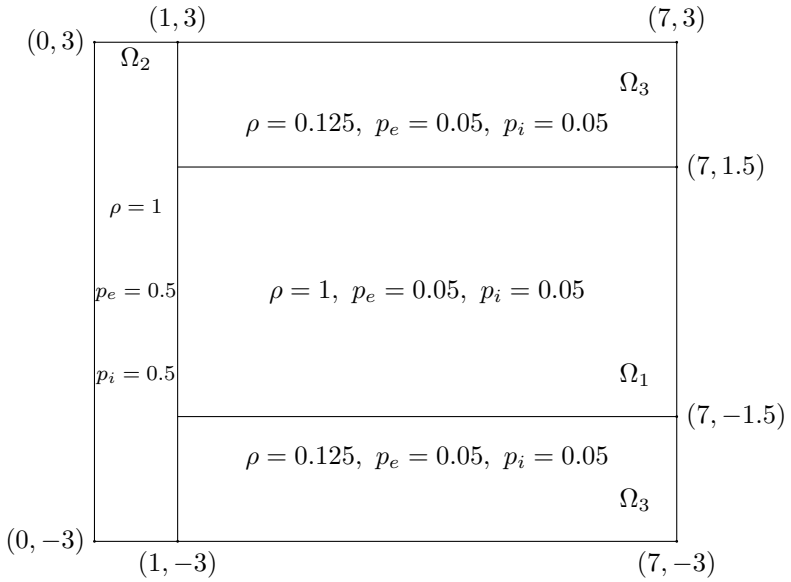

Figure 18: Initialization of the triple point problem in a rectangle.

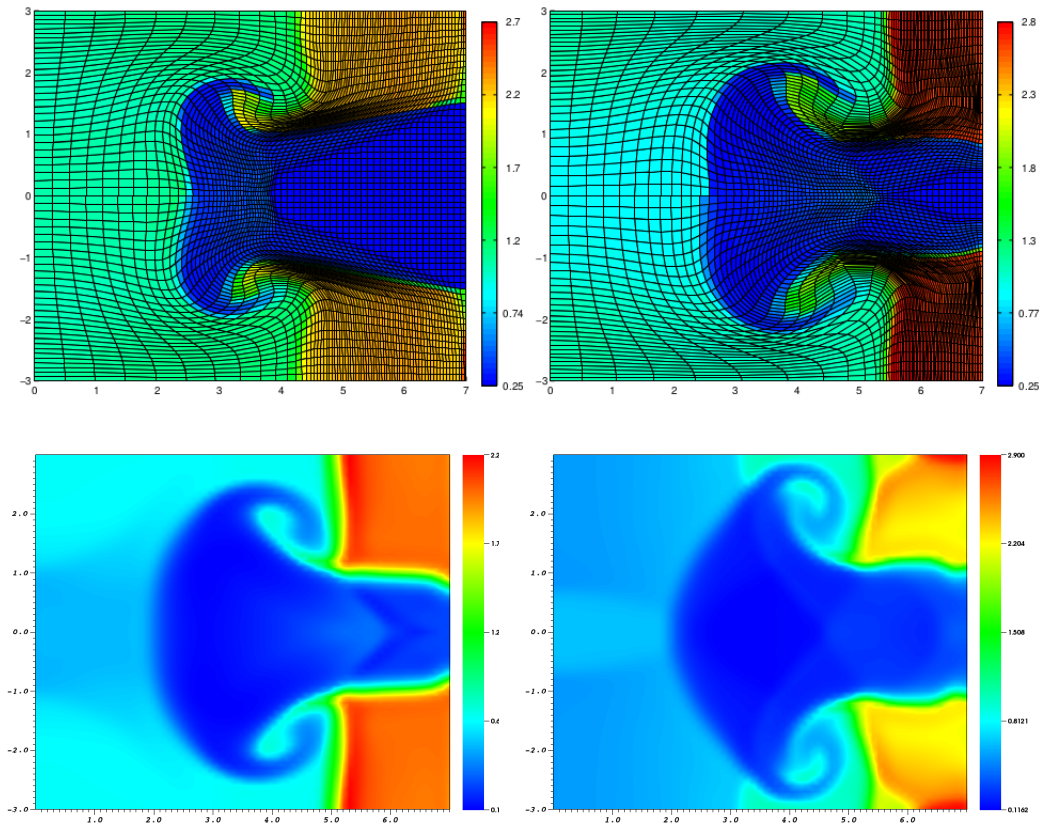

Figure 19: Triple point problem total internal energy at $t = 3.5s$ (left) and at $t = 5.0s$, Top: Results from [22] for mono-temperature Euler equations where the top of the domain is obtained with the Volume of Fluid method and the bottom of the domain with the concentration equations, Bottom: Relaxation scheme for bi-temperature Euler equations.

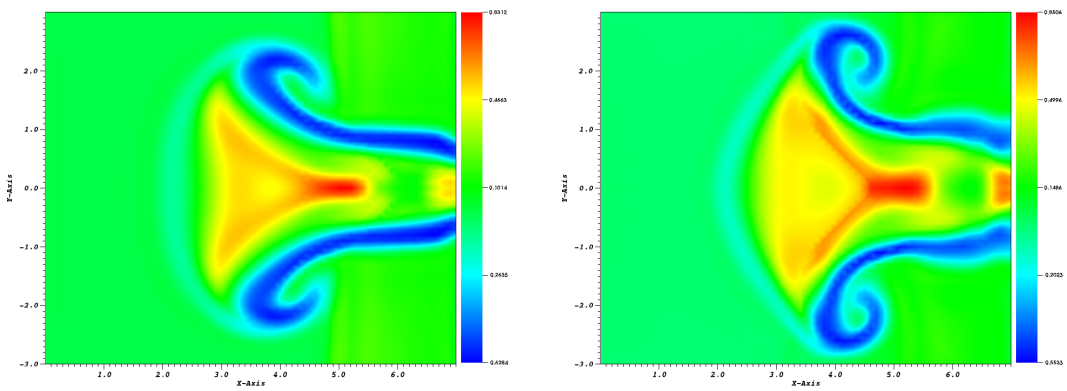

Figure 20: Triple point problem, $\dfrac{T_i - T_e}{T_e}$ 2-D field at $t = 3.5s$ (Left), and $t = 5.0s$ (Right).

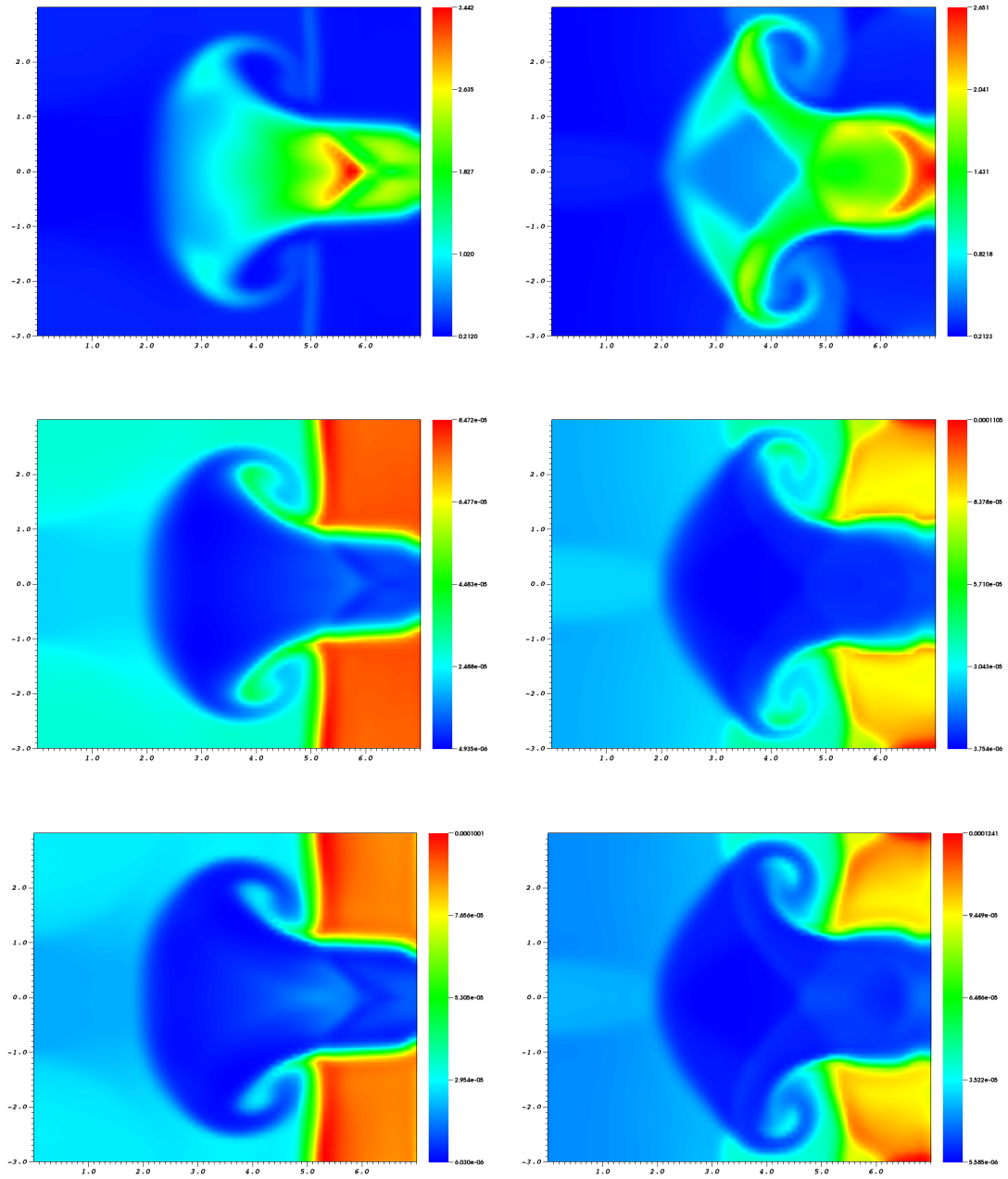

Figure 21: Triple point problem at $t = 3.5s$ (Left), and $t = 5s$ (Right). 2-D fields of Top: Density, Middle: Electronic temperature, Bottom: Ionic temperature.

6.6 Triple point problem in a disc in 2-D Cartesian geometry

Here we consider a triple point problem in a different geometry as a preliminary test for studying some problems of injection in tokamaks where very cold and dense cryogenic Deuterium/Tritium mixtures known as pellets are injected in a hot plasma. We first consider a problem in Cartesian geometry. The computational domain is now a disc of radius 1 meshed with 1435 cells. Figure 22 and Table 3 summarize the setting of the problem: the sub-domain Ω_1 is initially a domain of high density and low temperatures, it is given by the disc of radius 0.1414 of center point $(0.5, -0.5)$. The sub-domain Ω_3 is characterized by a low density and high temperatures and defined by the disc of center $(0, 0)$ and radius equal to 0.707 without the part Ω_1 of this disc. Finally, the sub-domain Ω_2 is the rest of the computational domain and its average density and temperatures are choosen to be between the density and temperaturues of the other two domains.

	ρ	$\mathbf{u}$	T_e(K)	T_i(K)	$p_e + p_i(Pa)$
Ω_1	3	0	3.4812×10^6	2.3208×10^6	1.4348×10^{11}
Ω_2	1	0	2.78496×10^7	1.85664×10^7	3.8262×10^{11}
Ω_3	0.5	0	3.4812×10^7	2.3208×10^7	2.3914×10^{11}

Table 3: Initial data of the three states of the triple points problem.

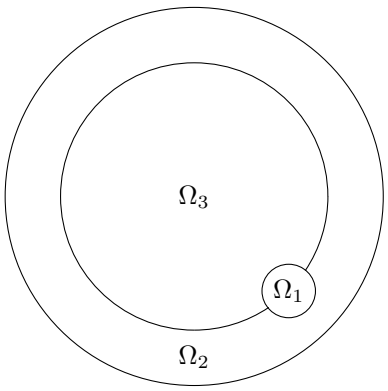

Figure 22: The three domain of the triple point problem in the (R, Z) plane.

We first comment on the differences in ionic and electronic temperatures for this test case. According to the formula (93) giving the temperature relaxation times, the equilibrium time varies as $T^{3/2}$. More precisely, at time $t = 0$, the temperature relaxation times in the three domains are

$$\left\{ \begin{array}{lcl} t_{\Omega_1} & = & 8.51 \times 10^{-11} s, \\ t_{\Omega_2} & = & 3.86 \times 10^{-9} s, \\ t_{\Omega_3} & = & 1.00 \times 10^{-8} s. \end{array} \right. \tag{96}$$

Hence we expect temperature equilibrium to be reached rapidly in domain Ω_1 while domain Ω_3 will be the last one where temperature equilibrium will occur.

Figure 23 displays the ratio $\dfrac{T_i - T_e}{T_e}$ at three different times.

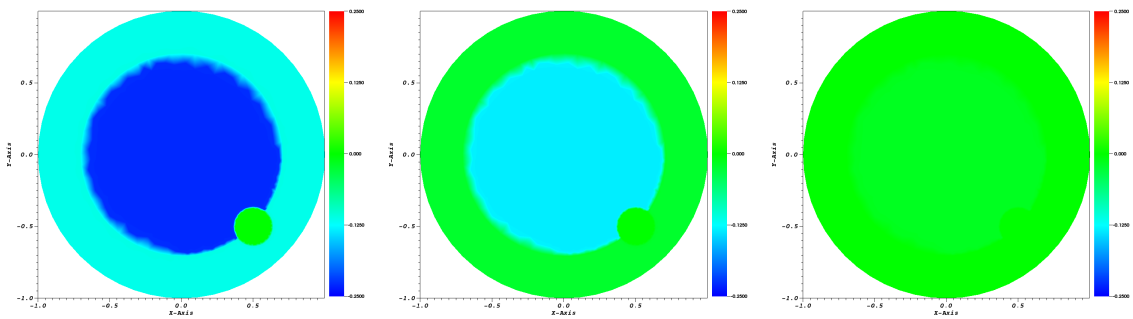

Figure 23: Triple point problem in Cartesian geometry. $\dfrac{T_i - T_e}{T_e}$ 2-D fields at $t = 2.1 \times 10^{-9} s$ (left), $t = 4.7 \times 10^{-9} s$ (middle), and $t = 1.35 \times 10^{-8} s$ (right).

At $t = 2.1 \times 10^{-9} s$, we can see that only the sub-domain Ω_1 gets equal temperatures. Then, at $t = 4.7 \times 10^{-9} s$, the cold and the intermediate sub-domains have reached the equilibrium. Finally, after $t = 1.35 \times 10^{-8} s$, the electronic and the ionic temperatures are equal in all the domain.

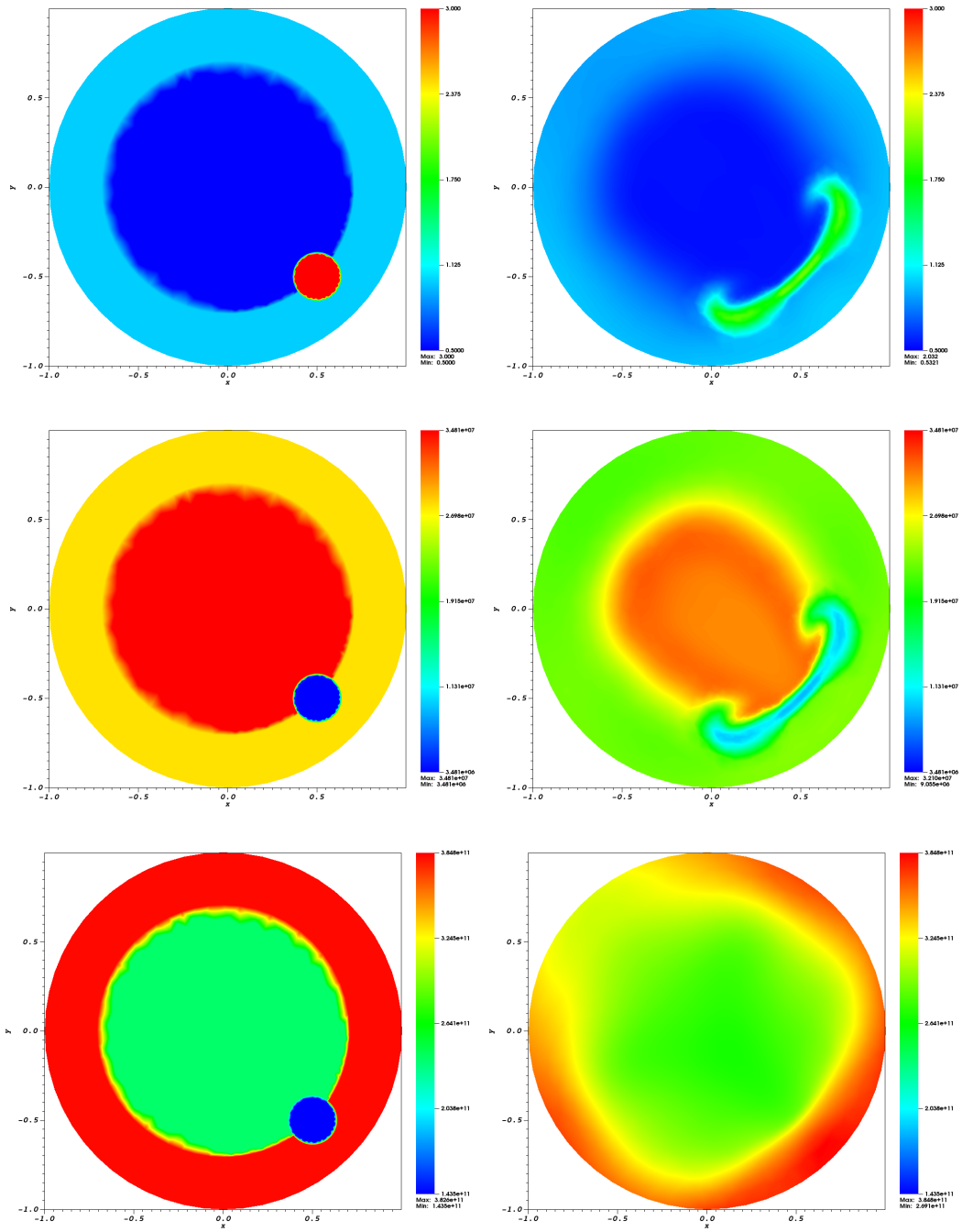

Figure 24: Triple point problem in Cartesian geometry. Initial data (Left) and solution at $t = 1.1574 \times 10^{-5} s$ (Right). Top: Density, Center: Electronic temperature, Bottom: Total pressure.

The results are at $t = 1.1574 \times 10^{-5}s$, and are given in Figure 24. The initial cold and dense domain Ω_1 corresponds to a zone of low pressure. Therefore it has been crushed by the high pressure neighbouring zones and has expanded mainly in the angular direction. Another noticeable result is that at this time, the density and temperatures have been smoothed out: while the initial density was in the interval $[0.5, 3]$, it is now between 0.5321 and 2.032 and the same smoothing effect can be noticed for the temperature. This effect is mainly due to pressure reflection on the boundary of the domain. Indeed, a rough estimate of the sound speed at time $t = 0$ ($c_s \approx 8.92816 \times 10^5 m.s^{-1}$) shows that at $t = 1.1574 \times 10^{-5}s$, pressure waves have crossed the domain around 5 times leading to a smoothing of the density and temperature fields.

6.7 Triple point problem in the plane of a torus with axisymmetry initialization

As in Section 6.4 we now reproduce the previous test case in the geometry of a torus. The aim of this test case is to see the influence of the geometry. We set the major radius of the torus at 3. As in Section 6.4, we have performed two simulations: the first one is a pure 2-D axisymmetric computation while the second is a true 3-D one where the toroidal direction has been discretized with 20 planes. As in Section 6.4 we have checked that the 3-D runs maintain the 2-D axisymmetric character of the solution and that no toroidal velocities have been created.

Since the results between the 3-D and the 2-D axisymmetric are extremly close, we present only the ones of the 2-D axisymmetric simulation.

The results are given in Figure 25. We see that the average domain Ω_2 expends more to the initial hot domain in the area closer to the center of the torus. This phenomenum can be due to centripetal or centrifugal forces. Moreover, the final temperatures are quite different of the 2-D Cartesian case. Indeed, for the cold domain, we obtain $8.738 \times 10^6 K$ for the electronic and ionic temperatures of the cold domain instead of $9.055 \times 10^6 K$. Then, we can suppose that the evolution is slower in the cylindrical case than in the Cartesian one. We also remark, that the final shape of the cold domain Ω_1 is not anymore symmetric and the temperature is hotter closer to torus center than to the exterior side. Likewise, the density is higher in the torus center zone than the exterior, and the final value of the domain Ω_1 is 2.092 instead of 2.032. In fact, the cold domain seems to move to the exterior of the torus. At the end of the simulation, as expected the electronic and ionic temperatures are balanced. In Figure 26, we compare the velocity in the polidal plane (R, Z) to the one of the Cartesian run. We can see that for the cylindrical geometry, the velocity is around twice the maximum of velocity of the Cartesian run. Indeed, around the border between the hot domain and the average domain closer to the center of the torus, the velocity of the axisymmetric run is about four times the one of the Cartesian geometry.

It follows from the above two last numerical tests that the geometry is an important input, since it largely modifies quantitatively and qualitatively the behaviour of the velocity field, and this the whole set of results.

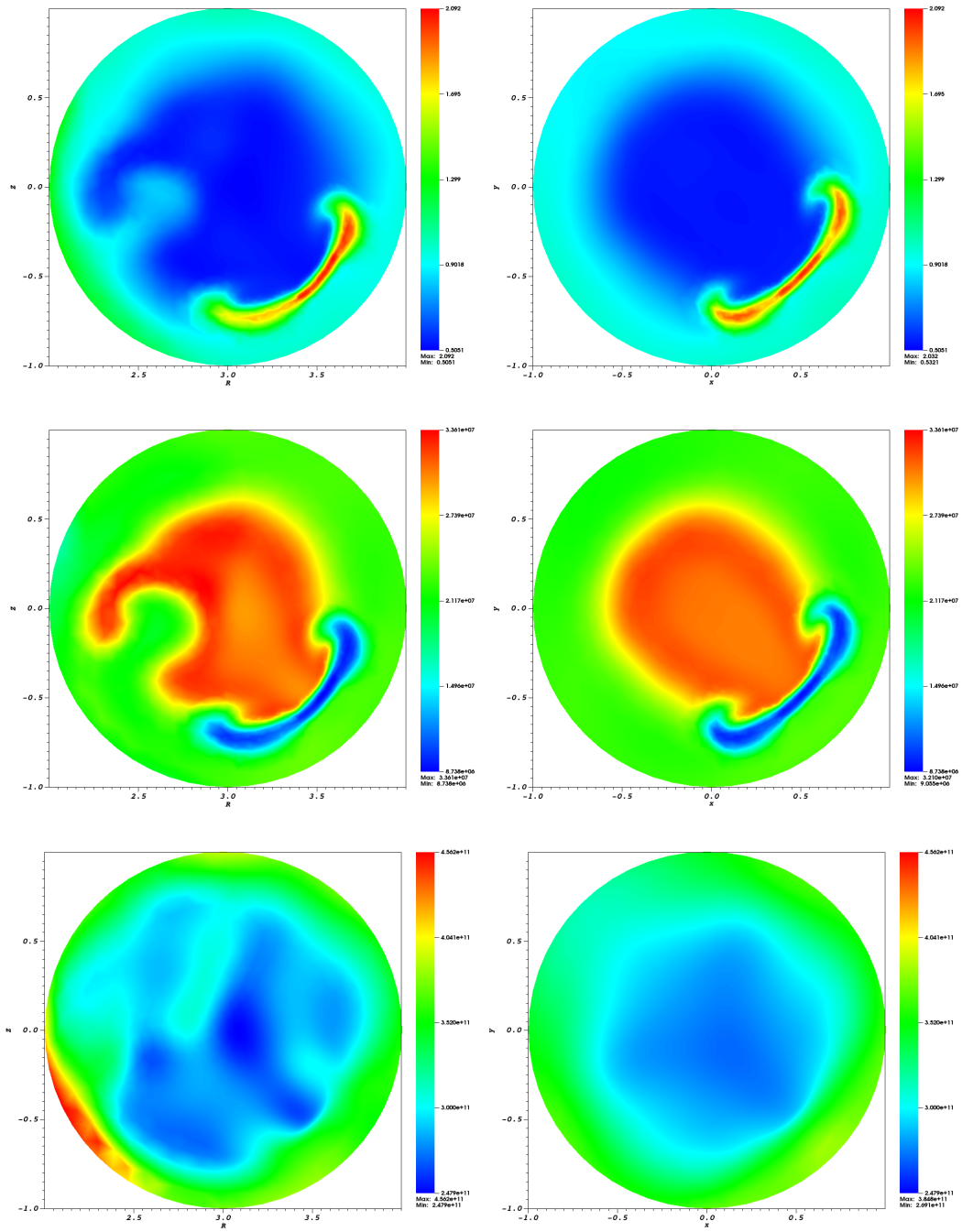

Figure 25: Triple point problem at $t = 1.1574 \times 10^{-5} s$. Comparison of the results obtained in Cartesian geometry and in a torus. Left: 2-D axisymmetric run, Right: 2-D Cartesian run. Top: Density, Center: Electronic temperature, Bottom: Total pressure.

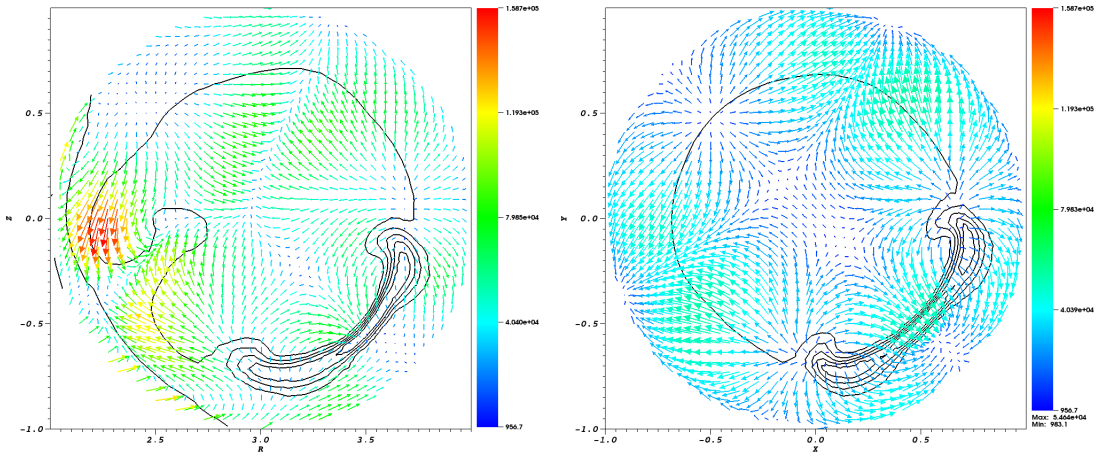

Figure 26: Triple point problem at $t = 1.1574 \times 10^{-5} s$. Comparison of the results obtained in Cartesian geometry and in a torus. Velocity vectors with density contours. Left: 2-D axisymmetric run, Right: 2-D Cartesian run.

6.8 Triple point problem in 3-D toroidal geometry

Here, we propose a fully 3-D numerical test in toroidal geometry. This test is based on the two previous cases, but instead of having an axisymmetric initialization, we consider that the initial cold and dense zone is a small cylinder. The periodic toroidal direction is meshed in a regular manner with 20 points and we assume that the zone where the cylinder is localized corresponds to the angular domain $[0, 3 \times 2\pi/20]$. In the domain where the cylinder is localized, a three state initialization is used while in the rest of the domain the fields are described by two different states. The different domains of the poloidal plans are described in Figure 27, and the initialization used for the domain Ω_1, Ω_2, and Ω_3 is given in Table 3. The three poloidal planes that intersect the cylinder as numbered as the poloidal planes 1, 2, and 3. Then, the two neighbouring planes are numbered the planes 4 and 20.

Figures 29, 30 and 31 display the results in the planes 1 to 3, 4, 20 and 10. They show that the extrema are reduced with respect to the 2D case. For instance, in the 3D case, the extrema are 0.46 and 1.867 instead of 0.5051 and 2.092 in the 2D asisymmetric case. But, globally, the evolution of the solution is similar to the one described for an axisymmetric intial state except for the total pressure. We can however note that we have a 3 dimensional effect in the toroidal direction leading to a increased smoothing of the extrema in the 3D case although this effect seems to be weak, up to this time. Such a computation would require a much denser mesh in the toroidal direction to give meaningful results.

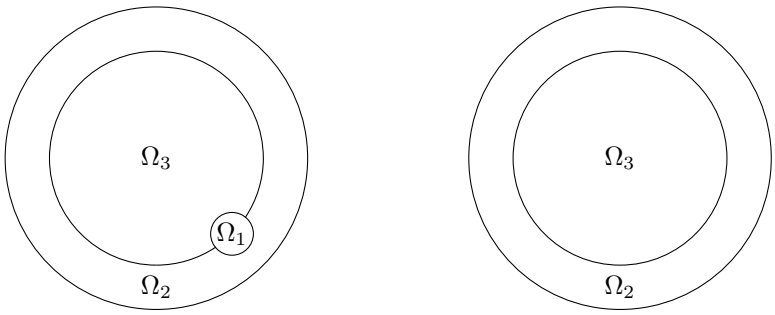

Figure 27: Triple point problem initial domain in 3-D toroidal geometry. Left: for the poloidal planes 1 to 3. Right: for the rest of the poloidal planes (4 to 20).

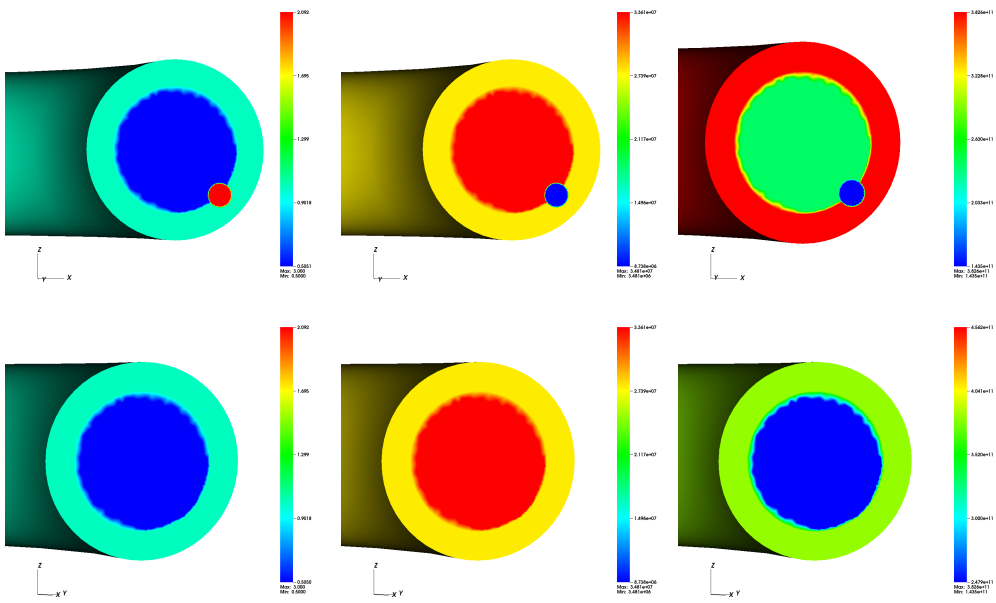

Figure 28: Triple point problem initialization. Top: Poloidal planes 1 to 3, Bottom: Poloidal planes 4 to 20. Left: Density, Center: Electronic temperature, Right: Total pressure.

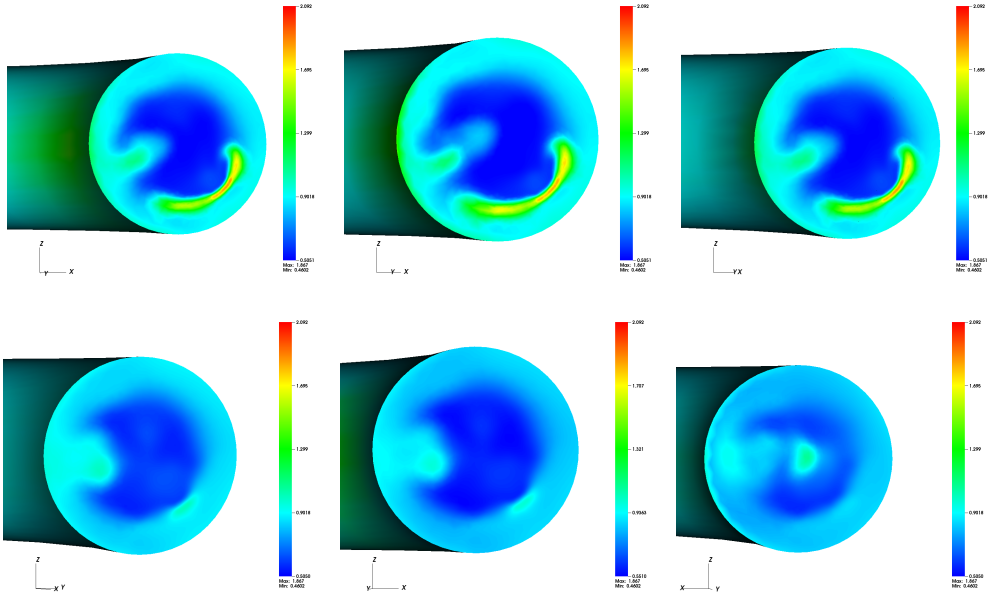

Figure 29: Triple point problem in 3-D toroidal geometry. Density at $t = 1.1574 \times 10^{-5}s$. Top-Left: Plane 1, Top-Center: Plane 2, Top-Right: Plane 3, Bottom-Left: Plane 4, Bottom-Center: Plane 20, Bottom-Right: Plane 10.

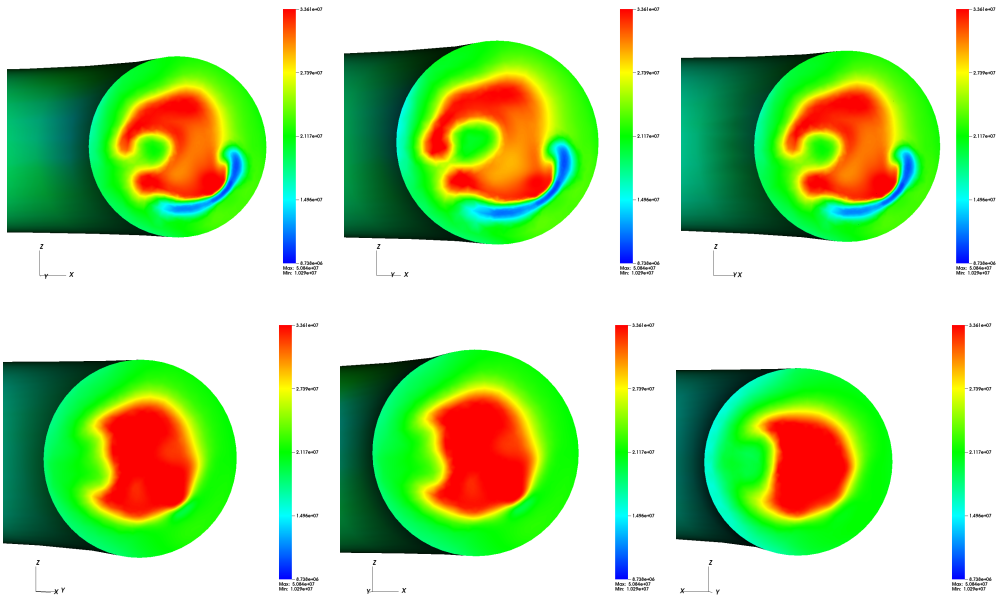

Figure 30: Triple point problem in 3-D toroidal geometry. Electronic temperature at $t = 1.1574 \times 10^{-5}s$. Top-Left: Plane 1, Top-Center: Plane 2, Top-Right: Plane 3, Bottom-Left: Plane 4, Bottom-Center: Plane 20, Bottom-Right: Plane 10.

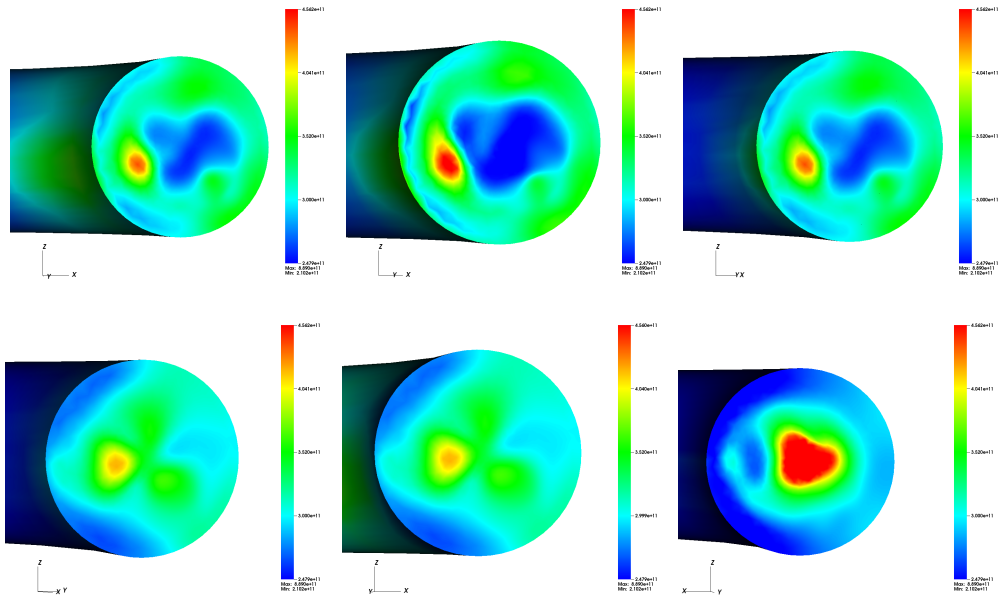

Figure 31: Triple point problem in 3-D toroidal geometry. Total pressure at $t = 1.1574 \times 10^{-5} s$. Top-Left: Plane 1, Top-Center: Plane 2, Top-Right: Plane 3, Bottom-Left: Plane 4, Bottom-Center: Plane 20, Bottom-Right: Plane 10.

7 Conclusions

In the present work, we have studied a numerical scheme for the approximation of the T_i–T_e model. This model considers the ion-electron mixture as a single fluid but retains two temperature or energy equations to describe the thermodynamics of the mixture. A derivation of this model that relies only on the assumption of a large plasma β parameter together with the standard assumption of quasi-neutrality has been presented. This derivation is more general than the ones in [16, 20, 24, 30, 1] and shows that similar models can be built without the massless electrons assumption. For smooth solutions, this model can be written under several different forms. Here, we have used a conservative form of the equations where instead of the two non-conservative temperature equations, we used the conservative total energy equation complemented by a conservative equation for the electronic entropy. While the preservation of the total energy equation must be respected by any model, other choices than the conservative form for the electronic entropy can be used and our choice is only motivated by the fact that due to the light mass of the electrons, the variations of electronic entropies can be large without affecting too much the total internal energy. With this choice, a relaxation scheme is proposed to solve the T_i–T_e model in Cartesian as well that in cylindrical coordinates by a finite volume method. The interest for cylindrical coordinate system is motivated by possible future applications to MCF and tokamaks.

Finally, we have presented several different numerical tests using the two coordinate systems and different geometries. The results have shown that the numerical scheme is able to simulate problems with large densities and pressure differences as well as fast phenomena. In the geometry of a torus, the proposed finite volume method has been tested on 3D test cases and has demonstrated its capability to respect the axisymmetric character of the solutions which is an important point for MCF applications. Future work on this topic will involve its extension to bounded plasma β parameter and the introduction of magnetic field and dissipative terms.

References

[1] Aregba-Driolet, D., Breil, J., Brull, S., Dubroca, B., and Estibals, E. Modelling and numerical approximation for the nonconservative bitemperature Euler model. *Submitted* (2016).

[2] Atzeni, S., and Meyer-Ter-Vehn, J. *The Physics of Intertial Fusion.* Oxford University Press, 2004.

[3] Aymar, R., Barabaschi, P., and Shimomura, Y. The ITER design. *Plasma Physics and Controlled Fusion 44*, 5 (2002), 519–565.

[4] Balescu, R. *Classical Transport*, vol. 1 of *Transport Processes in Plasmas.* North-Holland, Amsterdam, 1988.

[5] Balescu, R. *Classical Transport*, vol. 2 of *Transport Processes in Plasmas.* North-Holland, Amsterdam, 1988.

[6] Batten, P., Clarke, N., Lambert, C., and Causson, D. On the Choice of Wavespeeds for the HLLC Riemann Solver. *SIAM Journal of Scientific Computing 18* (1997), 1553–1570.

[7] Berthon, C., Coquel, F., and LeFloch, P. Why many theories of shock waves are necessary: kinetic relations for non-conservative systems. *Proceedings of the Royal Society of Edinburgh: Section A Mathematics 142*, 1 (2012), 1–37.

[8] Berthon, C., Dubroca, B., and Sangam, A. A Local Entropy Minimum Principle for Deriving Entropy Preserving Schemes. *SIAM Journal on Numerical Analysis 50*, 2 (2012), 468–491.

[9] Berthon, C., Dubroca, B., and Sangam, A. An Entropy Preserving Relaxation Scheme For Ten-Moments Equations with Source Terms. *Communications in Mathematical sciences 13*, 8 (2015), 2119–2154.

[10] Bettinger, A., and Decroisette, M. Laser megajoule project and impact on the inertial fusion program. *Fusion Engineering and Design 46* (1999), 457–460.

[11] Bhatnagar, P. L., Gross, E. P., and Krook, K. A model for collision processes in gases. *Physical Review 94* (1954), 511–524.

[12] Bilanceri, M., Combe, L., Guillard, H., and Sangam, A. A 3D finite volume scheme for the simulation of edge plasma in tokamaks. *ESAIM: Proceedings 43* (2013), 164–179.

[13] Bonnement, A., Fajraoui, T., Guillard, H., Martin, M., Nkonga, B., and Sangam, A. Finite volume method in curvilinear coordinates for hyperbolic conservation laws. *ESAIM: Proceedings 32* (2011), 163–176.

[14] Bouchut, F. *Nonlinear Stability of Finite Volume Methods for hyperbolic Conservation Laws and Well-Balanced Schemes for Sources.* Birkhäuser, 2004.

[15] Braginskii, S. I. Transport processes in a plasma. *Reviews of Plasma Physics 1* (1965), 205–311. Translated from the Russian.

[16] Coquel, F., and Marmignon, C. Numerical methods for weakly ionized gas. *Astrophysics and Space Science 260*, 1-2 (1998), 15–27.

[17] De Santis, D., Geraci, G., and Guardone, A. Finite Volume and Finite Element Schemes for the Euler Equation in Cylindrical and Spherical Coordinates. *Journal of Computational and Applied Mathematics 236* (2012), 4827–4839.

[18] Einfeldt, B., Munz, C., Roe, P., and Sjögreen, B. On Godunov-type methods near low densities. *Journal of Computational Physics 92*, 2 (1991), 273–295.

[19] Fitzpatrick, R. *Plasma physics: an introduction.* CRC Press, 2014.

[20] Freidberg, J. *Plasma Physics and Fusion.* Cambridge University Press, 2007.

[21] Furfaro, D., and Saurel, R. A simple HLLC-type Riemann solver for compressible non-equilibrium two-phase flows. *Computers & Fluids 111* (2015), 159–178.

[22] Galera, S., Maire, P.-H., and Breil, J. A two-dimensional unstructured cell-centered multi-material ALE scheme using VOF interface reconstruction. *Journal of Computational Physics 229* (2010), 5755–5787.

[23] Godlewski, E., and Raviart, P. A. *Numerical Approximation of Hyperbolic System of Conservation Laws.* Springer New York, 1996.

[24] Goedbloed, J. P., and Poedt, S. *Principles of Magnetohydrodynamics: With Applications to Laboratory and Astrophysical Plasmas.* Cambridge University Press, 2004.

[25] Guillard, H., and Abgrall, R. *Modélisation Numérique des Fluides Compressibles.* Series in Applied Mathematics. North-Holland, 2001.

[26] Hazeltine, R. D., and Meiss, J. D. *Plasma Confinement.* Dover publications, 2003.

[27] Hogan, W., Mosses, E., Warner, B., Soren, M., and Soures, J. The National Ignition Facility. *Nuclear Fusion 41*, 5 (2001), 565–573.

[28] Huba, J. *NRL plasma formulary.* Naval Research Laboratory, 2013.

[29] Kadomtsev, B. B. *Tokamak plasma, a complex physical system.* Institute of Physics Publishing, Bristol, 1993.

[30] Kulikovskii, A. G., Pogorelov, N. V., and Semenov, A. Y. *Mathematical Aspects of Numerical Solution of Hyperbolic Systems.* Chapmann and Hall/CRC, 2001.

[31] Leveque, R. *Finite-Volume Methods for Hyperbolic Problems.* Cambridge, 2004.

[32] Levermore, C. D. Moment Closure Hierarchies for Kinetic Theories. *Journal of Statistical Physics 83* (1996), 1021–1065.

[33] Levermore, C. D., and Morokoff, W. J. The Gaussian Moment Closure for Gas Dynamics. *SIAM Journal of Applied Mathematics 59* (1996), 72–96.

[34] Maire, P.-H. A high-order cell-centered Lagrangian scheme for compressible fluid flows in two-dimensional cylindrical coordinates. *Journal of Computational Physics 228* (2009), 6882–6915.

[35] Maire, P.-H., Abgrall, R., Breil, J., and Ovadia, J. A cell-centered Lagrangian scheme for two dimensional compressible frlow problems. *SIAM Journal on Scientific Computing 29* (2007), 1781–1824.

[36] Sentis, R. *Mathematical Models and Methods for Plasma Physics, Volume 1.* Birkhäuser, 2014.

[37] Shumlak, U., and Loverich, J. Approximate Riemann solver for the two-fluid plasma model. *Journal of Computational Physics 187*, 2 (2003), 620–638.

[38] Sod, G. A. A Survey of Several Finite Difference Methods for Systems of Nonlinear Hyperbolic Conservation Laws. *Journal of Computational Physics 27* (1978), 1–31.

[39] Toro, E. *Riemann Solvers and Numerical Methods for Fluids Dynamics, A Practical Introduction.* Springer, 1999.

[40] Toro, E., Spruce, M., and Speares, W. Restoration of the contact surface in HLL-Riemann Solver. *Shock waves 4* (1994), 25–34.

[41] Viozat, C., Held, C., Mer, K., and Dervieux, A. On vertex-centered unstructured finite volume methods for stretched anisotropic triangulations. *Computer Methods in Applied Mechanics and Engineering 190* (2001), 4733–4766.

[42] Wesson, J. *Tokamaks*, 3rd ed. International Series of Monographs on Physics. Oxford Sciences Publications, 2004.

[43] Xanthopoulos, P., Merz, F., Grörler, T., and Jenko, F. Nonlinear Gyrokinetic Simulations of Ion-Temperature-Gradient Turbulence for the Optimized Wendelstein 7-X Stellarator. *Physical Review Letters 99* (1999), 035002.

[44] Zohm, H., Angioni, C., Fable, E., Federici, G., Gantenbein, G., Hartmann, T., Lackner, K., Poli, E., Prote, L., and Sauter, O. On the physics guidelines for a tokamak DEMO. *Nuclear Fusion 53*, 7 (2013), 073019.

Contents

1 Introduction **3**

2 Plasma modeling **5**
2.1 Kinetic model 5
2.2 Macroscopic quantities 5
2.3 Collision operators 6
2.4 Moment equations 8
2.4.1 Mass conservation equation 8
2.4.2 Momentum equation 8
2.4.3 Energy equation 9
2.5 Maxwell equations 10
2.6 Bi-fluid MHD equations 11

3 Bi-temperature Euler model **14**
3.1 Quasi-neutral regime 14
3.2 Derivation of the bi-temperature model 17
3.3 The final bi-temperature model for large β parameter 21
3.4 Properties of the bi-temperature Euler model 22

4 Finite volume method **25**
4.1 Generalities on finite volume method 25
4.1.1 2-D cell-centered finite volume on rectangular mesh 26
4.1.2 2-D vertex-centered finite volume on a triangular mesh 28
4.2 Toroidal geometry 29
4.2.1 Cylindrical coordinates for toroidal problem and divergence form 30
4.2.2 Mesh design and adaptation to the finite volume method 31

5 Relaxation scheme for the bi-temperature Euler model **35**
5.1 Presentation of the scheme 35
5.2 Transport step 37
5.2.1 Properties of the relaxed system 37
5.2.2 Relaxation flux 39
5.3 Projection step 41

6 Numerical tests **42**
6.1 Shock tube 42
6.2 Implosion 46
6.3 Sedov injection in 2-D Cartesian geometry 53
6.4 Sedov injection in a poloidal plane of a torus with axisymmetry initialization . . 55
6.5 Triple point problem in a rectangular computational domain 58
6.6 Triple point problem in a disc in 2-D Cartesian geometry 62
6.7 Triple point problem in the plane of a torus with axisymmetry initialization . . . 65
6.8 Triple point problem in 3-D toroidal geometry 67

7 Conclusions **70**

RESEARCH CENTRE
SOPHIA ANTIPOLIS – MÉDITERRANÉE

2004 route des Lucioles - BP 93
06902 Sophia Antipolis Cedex

Publisher
Inria
Domaine de Voluceau - Rocquencourt
BP 105 - 78153 Le Chesnay Cedex
inria.fr

ISSN 0249-6399